Improved Ride Comfort through High-Bandwidth Seat Control Coupled with Passenger Biomechanics Analysis

By

ALI AKBARI
DISSERTATION

Submitted in partial satisfaction of the requirements for the degree of

DOCTOR OF PHILOSOPHY

in

Mechanical and Aerospace Engineering

in the

OFFICE OF GRADUATE STUDIES

of the

UNIVERSITY OF CALIFORNIA

DAVIS

Approved:

Donald Margolis, Chair

Dean Karnopp

Bahram Ravani

Committee in Charge

2023

ACKNOWLEDGEMENT

First and foremost, I would like to earnestly thank my beloved mentor and PhD advisor, Professor Donald L. Margolis. Professor Margolis has been much more than just a doctoral advisor to me. His continuous, compassionate, and generous offering of counsel, support, and wisdom has helped me to overcome many challenges that I came across during the last 5 years in my pursuit of higher education. Whether it was in addressing a problem I was facing in research, or just entertaining our mutual curiosities in physics and discussing the order in the cosmos, or even telling stories about past experiences, our conversations have always been quite rewarding. Frankly, with all the challenges that an immigrant student faces in life, Professor Margolis has been more of a father figure to me than simply an advisor who would offer strictly professional guidance. He always made a remark that I would be his last doctoral student, and while I might yet be just a finishing note on what is a glorious and formidable academic career, he would remain the most singularly influential character I have ever met for decades to come.

Secondly, I should like to thank my parents. I would like them to know how sincerely I appreciate their altruistic support and care all these years. They are honest, kind, and erudite people that I am forever grateful to for teaching me the value of said three characteristics.

Thirdly, I would like to thank Hyundai Motor Company for funding our research center throughout my years as a PhD student and I hope that our findings have been worth their investment.

And last but not least, I would like to thank and honor Sir Isaac Newton who made this all possible through pure genius. He said, “If I have seen further than others it is by standing on the shoulders of giants”. He has been forever my inspiration and academia was the giant upon whose shoulders I wished to climb, to perhaps see a bit further.

ABSTRACT

With the rise of autonomous vehicles, ride comfort is becoming ever more important for vehicle manufacturers as a design criterion. Studies on the currently established metrics for ride comfort indicate that they are often discrepant, and their predicted zones of comfort do not overlap. It is hypothesized that the perception of ride comfort for a vehicle passenger is correlated with their body's internal dynamic response to the disturbance vibrations coming in from the vehicle. To test this hypothesis, it is essential to develop a biomechanical model of a vehicle passenger.

The passenger body's internal mechanical structure is primarily the human spine which has an inherent geometric curvature. Therefore, in order to adequately predict the propagation of disturbance vibration into the passenger body, the biomechanical model should account for curved motion. A 25-DOF, lumped parameter, nonlinear biomechanical model of the upper body is proposed and validated against experimental literature. The model tracks curved trajectories and enables smooth posture prediction.

A full car model is developed, and its seat track velocities become input to the passenger model.

A non-dimensional, novel ride comfort cost function is devised according to the energy associated with the important internal displacements of the body.

The nonlinear model is linearized around its equilibrium position and a linear, observer-based, state-variable feedback control strategy is proposed. In normal ride conditions, the controller reduces the cost function by more than 50% without excessive consumption of power. Actuation takes place through the seats and is therefore cost effective as compared to manipulation of the entire suspension system.

1. Introduction

The concept of ride comfort in ground vehicles comfort is a major component in the development of vehicle dynamics. After all, for passenger vehicles, aside from the main purpose of transportation, it is also important that the passenger should remain comfortable during their ride, as well as getting to their destination in one piece. However, passenger comfort is conceptually a quality which cannot be directly measured. With the rise of autonomous vehicles and the competition for the market in the vehicle industry, passenger comfort is a vital concern for automotive manufacturers[1]. If we are to improve passenger comfort, first we must have a quantitative notion of the concept. Therefore, passenger comfort must somehow be quantified such that it could be integrated into a vehicle design. But how is this achieved?

First we must notice that there are many qualitative factors that impact the perception of ride comfort, such as temperature, air quality, visual and auditory ques, and vibration[2]. Since this research is studying ride comfort from a mechanical engineering perspective, vibration is considered to be the sole agent responsible for ride comfort.

To quantify ride comfort, one straight-forward way is to perform tests on human subjects. In such tests, a diverse group of volunteers, which would include differences in age, sex, genetics, body posture, etc.; is put through a series of standard ride tests. It is obvious that during such tests other non-subjective variables such as the test road, test vehicle, test driver, and the subjects' sitting position must be kept the same. After the test is conducted, each subject would receive a questionnaire in which they would assess their ride comfort with a qualitative index ranging from completely comfortable to completely uncomfortable. This qualitative data would then be quantified, thus yielding quantitative measures for ride comfort. During these tests, sensors on the

vehicle would output vehicle motion such that correlations can be determined between test subject responses and the dynamics of the vehicle.

This is what one ultimately wishes to understand about ride comfort, i.e. its correlation with the vehicle's motion (dynamic signals such as acceleration or jerk), such that the vehicle's design can be influenced in a way that corresponds to maximizing passenger comfort. However, there are not many passenger-comfort experiments available in the literature, especially those which have well accounted for various ages, physiques, and other subject-dependent criteria.

Due to the subjectivity of what everyone may experience in the test, it is rather difficult to come up with a unique measure of ride comfort using passenger test data. Wang et al.[1] stated that comfort can substantially enhance people's acceptance of autonomous vehicles and argued that ride comfort is mostly associated with vehicle's acceleration and that their comfort measure correlates most significantly with a linear combination of all four lateral/longitudinal acceleration/jerk signals. However, their comfort criterion has correlation discrepancies against gender and the direction of motion (longitudinal/lateral).

Hoberock[3] conducted an experimental study to determine a longitudinal ride comfort measure. Their study suggests that longitudinal acceleration must be kept below 0.15g and jerk below 0.3 g/s for a comfortable ride. However, they mention that due to an unavailability of a robust testing method, such experimental results are not repeatable and argue that test passengers "learn" the test process which changes their response and perception of ride comfort. Oborne[4, 5] published a critical assessment of the available experimental studies on passenger comfort with respect to vertical vibrations and argued that said experimental tests were inconclusive and that their results have barely benefited the design engineers as their multiple conclusions do not comply with one another. For instance, they point out that the same vertical acceleration in magnitude and frequency

(0.01g at 10 Hz) was perceived quite differently in the available ride comfort studies within the literature, ranging from “more than uncomfortable”[6] to “Just above threshold”[7] and “almost very good”[8].

Yang et al.[9] reviewed several published experiments on vibration comfort. In their rather extensive research, it was found that the available literature is discrepant when it comes to determining ride comfort levels. They argued that a peak acceleration value of 0.3 m/s^2 corresponded to conflicting indications of comfort amongst the various sources including “almost uncomfortable”[10], “almost perceptible”[11], “comfortable”[12], “not uncomfortable”[13, 14], and “very unsatisfactory”[15]. Multiple studies, the most recognized of which being the ISO2631[16], rely on the premise that acceleration is the proper measure of ride comfort where the smaller the acceleration, the more comfortable the ride.

The ISO2631 is an ISO standard on human whole-body vibrations that chooses acceleration as the responsible agent for ride comfort and suggests frequency weighting filters for the acceleration signal in the vertical, lateral, and longitudinal directions to account for humans’ perception of vibration intensity. Afterwards, a net value of the filtered acceleration signal is calculated and cross-referenced with the ranges given by ISO2631 for thresholds of comfort[16]. Many studies have adapted ISO2631 into developing further comfort criteria[17]. One study has combined ISO2631’s frequency weightings into a weighted-average acceleration magnitude as a ride comfort measure. This “total” acceleration is the magnitude of the $(1.4a_x, 1.4a_y, a_z)$ vector where a_x, a_y, a_z are the longitudinal, lateral, and vertical components of the acceleration vector, respectively [1]. However, some researches argue that ISO2631 has underestimated non-vertical vibrations. [3], [18], [19].

Chen et al.[20] took ride comfort to be associated with the RMS[1] net acceleration and proposed a suspension configuration which improved their introduced ride comfort index by 17%. Soliman et al.[21, 22] studied optimal suspension parameters and road roughness conditions for passenger comfort. Abernethy et al.[23, 24] suggest that the maximum deceleration rate that allows for seat retention in public transportation is around 0.3g which is significantly smaller than a previous threshold found by the same author. They argued that while jerk impacted the passengers' perception of ride comfort, it did not affect seat retention. Martin et al.[25] suggest 0.9 m/s^2 and 0.6 m/s^3 for peak levels of acceleration and jerk, respectively, for a comfortable ride. Elbanhawi et al.[26] has stated that passenger comfort in autonomous vehicles is associated with proper path planning just as much as having the appropriate vertical motions; since following a continuous, smooth trajectory tracking leads to smaller horizontal jerk and acceleration.

One experiment studied the driver's head motion and its correlation with comfort and stated that the perception of ride comfort comprises two main motion-related feelings, namely the floating feeling, and the body-toss feeling. And they further state that ride comfort is in inverse correlation with the head's absolute vertical velocity and pitch angular acceleration, respectively[27]. Another study correlated ride comfort with the vehicle's lateral and roll motions[28].

Another major type of discomfort which could affect one's perception of ride comfort is Motion Sickness. From a vibration perspective, motion sickness is essentially a frequency-based phenomenon, as vibrations within certain frequency ranges are known to cause motion sickness[2]. In a subjective experimental survey, Griffin et al.[19] stated that motion sickness is primarily due to low-frequency lateral oscillations and that most studies that associate motion sickness with

[1] Root Mean Square

vertical vibrations are underestimating low-frequency lateral vibrations. They also urged that the vehicle's heave, pitch, and roll motions do not contribute much to motion sickness. In another study they later gave a lateral acceleration frequency weighting filter for motion sickness which maintains vibrations from 0.0315 Hz to 0.2 Hz and then diminishes with a rate of 40dB/decade until 0.8Hz, indicating that tendency for motion sickness is worst at 0.2 Hz lateral oscillations[29].

Parsons et al.[30] performed laboratory tests on human subjects for a select range of typical ride frequencies and determined the threshold allowable levels of acceleration for all spatial degrees of freedom (6 DOF[2] i.e. heave, lateral, and longitudinal translations along with yaw, pitch, and roll rotations) before subjects declared discomfort. They also performed ride comfort passenger tests on standard roads and stated that in a standard road test none of the individual accelerations exceeded the laboratory threshold.

Jerk, being the time-derivative of acceleration, has recently come into attention as a potential metric for ride comfort. One study collected a list of research articles published within the past 5 years that included the term "jerk" in their title and demonstrated how a rather significant faction of them had discussed the incontrovertible correlation between jerk and passenger discomfort in vehicles[31]. As there is no widely established jerk sensor which could directly measure that signal, jerk is usually estimated by calculating the time-derivative of the acceleration. However, merely differentiating the acceleration signal creates significant noise and high-frequency behavior. Therefore, to appropriately employ jerk in ride comfort evaluation studies, the signal must first be properly filtered. Nakazawa et al.[32] devised transfer functions between acceleration and jerk using H-∞ control. Another study performed sudden-braking tests with passengers and

[2] Degree Of Freedom

argued that jerk plays an important part in the passenger's perception of ride comfort as they demonstrated how a higher jerk corresponded to a significantly higher percentage of people who had declared discomfort, even though the acceleration levels were held constant[33, 34]. In another jerk-based study, Huang et al.[35] found out that gear shifts affect longitudinal jerk and subsequently its implication for ride comfort.

In an experimental research by Mitsubishi Motors Corp., Hayafune et al.[36] argued that a comfortable ride is one whose peak values for lateral acceleration and lateral jerk fit within a comfort oval with its major and minor axes being lateral acceleration and lateral jerk, with semi-axis values of $0.5g$ and $0.15g/s$, respectively. Another study implemented jerk in its comfort metric to design a vehicle suspension unit[37]. One other study performed parameter identification for an electric vehicle implementing an anti-jerk control strategy[38]. Khorram et al.[39] correlated the level of longitudinal jerk with crash-related dangerous driving in an experiment involving 176 bus drivers in Tehran, Iran. Scamarcio et al.[40] adopted jerk as their comfort index and compared various anti-jerk controllers for development of electrical vehicle powertrains[40].

The US Army Tank Automotive Center conducted an experiment led by Pradko and Lee in 1966 where in a passenger test, they urged that the passengers' perception of ride comfort did not correlate well with acceleration data, whereas it agreed rather promisingly with data for "Average Absorbed Power", a quantity that is proportional to the square of the acceleration signal (similar to a power spectral density) with a proportionality constant that is only frequency-dependent and is constant for any individual frequency[41]. This research culminated in an industrial standard known as Adjusted Absorbed Power or AAP which states that a ride is comfortable as long as the adjusted absorbed power remains below 6 Watts.

Besides ISO2631 and AAP, other industry-adopted ride comfort standards include the acceleration-based VDI-2057 from Germany[42], and the acceleration-based BS-6841 from the UK[43]. In a study to investigate the applicability of the four aforementioned established industrial standards to ride comfort in off-road vehicles, Els[44] argued that while the four ride comfort standards had similar predictions for conservative ride conditions and that they agreed on the trend that higher acceleration exacerbates the perception of ride comfort, they did not agree on ride comfort thresholds, as a ride scenario could be perceived as comfortable according to one standard and uncomfortable according to another. Amongst Els' findings was another keen observation: their study shows that ride comfort is subjective, as the same ride had been perceived differently among people who had different occupations, such that the managers had rarely found a ride comfortable whereas soldiers rarely found one uncomfortable.

Ride comfort metrics have been employed to design optimal vehicle suspension systems[20, 37, 45]. Yet if the adopted ride comfort criterion should be different, so will be the accordingly-designed suspension systems and their performance. This further clarifies the need for a unifying, inclusive ride comfort index. In a study performing both experimental and numerical analysis of ride comfort, it was argued that vertical acceleration alone does not suffice for estimating ride comfort and that pitch and roll accelerations must also be considered[46]. Often concerns regarding passenger comfort are employed in the design of a vehicle's suspension system. However, a seat-specific suspension could be designed to improve passenger comfort, as most vibrations coming into the passenger body originally come through the seat[47]. Shurpali et al.[48] designed a seat suspension accordingly and argued how seat suspension enables enhanced passenger comfort.

In a rather different approach to ride comfort, Kasaiezadeh et al.[49] argued that it is fatigue that causes passenger discomfort and made an analogy between the stress a mechanical part undergoes and the acceleration that the human body experiences during car rides. They employed Goodman's fatigue criterion and came up with mean acceleration for ride comfort.

Judging from the aforementioned studies and how their introduced metrics for passenger comfort are in partial defiance of one another, it can be concluded that a universal ride comfort index does not yet exist and that currently established indices are prone to subjective discrepancies.

It is once again stressed that ride comfort is ultimately affected by many non-mechanical factors as well (visual disturbances, temperature variations, indigestion, etc), yet the scope of this study solely involves the mechanical implications of ride comfort. Much like cold being merely the absence of heat, comfort seems to virtually be the lack of discomfort. If the human body undergoes vibrations which would make it feel uncomfortable, that will have to be felt as the result of a nervous connection transmitting signals of pain/discomfort. Since the body's musculoskeletal system (the body's internal mechanical domain) is essentially responsible for "taking in" and "feeling" said input motions to the body, any motion-induced discomfort must correspond to a nervous signal coming from the musculoskeletal system. And those nerves in turn are associated with "changes" within the musculoskeletal system which are in fact the body's internal dynamics.

The author hereby claims that knowledge of the internal dynamics of the body in response to the disturbance input vibrations correlates with the nervous signals which "feel" the input motion and therefore constitute one's perception of comfort/discomfort. Hence, it is proposed that through modeling the body's internal dynamics in response to the input motions from a vehicle, one could determine whether said ride is comfortable or not. The author hypothesizes that if the body's internal mechanics are adequately modeled, one can correlate its response to input vibration with

feelings of discomfort. If motions from the internal dynamics model exceed their respective comfortable range of motion, this will signify discomfort. In other words, one could describe a most comfortable ride as one that during which the least amount of internal motion/reaction is induced within the human body; and that the higher the levels of internal motion/reaction, the higher the discomfort.

To address the lack of a ubiquitous ride comfort index, a quantitative ride comfort metric will be developed that can estimate the effect of input vibrations on the passenger's body and make a comfort inference according to its internal, dynamic response. Should such a metric be available, one can associate controllable vehicle outputs with ride comfort and develop vehicle control algorithms accordingly or design vehicle systems to achieve maximum ride comfort. This provides the motivation for developing a biomechanical model of a vehicle's passenger. This model should be sufficiently sophisticated to include the necessary degrees of freedom while still not being too complicated to prevent intuition. Henceforth this proposed biomechanical model will be known as the Passenger Model.

There are biomechanical passenger models available in the literature which have been utilized in the design of a vehicle seat[50, 51] suspension system[52]. Most such models have exclusively studied the vertical motion within the body, as it has been argued that it is the vertical vibrations, also known as the heave motion, that impacts ride comfort the most[16]. These models have treated the entire body as one or a few mass/spring elements sequentially placed only vertically[53-55]. Kim et al.[56] determined the necessary number of lumps to consider in a biomechanical model that would correspond well with experimental tests in terms of the vibration transmissibility. In an experiment involving a dual-axis vibration table set-up, Kozawa et al.[57] argued that the most significant input motions from a vehicle that contribute to a passenger's perception of discomfort

are mainly the seat's hip cushion's vertical vibrations, and the seat's backrest cushion's vertical/longitudinal vibrations, and not those that come in through the feet. Therefore, the proposed biomechanical model needs only include the upper body. The upper body's mechanical structure primarily consists of the human spine stretched between the pelvis and the head, as shown in Fig.1. Because of the spine's inherently curved, S-shaped geometry[58], even if it is only the vehicle's vertical vibration input that is to be considered, its mechanical effects within the body still cannot be properly accounted for using a vertical-only model. Consequently, the model of interest needs to encompass the necessary degrees of freedom, but not more, to maintain simplicity and yield physical intuition.

According to [57], the comfort-determining vibrations lie in the vehicle's pitching plane, i.e. the plane within which the vehicle rotates around its lateral axis. Said plane includes the cruise (longitudinal) and heave (vertical) translations as well as the pitch rotation. In anatomical terms, that plane coincides with the sagittal plane, which is defined as the longitudinal plane that divides a bilaterally symmetrical body into right and left sections. The spinal column itself is made up of three major sections which are distinguished from one another according to changes in the direction of spinal curvature[58]: the lumbar spine (lowermost section), the thoracic spine (middle section), and the cervical spine (uppermost section) as seen in Fig.1.

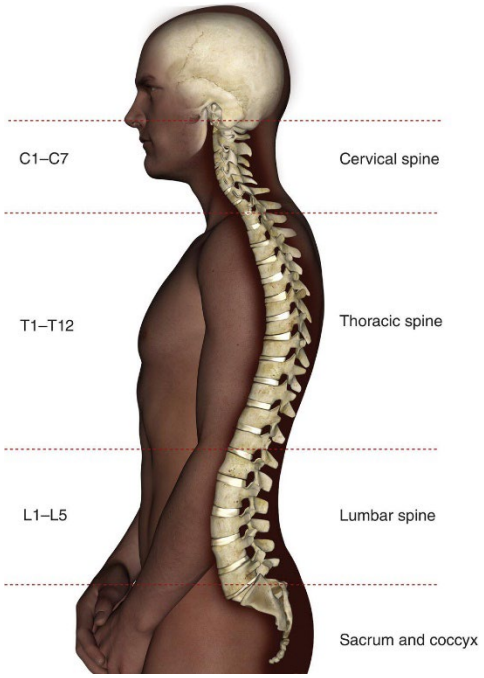

Figure 1 Sagittal view of the spinal column and its different sections[59]

The passenger model should account for the most prominent motions in the sagittal plane and the mechanical elements which affect them significantly. It should be noted that even though the model at hand is meant for the purpose of assessing a passenger's internal dynamics while aboard a moving vehicle, its design is sufficiently generic to be used in any application that requires a biomechanical model of the upper body in the sagittal plane.

1.1.Conclusion

Discrepancies within the established ride comfort metrics provide the motivation for developing a new metric according to passenger biomechanics. This requires a biomechanical model of the upper body that includes the sagittal degrees of freedom. Once the model is developed it can be exposed to disturbance input vibrations from the vehicle and its response can be employed in devising a ride comfort index which interprets the most comfortable ride as one that induces the smallest internal displacements within the passenger model.

2. The Biomechanical Passenger Model

Musculoskeletal biomechanical models have wide applications in ergonomics[60], rehabilitation[61, 62], and injury estimation[63, 64]. Their use can be extended to quantitatively explain and estimate ride comfort for a vehicle's passenger. A biomechanical model of the upper body in the sagittal plane is constructed which allows for curved motion to simulate the propagation of disturbance energy within a seated passenger aboard a moving vehicle. The model provides analytical and geometric intuition into the motion of the various segments of the upper body using a few simple geometric assumptions and can be employed to develop a quantitative ride-comfort metric, such that the most comfortable ride would be that which would induce the least internal motion within the passenger model.

2.1. Modeling

The passenger model should account for the most prominent motions in the sagittal plane and the mechanical elements which affect them significantly. It should be noted that even though the model at hand is meant for the purpose of assessing a passenger's internal dynamics while aboard a moving vehicle, its design is sufficiently generic to be used in any application which requires a biomechanical model of the upper body in the sagittal plane.

2.2. Building Blocks and Structure

Decades-long cohort studies have shown that lower-back pain, a medical condition associated with the lumbar spine, is among the most common and costly musculoskeletal disorders[65]. Amidst the three different spinal sections, the lumbar spine bears the highest portion of the weight of the upper body, has the largest range of motion[58], and is closest to the load input (hip cushion) for

a vehicle passenger. It is also evident that the lumbar spine is prone to the highest levels of chronic and acute pain[58]. Thus, the lumbar spine is of utmost importance when constructing a biomechanical model of the upper body. The lumbar spine itself comprises five lumbar vertebrae, named L1 through L5 that sandwich the intervertebral discs which are named according to the vertebrae to which they are attached on either side and provide compliance and damping. The vertebrae are mechanically much harder than the discs[66] and are therefore modeled as rigid body inertias, while representing the disc material as springs and dampers.

The thoracic spine is the middle segmental column of the upper body which in reality is connected to the ribcage and shapes a relatively rigid casing around the internal organs. Morita et al. showed that thoracic range of motion is significantly smaller than that of the lumbar [67]. Also, the thorax altogether is one relatively large inertia, almost an order of magnitude more massive than the most massive lumbar vertebra[68]. Subsequently, it is reasonable to assume the entire thorax as one rigid body despite entailing 12 of the total of 33 vertebrae in the spinal column[58].

The head rests on the neck that comprises 7 cervical vertebrae[58]. Generally, the cervical vertebrae have significant range of rotary motion with respect to one another However, a vehicle's passenger would most probably be looking ahead, and the motions induced by a vehicle would not be outside a linear range of motion. Thus, one equivalent neck joint is used to adequately approximate the cervical spine in this model.

At the bottom of the passenger model lies the pelvis which is modeled as a large inertia that serves as base for the rest of the passenger model.

Another mechanical element in the upper body which could affect internal sagittal motions is the musculature. There is a plethora of muscle fibers pulling on various vertebrae but they are clustered

into main muscle groups[69]. In the sagittal plane, muscles are either flexors which bend the upper body forward, or extensors that bend it backwards. Due to the seat's backrest, for the case of a seated passenger there would generally be no extension motion as a passenger cannot bend backwards with the seat's backrest at their back. Therefore, only extensor muscles are of interest. Additionally, the low-amplitude flexion motions of a passenger would generally include no active bending such as a case of intentional, large-scale forward bending. Hence, muscles would be modelled to act only passively, which can be approximated by an elastic resistance to tension. Consequently, one local multifidus muscle is considered for each lumbar vertebra, and one global longissimus muscle is considered for the thorax. Muscles are attached to the pelvis and passively resist forward bending if in tension.

The only remaining part of the upper body would be the arms. The arms are excluded from the model given that the passengers of an autonomous vehicle would most likely have their arms rest on their laps and therefore they wouldn't impact sagittal motions significantly. However, having the arms resting on a steering wheel would somewhat affect the dynamic response of the model as shown in [70].

Finally, the seat acts as the source of input excitations coming from the vehicle and includes a hip cushion, modeled as a translational point mass plus a spring and a damper, and two backrest cushions for lumbar and thoracic support which are modeled as springs and dampers. These supports exert forces on the passenger model in a direction perpendicular to the seat.

The planar degrees of freedom within the geometry of the sagittal spine correspond to axial displacement (tangent to the spine along the spinal cord), anterior-posterior shear displacement (perpendicular to the spine and the spinal cord), and flexion/extension rotation (bending forward or backward) as shown in Fig.1. These directions constitute the necessary and sufficient degrees

of freedom for constructing a passenger biomechanical model which can appropriately investigate the propagation of a vehicle's major input vibrations within the body. To sum up, the passenger model would include eight inertias including Pelvis, L5 through L1 vertebrae, Thorax, and the Head. In between all these would be elements that provide stiffness and damping. Each inertia has three sagittal degrees of freedom, and the hip cushion has one degree of freedom perpendicular to the seat. This results in a 25-DOF model. A schematic of the model is shown in Fig.2.

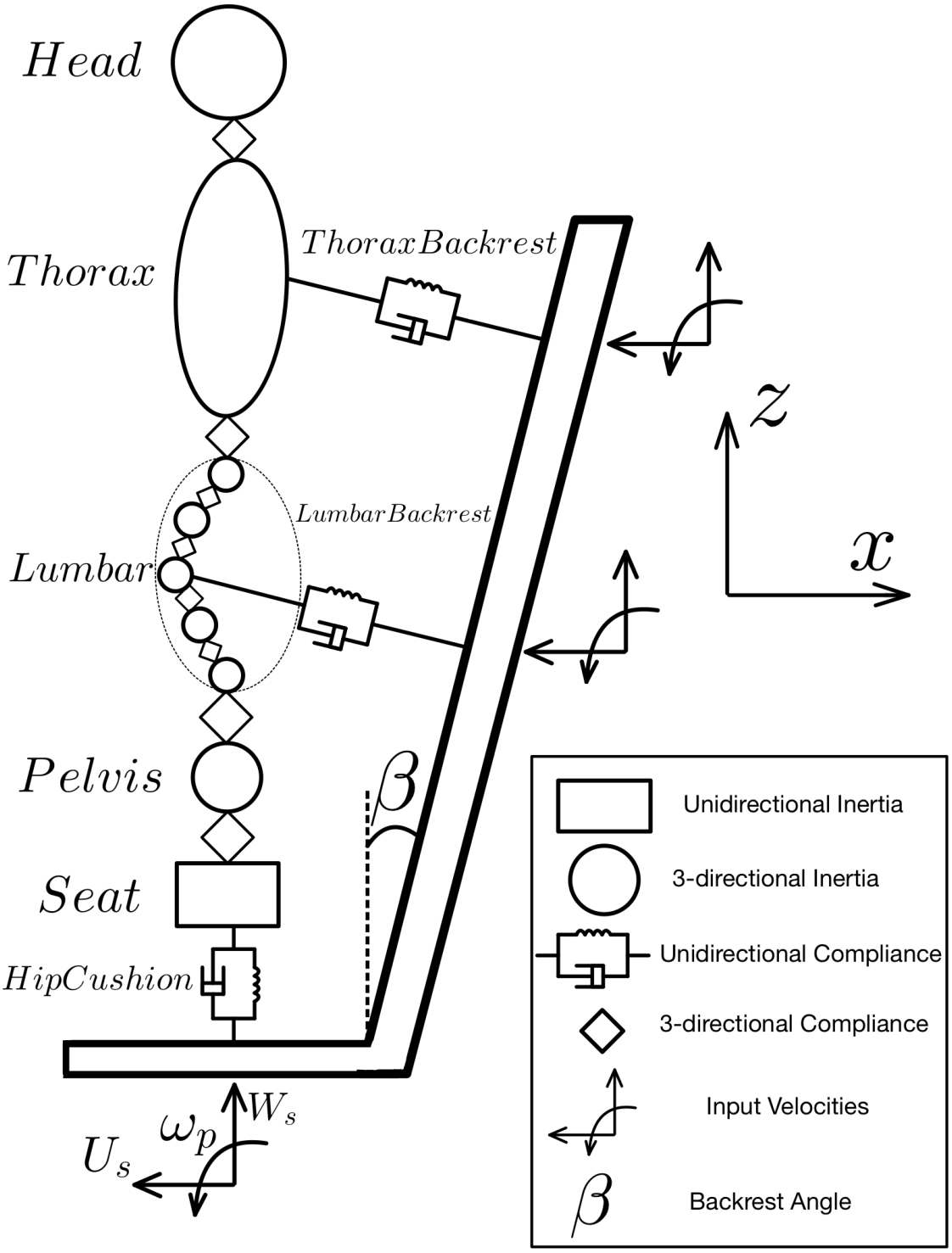

Figure 2. Schematic of the passenger model

The rhombus shapes in Fig.2 represent 3-directional spring/damper elements which provide stiffness and damping in all 3 axial, shear, and rotary directions. There is also a distinction between the seat mass which can only move perpendicular to the hip cushion, and the remaining inertias which can both translate and rotate in the sagittal plane and have a rotational inertia component as well as mass. Furthermore, the input signals to the passenger model are heave (vertical W_s), cruise (longitudinal U_s), and pitch (rotational ω_p) velocities which come from a separate vehicle model and are calculated at the point of contact of the seat with the passenger model using velocity transfer from the vehicle's center of gravity. Also, the seat is allowed to have a backrest inclination angle β which is zero if the seat is upright.

2.3.Physical Assumptions

The most prominent physical assumption in developing the passenger model is perhaps how force-generating elements, i.e. springs and dampers, have linear constitutive behaviors. This means that spring forces are proportional to the displacement across the spring, and damper forces would be proportional to the relative velocity across the damper. In reality, it is known that such elements do not generally display linear behavior[71] and are prone to non-linear effects such as viscoelasticity, poroelasticity, and hysteresis[72, 73]. However, studies show that the force-generating elements behave rather linearly in the low-amplitude range of motion, for both rotation[74], and translation[75]. Given that this model is not intended for large displacements, or impact-loads, assuming linear constitutive behavior for force-generating elements is reasonable.

2.4.Geometry and Kinematics

The model accounts for the curved geometry of the spine. Therefore, body-fixed, curvilinear coordinates are used and each inertia is assumed to have three sagittal velocity components: a

tangential velocity V_t along the spinal cord, a normal velocity V_n perpendicular to it, and an angular velocity ω. Also, to have access to the angular orientation of each inertia, the angle θ is designated as the angle that the tangential velocity component makes with respect to the inertial x direction, as depicted in Fig.3.

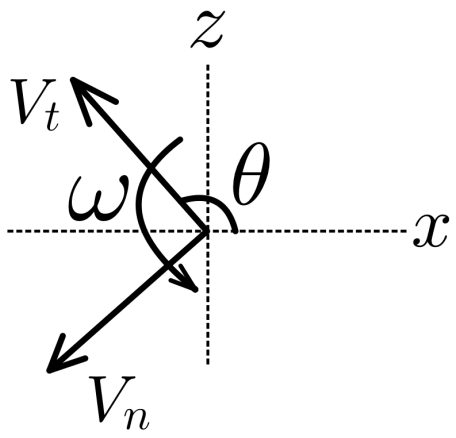

Figure 3. Body-fixed velocities for each inertia

The body-fixed velocities can be projected along the inertial directions and integrated so as to obtain inertial displacement and angular positions.

$$\theta(t) = \int \omega \mathrm{d}t + \theta_0$$

Eq. 1

$$x(t) = \int (V_t \cos\theta - V_n \sin\theta)\mathrm{d}t + x_0$$

Eq. 2

$$z(t) = \int (V_t \sin\theta + V_n \cos\theta)\mathrm{d}t + z_0$$

Eq. 3

Where $x(t)$ and $z(t)$ represent the instantaneous translational position of the center of gravity of the inertial element with respect to the inertial x-z frame and θ(t) indicates its angular position with respect to positive x-direction. The coordinate origin is the seat base in the hip cushion.

The instantaneous directions of axial compliance and shear compliance need to be expressed in terms of the instantaneous positions of the inertias. The cornerstone in shaping the geometry of this model is the assumption that the intervertebral axial compliance lies in the direction of the line that connects the centers of gravity for the two adjacent inertias. Once that direction is obtained, the direction of the shear compliance would be perpendicular to that line. In an exaggerated fashion for the purpose of clarity, Fig. 4 shows the centers of gravity for two consecutive top (T) and bottom (B) inertias along with their individual velocity components and the directions for axial and shear compliance.

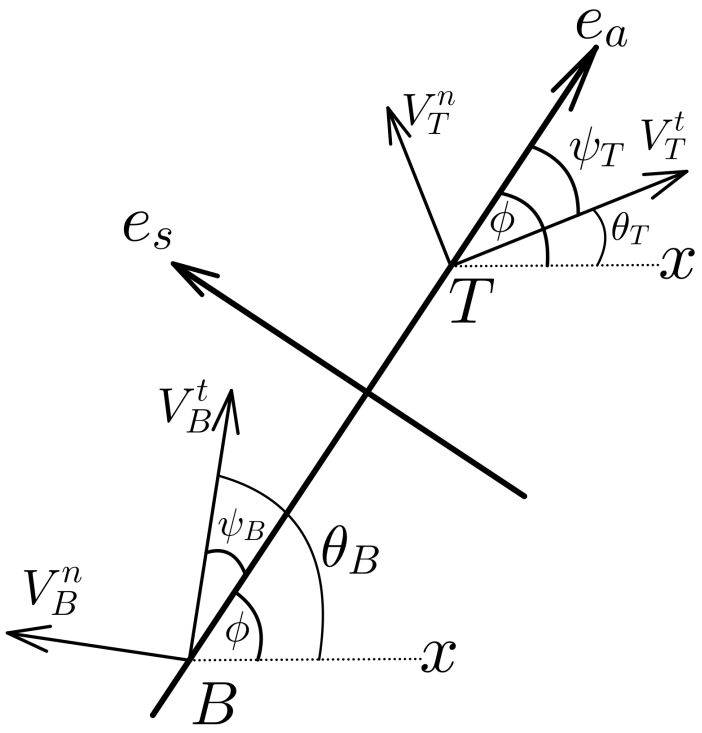

Figure 4. Directions for axial and shear compliance

Axial and shear forces would respectively be in the direction of $\mathbf{e_a}$ and $\mathbf{e_s}$ which are unit vectors for axial and shear directions and are determined by the angle φ. The φ angle can be obtained in terms of inertial positions according to Fig.4 as follows:

$$\varphi = \tan^{-1} \frac{z_T - z_B}{x_T - x_B}$$

Eq. 4

It's noteworthy that the two inertias share a φ angle which would thusly be uniquely found, as both $z_T - z_B$ and $x_T - x_B$ are individually available. In turn, the contribution of the intervertebral compliance forces to the body-fixed velocities would be determined by the difference of the φ angle and the inertia's individual θ angles, which are denoted with ψ_T for the top and ψ_B for the bottom inertia. With knowledge of φ, ψ_T and ψ_B are calculated as:

$$\psi_T = \varphi - \theta_T \quad ; \quad \psi_B = \theta_B - \varphi$$

Eq. 5

Multiple geometric dimensions for the model have been extracted from the literature. In addition, a CAD model which itself was constructed from CT-scan images from a healthy human subject with no history of lower-back pain was used for complimentary geometric information[76].

Since the equations of motion were derived using bond graph modeling[77], it was necessary to obtain the relative velocities across force-generating elements, i.e. intervertebral discs and muscles. For this purpose, the velocity vectors of inertias on either side would first have to be transferred from the center of gravity to the disc interface and then projected along the disc's compliance directions. Since the inertias are modelled as rigid bodies with spatial dimensions, their velocity at the disc interface would be different from the velocity of their center of gravity.

For instance, the lumbar vertebrae have a half-thickness distance in the tangential direction from their center of gravity to the disc interface which contributes to changes in the vertebra's normal velocity at the disc interface as shown in Fig.5 as D_B and D_T.

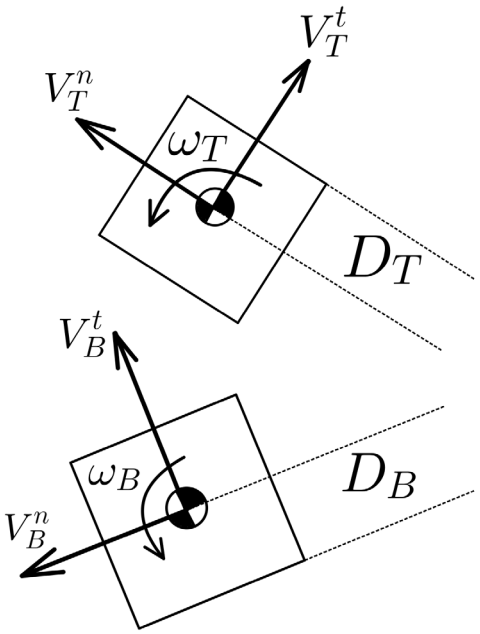

Figure 5. Schematic of the half-thickness dimension used for velocity transfer in lumbar vertebrae

According to Fig.5, velocity transfer from the vertebral center of gravity (CG) of each inertia to the top-bottom disc interface (TB) would look like:

$$\mathbf{V_{i,TB}} = \mathbf{V_{i,CG}} + \boldsymbol{\omega_i} \times \mathbf{D_i} \rightarrow {V_{B,TB}}^n = {V_B}^n + D_B\omega_B \quad ; \quad {V_{T,TB}}^n = {V_T}^n - D_T\omega_T$$

Eq. 6

The interface velocities are resolved into the compliance directions according to Fig.4:

$$\mathbf{V_{i,TB}} = \left({V_i}^t \cos\psi_i - {V_{i,TB}}^n \sin\psi_i\right)\mathbf{e_a} + \left({V_i}^t \sin\psi_i + {V_{i,TB}}^n \cos\psi_i\right)\mathbf{e_s}$$

Eq. 7

And the relative velocity and relative angular velocity across intervertebral discs can be found as:

$$\mathbf{V_{rel,TB}} = \mathbf{V_{B,TB}} - \mathbf{V_{T,TB}} = V_{rel,TB_a}\mathbf{e_a} + V_{rel,TB_s}\mathbf{e_s}$$

Eq. 8

$$\omega_{TB} = \omega_B - \omega_T$$

Eq. 9

Where the relative velocity is considered positive in compression.

Another force-generating element that requires explanation is the musculature. There are a total of 6 muscles considered in the model, one global longissimus muscle that attaches the thorax to the pelvis, and 5 local multifidus muscles that attach the individual lumbar vertebrae to the pelvis. The location of the pelvic attachment point and the vertebral attachment points for each muscle are extracted from Arjmand et al.[78]. Fig. 6 shows a schematic of muscle architecture.

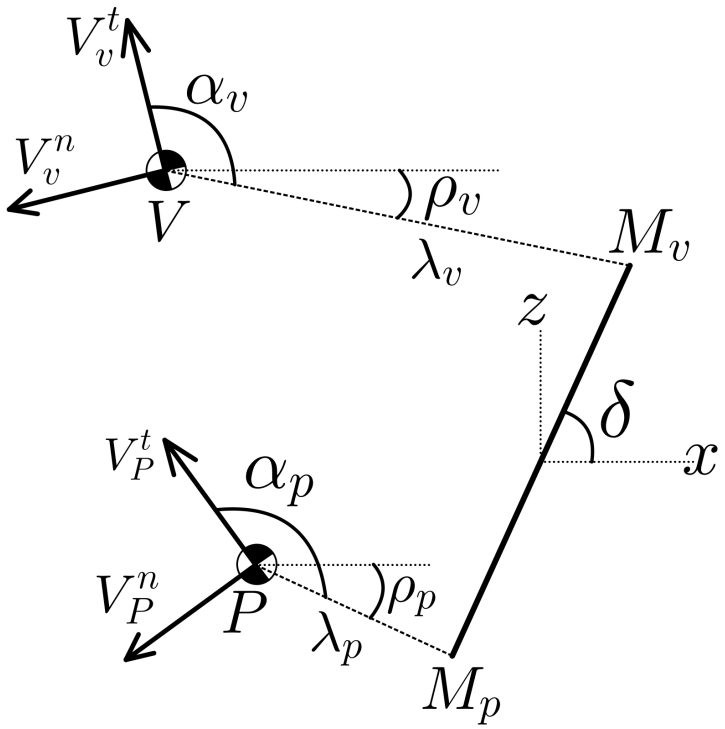

Figure 6. Schematic of muscle architecture in the model

In Fig.6, P and V denote pelvic and vertebral centers of gravity and p and v subscripts associate quantities with them, respectively. The angle α_i is the angle between the vertebral axis and the line that connects the vertebral center of gravity to the muscle attachment point. The length λ_i is the distance between the respective vertebral center of gravity and the muscle attachment point. Both α_i and λ_i are constants pertaining to each muscle and are obtained from[76]. The angle ρ_i is defined as the difference between α_i and the individual inertia's orientation angle θ_i.

$$\rho_v = \alpha_v - \theta_v \quad \& \quad \rho_p = \alpha_p - \theta_p$$

Eq. 10

Subsequently, the position of the muscle attachment point is calculated on both the pelvis (M_p) and the vertebra itself (M_v).

$$x_{M_i} = x_i + \lambda_i \cos \rho_i$$

Eq. 11

$$z_{M_i} = z_i - \lambda_i \sin \rho_i$$

Eq. 12

This allows for the calculation of the muscle orientation angle δ and the muscle initial length L_0.

$$\delta = \tan^{-1} \frac{z_{M_v} - z_{M_p}}{x_{M_v} - x_{M_v}}$$

Eq. 13

$$L_0 = \left|\overline{M_v M_p}\right| = \sqrt{\left(z_{0_{M_v}} - z_{0_{M_p}}\right)^2 + \left(x_{0_{M_v}} - x_{0_{M_v}}\right)^2}$$

Eq. 14

Where L_0 is the initial, unstretched length of the muscle. To find the relative velocity across each muscle, the velocity of muscle attachment points for both the pelvis and the vertebra are calculated using velocity transfer.

$$\mathbf{V_M} = \mathbf{V_{CG}} + \boldsymbol{\omega} \times \boldsymbol{\lambda}$$

Eq. 15

Given that the muscle orientation is different than the body-fixed orientation for each vertebra, all velocities are resolved in the inertial x-z frame (Fig.2) with respective **i** and **k** unit vectors.

$$\mathbf{V_M} = (V_t \cos\theta - V_n \sin\theta + \lambda\omega \sin\rho)\mathbf{i} + (V_t \sin\theta + V_n \cos\theta + \lambda\omega \cos\rho)\mathbf{k}$$

Eq. 16

Equation 16 can be used to yield the velocity of both M_v and M_p muscle attachment points and now the relative velocity across the muscle can be calculated in the x-z frame and then projected along the direction of the muscle itself which is determined by the muscle orientation angle δ.

$$\mathbf{V_{rel,m}} = \mathbf{V_{M_v}} - \mathbf{V_{M_p}} = V_{rel,m_x}\mathbf{i} + V_{rel,m_z}\mathbf{k}$$

$$V_{rel,m} = V_{rel,m_x} \cos\delta + V_{rel,m_z} \sin\delta$$

Eq. 17

Where $V_{rel,m}$ is a scalar value that indicates the relative velocity across the muscle, considered positive in tension as muscles could only withstand tension[79].

2.5.Equations of motion and kinetics

Between any two inertias there is an axial compliance, a shear compliance, and a rotary compliance which exert forces and moments on said inertias. Furthermore, all inertias except that representing

the head are subject to muscle forces which pull on them towards the pelvis. And finally, there are gravity forces acting vertically downward.

The described dynamics comprise a non-linear state space where the main state variables are the velocities of the inertias and the displacements across the compliances. Each inertia has three velocity states: tangential V_t, normal V_n, and angular ω and each compliance has three relative displacement states: axial q_a, shear q_s, and rotary q_r. Even though all energy elements (inertias, springs, and dampers) are considered to have linear constitutive behaviors, the dynamics are still non-linear, because of the system kinematics. Moreover, the state space is expanded to include auxiliary states which are not directly involved with storing or dissipating energy, but are necessary for developing the dynamics. These auxiliary states consist of the angular and translational positions of the inertial elements.

The translational and rotary intervertebral compliance elements (TB) generate respective forces and moments which depend on the relative displacements and velocities across said elements, where the displacement is the temporal integral of said relative velocity.

$$\dot{q}_{TB_i} = V_{rel,TB_i} \quad ; \quad \dot{q}_{TB_r} = \omega_{rel,TB_r}$$

Eq. 18

$$F^i{}_{TB} = k_{TB_i} q_{TB_i} + b_{TB_i} V_{rel,TB_i} \quad ; \quad M_{TB_r} = k_{TB_r} q_{TB_r} + b_{TB_r} \omega_{rel,TB_r}$$

Eq. 19

Similarly, for the muscles:

$$\dot{q}_m = V_{rel,m} \quad ; \quad F_m = k_m q_m + b_m V_{rel,m} \quad for\ q_m \geq 0$$

Eq. 20

The $q_m \geq 0$ condition ensures the muscle is in tension. In the equations above F denotes a force and M designates a moment. Also, k and b indicate linear stiffness and damping coefficients, the TB subscript indicates the top-bottom vertebral interface, and the m subscript pertains to a muscle. The i subscript indicates either of axial or shear, and the r subscript denotes rotation.

The acceleration vector in the rotating body-fixed frame would be:

$$\mathbf{a} = \frac{\mathrm{d}\mathbf{V}}{\mathrm{d}t} = \frac{\partial \mathbf{V}}{\partial \mathrm{t}} + \boldsymbol{\omega} \times \mathbf{V} = (\dot{V}_t - \omega V_n)\mathbf{e_t} + (\dot{V}_n + \omega V_t)\mathbf{e_n}$$

Eq. 21

Where $\mathbf{e_t}$ and $\mathbf{e_n}$ are tangential and normal unit vectors, respectively.

Every force, including gravity, has to be resolved in tangential and normal directions and then their moment around the center of gravity needs to be calculated. Fig.7 shows the direction of the gravity force in the body-fixed frame.

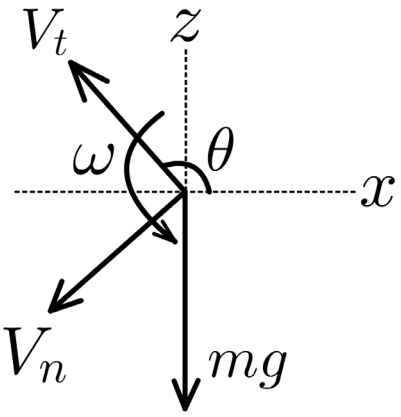

Figure 7. Direction of the force of gravity in the body-fixed frame

According to Fig.7, the force of gravity is expressed as:

$$\mathbf{F_g} = mg(-\sin\theta\,\mathbf{e_t} - \cos\theta\,\mathbf{e_n})$$

Eq. 22

The force of gravity has no moment about the center of gravity.

As for the intervertebral compliance forces, according to the employed sign convention with relative velocity being positive in compression, a positive force pushes the top inertia up and the bottom inertia down, as shown in Fig.8.

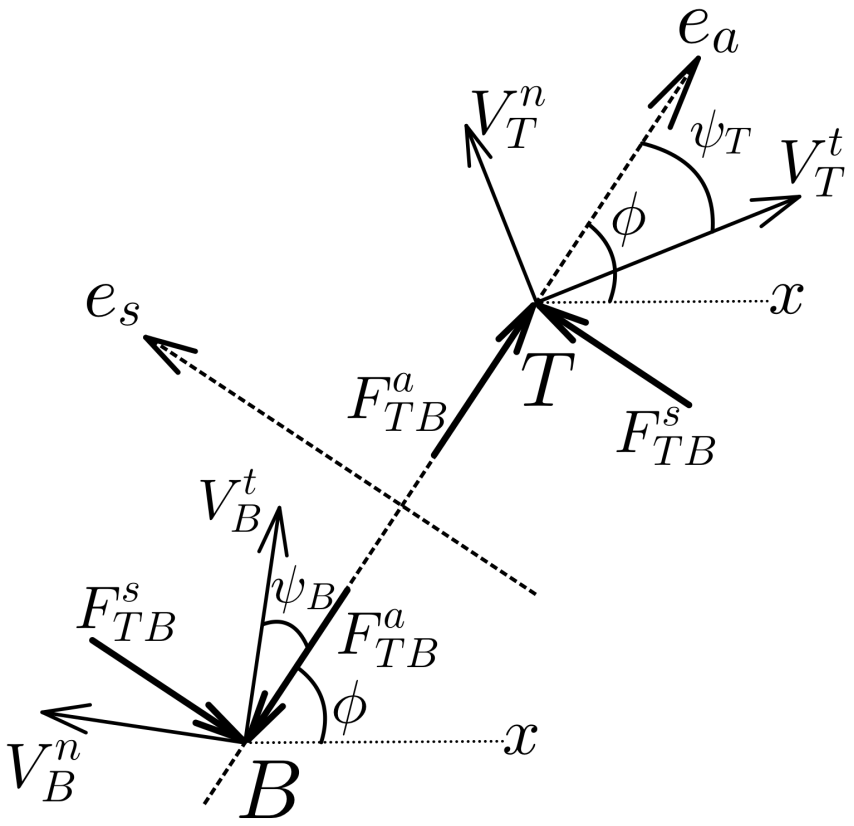

Figure 8. Intervertebral (TB) forces in action and reaction

The intervertebral (TB) compliance forces are now resolved in body-fixed directions. For the top inertia:

$$\mathbf{F_{TB,T}} = ({F_{TB}}^{a} \cos\psi_T - {F_{TB}}^{s} \sin\psi_T)\,\mathbf{e_t} + ({F_{TB}}^{a} \sin\psi_T + {F_{TB}}^{s} \cos\psi_T)\mathbf{e_n}$$

Eq. 23

And for the bottom inertia:

$$\mathbf{F_{TB,B}} = (-{F_{TB}}^{a} \cos\psi_B - {F_{TB}}^{s} \sin\psi_B)\,\mathbf{e_t} + ({F_{TB}}^{a} \sin\psi_B - {F_{TB}}^{s} \cos\psi_B)\mathbf{e_n}$$

Eq. 24

Amongst intervertebral (TB) forces, the axial force generates no moment because it passes through the center of gravity. However, the shear force exerts a moment on each body due to the half-thickness distance between the disc interface and the vertebral center of gravity. Fig.9 shows the orientation of the shear force with respect to the center of gravity.

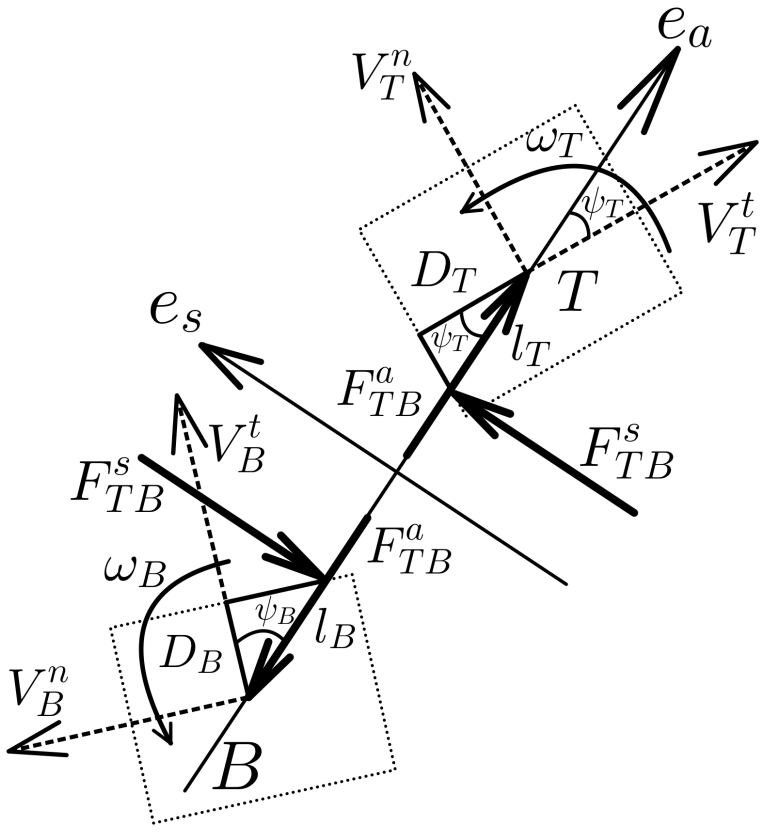

Figure 9. Orientation of the intervertebral shear force with respect to centers of gravity

The shear force has a moment arm with respect to the centers of gravity denoted with l_i :

$$l_i = \frac{D_i}{\cos \psi_i}$$

Eq. 25

The shear force's moment is then:

$$M_{s,TB}{}^{i} = -F_{TB}{}^{s} l_i$$

Eq. 26

It is noteworthy that the shear force opposes the rotation for both bodies.

With the relative muscle velocity being considered positive in tension, a positive muscle force pulls on both bodies along itself. Fig.10 shows the orientation of the muscle force on the vertebra and its reaction on the pelvis with respect to the body-fixed coordinates.

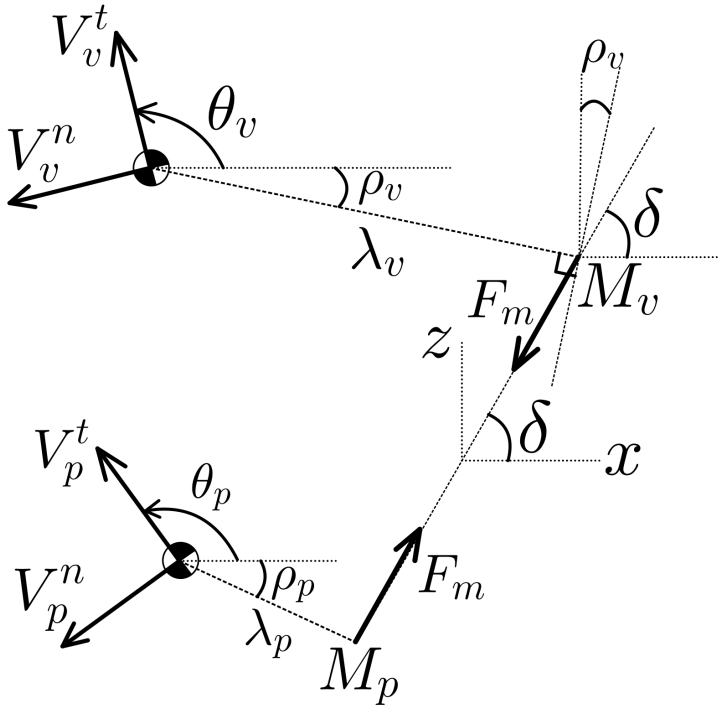

Figure 10. Orientation of the muscle force

The muscle force is expressed in body-fixed directions:

$$\mathbf{F_{m_v}} = F_m(-\cos(\theta_v - \delta)\,\mathbf{e_t} + \sin(\theta_v - \delta)\,\mathbf{e_n}) = F_{m_{v_t}}\mathbf{e_t} + F_{m_{v_n}}\mathbf{e_n}$$

Eq. 27

$$\mathbf{F_{m_p}} = F_m\big(\cos\big(\theta_p - \delta\big)\,\mathbf{e_t} - \sin\big(\theta_p - \delta\big)\,\mathbf{e_n}\big) = F_{m_{p_t}}\mathbf{e_t} + F_{m_{p_n}}\mathbf{e_n}$$

Eq. 28

The muscle force also produces a moment about the center of gravity for both the vertebra of interest and the pelvis. That moment is calculated according to Fig.10:

$$M_{m_v} = -\lambda_v F_m \cos\left(\frac{\pi}{2} - (\rho_v + \delta)\right) = -\lambda_v F_m \sin(\rho_v + \delta)$$

Eq. 29

$$M_{m_p} = \lambda_p F_m \cos\left(\frac{\pi}{2} - \big(\rho_p + \delta\big)\right) = \lambda_p F_m \sin\big(\rho_p + \delta\big)$$

Eq. 30

The last forces that need attention are those from the seat. Fig.11 schematically shows the orientation of the seat forces where H indicates the seat's base (hip cushion) and R_L, R_T denote the seat-contact point for the lumbar and thorax backrests, respectively. Also, d_L and d_H respectively indicate the distance between lumbar and thorax backrest contact points and the seat's base. And β is the seat backrest's inclination angle.

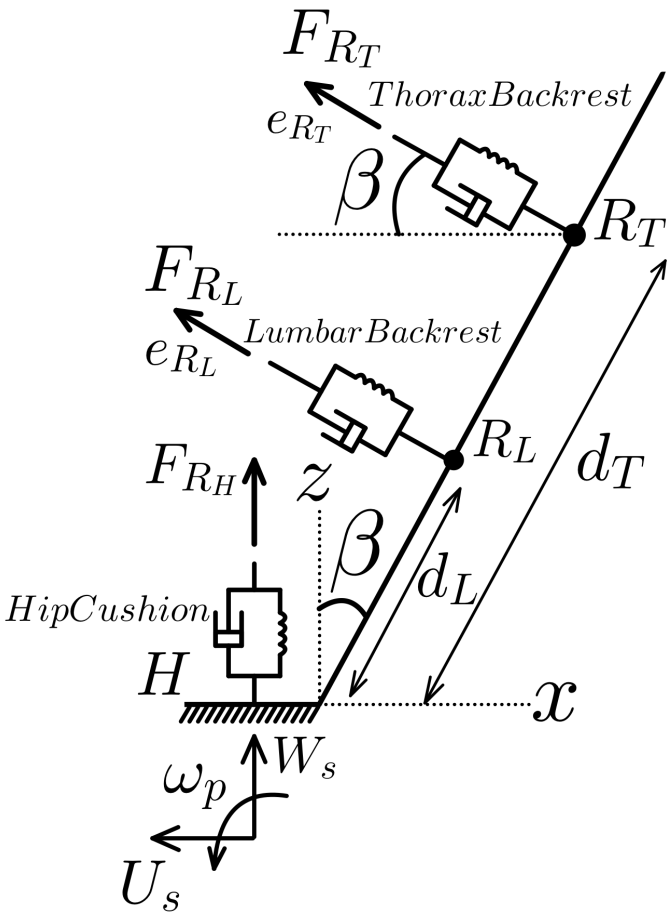

Figure 11. Orientation of the seat forces

The seat forces can only push on the passenger's body which means their associated compliance can only undergo compression, i.e., $q_R \geq 0$. All seat compliances act only in one direction, perpendicular to the seat's orientation at the contact point. The hip cushion and its associated mass can only move vertically with respect to the vehicle:

$$\dot{q}_{R_H} = W_s - V_{seat_H} \; ; \; F_{R_H} = k_{R_H} q_{R_H} + b_{R_H}\left(W_s - V_{seat_H}\right) \;\; for \;\; q_{R_H} \geq 0$$

Eq. 31

It is noted that F_{RH} does not generate any moment as the hip cushion's mass is considered to only move vertically.

To calculate the seat-backrest forces at either location, velocities of the two ends of the backrest compliance along its direction ($\mathbf{e_R}$) should be found. The backrest contact point on the seat needs a velocity transfer from the seat's base to the backrest's contact point as seen in Fig.11, thus:

$$\mathbf{V_R} = (U_s \cos\beta + W_s \sin\beta + d\omega_p)\mathbf{e_R}$$

Eq. 32

It is assumed that the seat backrest makes contact with the upper body at two points[53]: the lumbar backrest touches the lowest depression point on the lumbar spine at the spinous process of the L3 vertebra due to lordosis curvature, and the thorax backrest touches the highest protrusion point on the thoracic spine at the location of the spinous process of the T7 vertebra due to kyphosis curvature[58]. The dimensions of the vertebrae and the position vector that connects the inertia's center of gravity to the backrest contact point are extracted from the literature[68, 76]. Fig. 12 shows a schematic of the relative position of the seat backrest's contact point on the passenger body with respect to the associated inertia's center of gravity, where SP stands for spinous process and D_x and D_z are its distance from the vertebral center of gravity in inertial x-z directions.

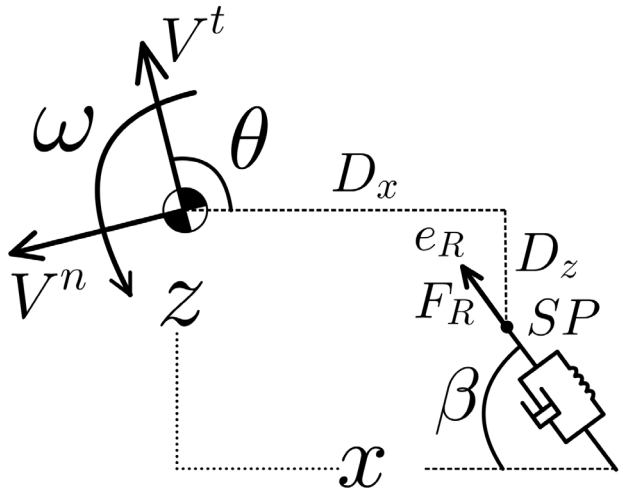

Figure 12. The orientation of the backrest force with respect to the center of gravity of the associated inertia

The velocity of the spinous process is resolved in the backrest compliance's direction:

$$\mathbf{V_{SP}} = (V^t \cos\theta - V^n \sin\theta + \omega D_z)\mathbf{i} + (V^t \sin\theta + V^n \cos\theta + \omega D_x)\mathbf{k}$$

$$\mathbf{V_{SP}} = V_{SP_x}\mathbf{i} + V_{SP_z}\mathbf{k} = \left(-V_{SP_x} \sin\beta + V_{SP_z} \cos\beta\right)\mathbf{e_R}$$

Eq. 33

Now the seat backrest (SBR) force along the compliance direction can be calculated.

$$\mathbf{V_{rel_{SBR}}} = \mathbf{V_R} - \mathbf{V_{SP}} = V_{rel_{SBR}}\mathbf{e_R}\ ;\ \dot{q}_{SBR} = V_{rel_{SBR}}\ ;\ F_{SBR} = k_{SBR}q_{SBR} + b_{SBR}V_{rel_{SBR}}$$

Eq. 34

From Fig.12, the seat backrest force makes an angle equal to π-(β+θ) with respect to the tangential velocity of its associated inertia. The seat backrest force and moment become:

$$\mathbf{F_{SBR}} = F_{SBR}(\cos(\pi - (\theta + \beta))\mathbf{e_t} + \sin(\pi - (\theta + \beta))\,\mathbf{e_n})$$

Eq. 35

$$M_{SBR} = -D_z F_{SBR} \cos\beta + D_x F_{SBR} \sin\beta$$

Eq. 36

With all the acting forces and moments expressed in their respective body-fixed frames, the equations of motion become:

$$m\dot{V}^t = m\omega V^n + \sum F_t \quad ; \quad m\dot{V}^n = -m\omega V^t + \sum F_n \quad ; \quad J\dot{\omega} = \sum M$$

Eq. 37

The equations of motion are extensively given for the L3 vertebra as an example, since its motion is relatively more involved as it experiences all the possible considered effects.

$$m_{L3}\dot{V}_{L3}{}^{t} = m_{L3}\omega_{L3}V_{L3}{}^{n} - m_{L3}g\sin\theta_{L3} + F_{L3L4}{}^{a}\cos\psi_{L3L4} - F_{L3L4}{}^{s}\sin\psi_{L3L4}$$
$$- F_{L2L3}{}^{a}\cos\psi_{L3L2} - F_{L2L3}{}^{s}\sin\psi_{L3L2} - F_{SBR_{L3}}\cos(\theta_{L3}+\beta) + F_{m_{L3_t}}$$

$$m_{L3}\dot{V}_{L3}{}^{n} = -m_{L3}\omega_{L3}V_{L3}{}^{t} - m_{L3}g\cos\theta_{L3} + F_{L3L4}{}^{a}\sin\psi_{L3L4} + F_{L3L4}{}^{s}\cos\psi_{L3L4}$$
$$+ F_{L2L3}{}^{a}\sin\psi_{L3L2} - F_{L2L3}{}^{s}\cos\psi_{L3L2} + F_{SBR_{L3}}\sin(\theta_{L3}+\beta) + F_{m_{L3_n}}$$

$$J_{L3}\dot{\omega}_{L3} = M_{L3L4} - M_{L2L3} - M_{s_{L3L4}} - M_{s_{L2L3}} + M_{m_{L3}} + M_{SBR_{L3}}$$

Eq. 38

The model is nonlinear as the equations of motion include rotating frame cross product terms as well as many trigonometric functions operating on the position states. It is also analytical since it does not involve geometric and numerical domain discretization like finite element methods do.

2.6.Initial Conditions

Each state requires an initial condition value. The initial condition for the auxiliary states including translational and angular positions of the inertias is extracted from the literature[68, 76]. The velocity states all have zero initial conditions. However, since the model is subject to gravity, the displacement states have non-zero initial conditions. Given how the equations of motion are heavily coupled, an analytic derivation of those initial conditions was not performed. Instead, the model was run with zero initial conditions and zero inputs, and the system was allowed to settle into a static equilibrium. The resulting displacement states were then saved as the initial conditions for ensuing runs of the model.

2.7.Parameter Investigation

There are as many as 79 parameters employed in developing the model, which include stiffness and damping coefficients associated with all compliances, as well as values for mass and moments of inertia for all inertial elements. While the fundamental dynamics depend on the modeling assumptions, the response-time history and the associated critical frequencies greatly depend on the parameter values. Parameters are extracted from the literature as best as possible. Finding the required parameters within the literature proved a challenge as no unique study has reported all 79 required parameters in the way identified in this study. Hence, the parameters needed to be extracted from various studies where differing experimental methods were used to obtain said parameters and therefore there is not total agreement among researchers. The highest level of confidence belongs to masses and moments of inertia, and they are extracted from[68, 80]. Stiffness parameters do not come with the same level of confidence, as most experiments that give values for these parameters are performed on cadavers and the force-generation mechanism for a living organism is not the same as a cadaver. And lastly, the least level of confidence belongs to the damping parameters which add time-dependence to the force-generation mechanism as well. Quite a few references were investigated to obtain the required stiffness and damping parameters, including but not limited to [22-25, 27, 44, 45]. It was observed that they did not agree on the lumping strategy for defining the parameters or on the parameter values. In some cases, they differed by an order of magnitude. Consequently, some biomechanical parameters, particularly the damping values, had to be modified from their initial values extracted from the literature to enable model validation against experimental findings. The initial values for the biomechanical stiffness and damping parameters were taken from [81] and [82], respectively.

Also, seat parameters were taken from [80]. For the muscles, Young's modulus E_m, damping ratio ζ_m, and cross-sectional area A_m were extracted from the literature, respectively[83-85] and the muscle stiffness and damping coefficients were calculated as follows.

$$k_m = \frac{E_m A_m}{L_0} \quad ; \quad b_m = 2\zeta_m \sqrt{k_m m_v}$$

Eq. 39

Where L_0 is the muscle's unstretched length and m_v is the mass of the vertebral body to which the muscle is attached. The parameters employed in this study are given in Tables 1-12.

2.8.Validation

Before the model can be used to make further inferences on the internal motions within the body, it needs to be validated, i.e., assert that it can predict reasonable outputs according to available literature. The present model has been validated against Pranesh et al.[70]. In their study, 12 seated human subjects with no history of lower-back pain were exposed to vibrations of vehicular nature with vertical excitations at the base. Using accelerometers, vibration transmissibility frequency responses were recorded at different locations of the upper body. Fig. 13 compares the vibration transmissibility as predicted by the model here with the experimental data from Pranesh et al.. Given that vertical vibrations are responsible for the majority of the perception of ride comfort, vertical vibration transmissibility is compared to Pranesh's experiment in three different locations: the L5 and L3 vertebra within the lumbar spine, and the head at the top of the model. Figs.13 (a) through (c) show this comparison. Also, the horizontal vibration transmissibility in response to the same vertical excitation at the base is investigated for the head in Fig.13 (d) to account for the fore-aft degree of freedom.

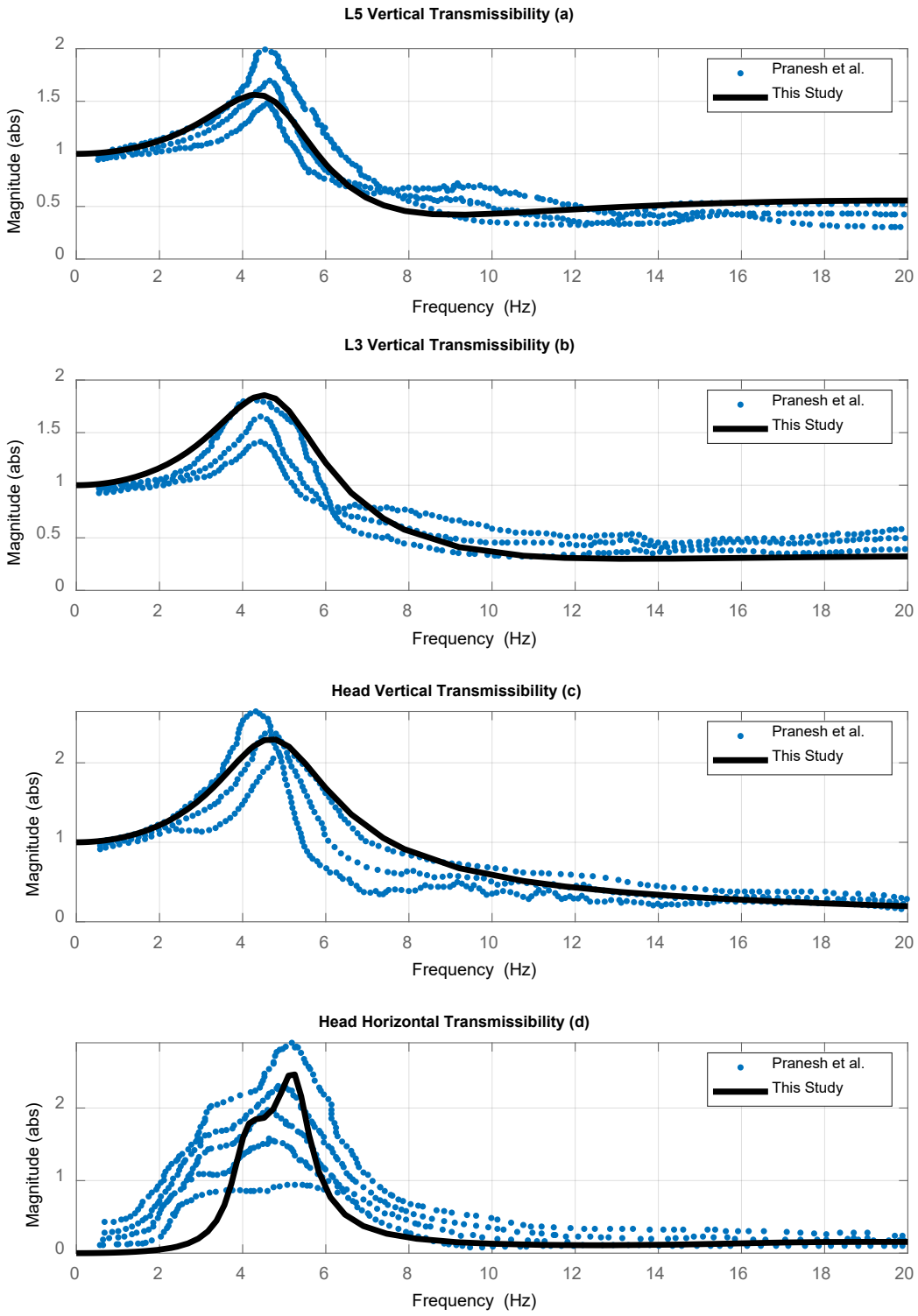

Figure 13. Comparison of vibration transmissibility between this study and Pranesh et al.'s experiment[70]

As seen in Fig.13, the model developed here agrees sufficiently well with Pranesh et al. in both magnitude and frequency content. This provides some confidence that this model can predict reasonably accurate results and could be further employed to make inferences regarding the body's internal dynamics.

2.9. Results and discussion

Fig. 14 shows the axial displacement deviation at various vertical locations for a unit heave-impulse at the base of the model.

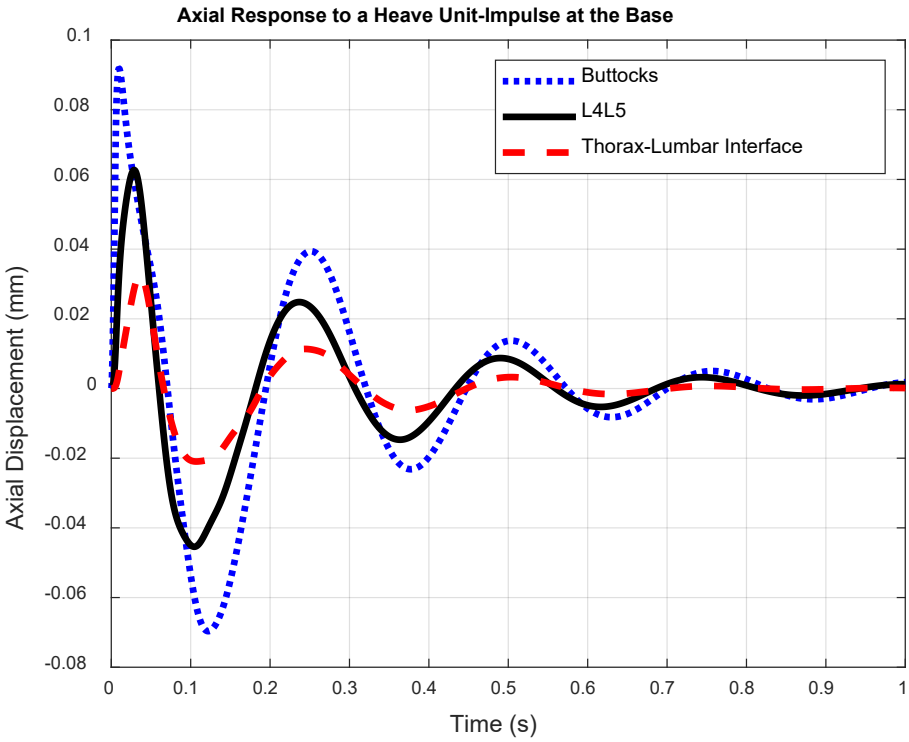

Figure 14. Wave-like propagation of an impulse within various sections of the model

Fig. 14 shows that, in those sections that are closer to the base, the effect of the input is noticed both earlier and with a higher intensity, such that a wave-like behavior is observed in the propagation of the excitation motion within the passenger's body.

Another subject of interest is the model's frequency response. The non-linear model has been linearized around its equilibrium and its frequency response has been investigated. To ascertain the accuracy of the linearization, the non-linear model was simulated for a small-amplitude harmonic input with a frequency sweep in the range of interest. It was determined that the linearized frequency response was virtually identical to the small-input, non-linear response. Frequency response plots were generated for various intersegmental velocity responses against the three heave, cruise, and pitch input velocities for a frequency range of 0.1-20 Hz. This range encompasses the entire range of vibration signals coming from a generic vehicle which is about 1-10 Hz [86]. It is noteworthy that this frequency response is identical to that of one between respective intersegmental displacements and input displacements, since velocity and displacement are proportional in the frequency domain.

$$\frac{V_{rel}(s)}{V_{in}(s)} = \frac{\mathcal{L}(\dot{q})}{\mathcal{L}(\dot{q}_{in})} = \frac{sq(s)}{sq_{in}(s)} = \frac{q(s)}{q_{in}(s)}$$

Eq. 40

Fig. 15 shows the non-dimensional vibration transmissibility for axial and shear motions subject to translational excitation velocities at three joint locations: the L5S1 and L4L5 lumbar discs at the bottom and the neck at the top of the model.

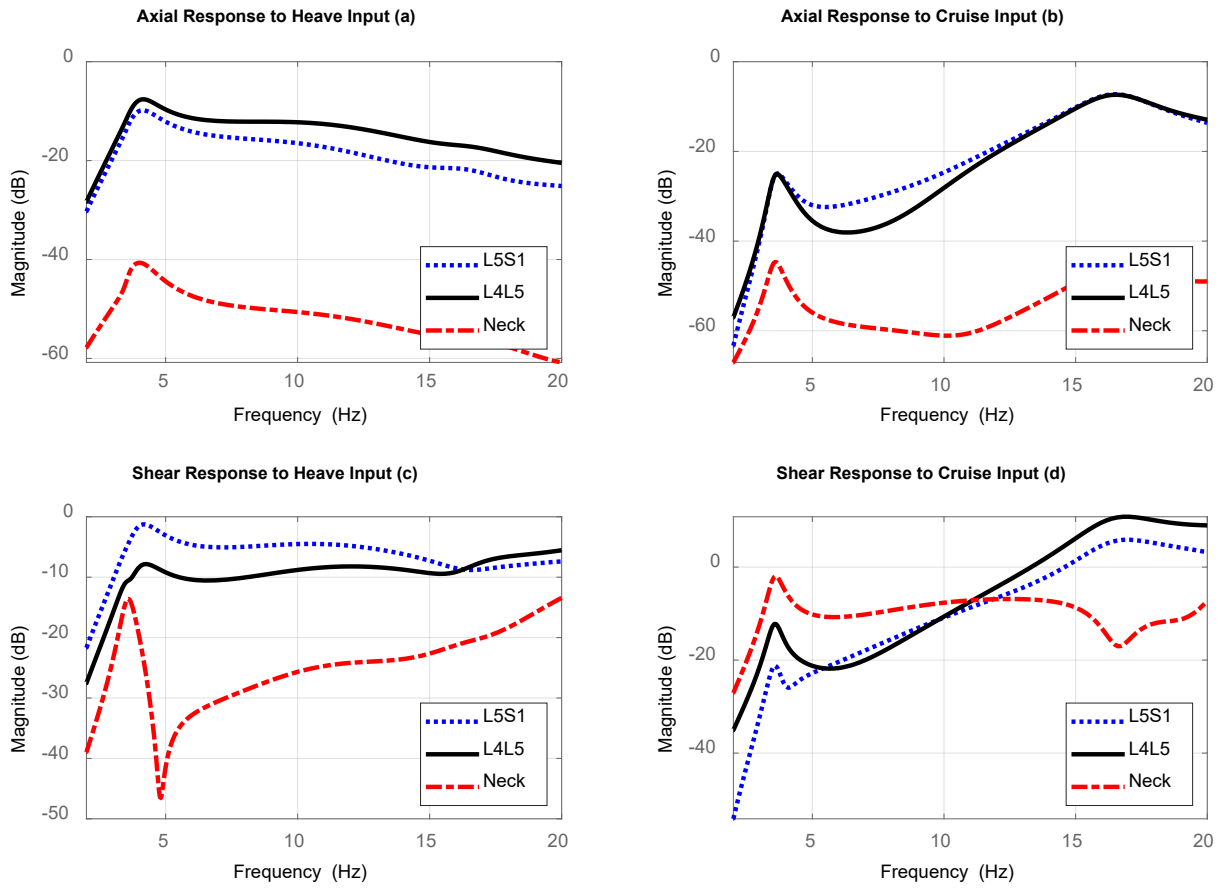

Figure 15. Translational Frequency Response for L5S1, L4L5, and Neck Joints

Fig. 15(a) shows that in response to vertical excitation, it is the L4L5 disc that experiences the highest vibration transmissibility for axial displacement, with L5S1 being a close second. However, for shear displacement due to heave input, it is L5S1 that sees the highest transmissibility, as evident in Fig.15(c). This corroborates with L5S1's inherent slanted orientation where its askew geometry induces a substantial shear force when exposed to vertical excitation[58]. Similarly, said slanted geometry causes the same cross-transmission effect as noted in Fig.15(b) where L5S1 experiences a higher transmissibility for axial displacement when subject to a horizontal excitation. Figures 15 (a) through (c) correspond well with how most chronic lower back pain is associated with the lower lumbar region[65], as the L4L5 and L5S1 discs have

developed the highest translational transmissibility. The smallest translational transmissibility is generally observed at the level of the neck. However, as depicted in Fig. 15(d), the neck experiences the highest transmissibility in shear vibrations when exposed to horizontal excitations within the vehicular frequency range of interest. This corresponds with how the majority of neck injuries are shear-related and are commonly associated with head-on collisions[87]. The non-dimensional rotational frequency response for a rotary excitation is brought in Fig. 16.

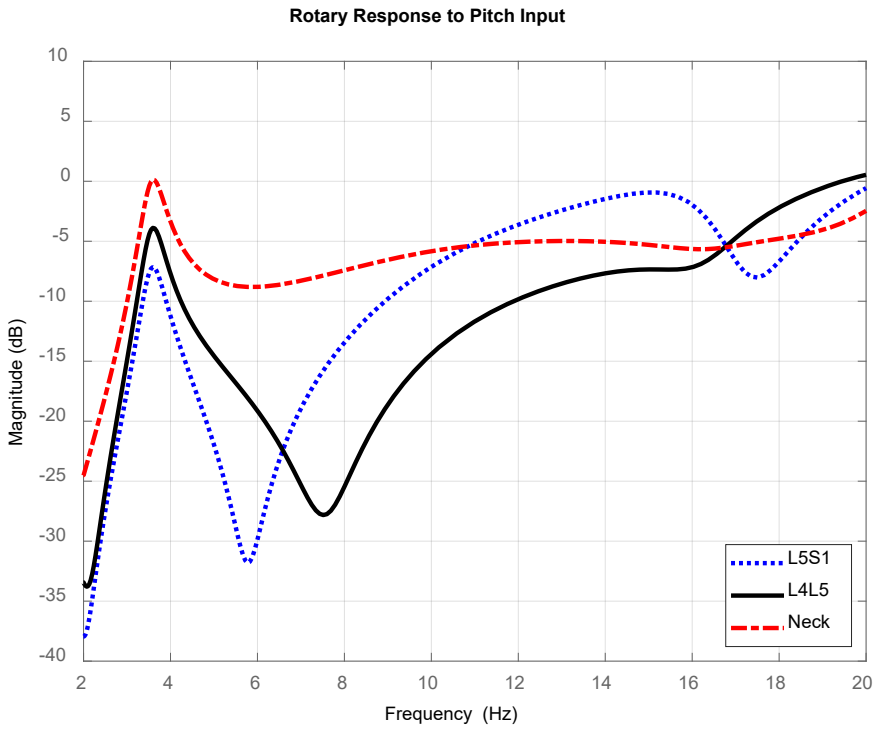

Figure 16. Rotary Frequency Response for the L5S1, L4L5, and Neck Joints

Fig. 16 shows that the neck has the highest rotational susceptibility to rotary excitation for the vehicular frequency range. Fig. 17 extensively investigates the non-dimensional translational transmissibility for translational excitations for the L4L5 disc.

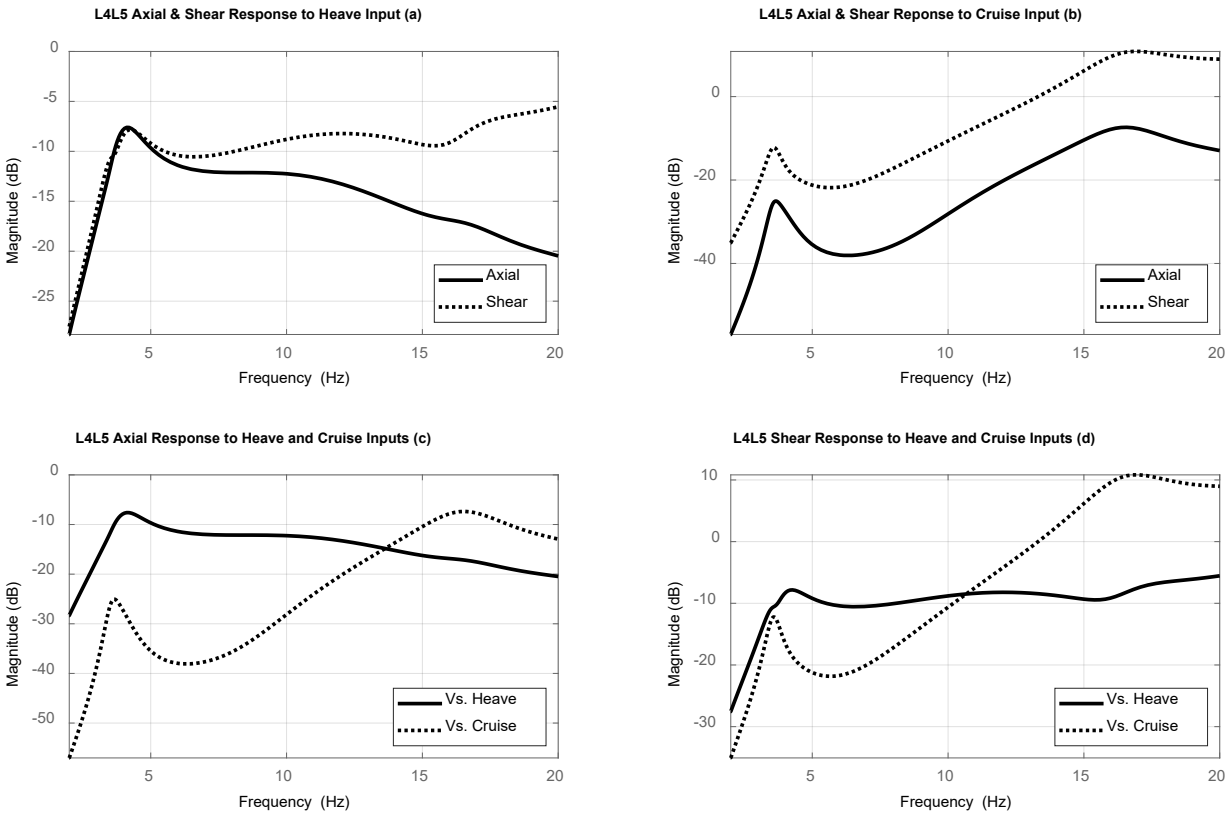

Figure 17. Translational Frequency Responses of the L4L5 Joint

Fig. 17 (a) and (b) show that in response to both translational inputs, the shear displacement has a higher transmissibility than that of axial displacement for all frequencies. Fig. 17(c) and (d) show that within the frequency range of interest, both translational responses are more susceptible to the heave input, despite the cruise input taking over at higher frequencies.

Another noteworthy remark that can be observed from all these frequency responses is that vibration transmission has a peak at around 4 Hz for all displacements and all excitations. This is also noticed in Pranesh's experiment and indicates a resonant natural frequency of about 4 Hz which falls within the vehicular frequency range.

The main limitation of this study is that its application is restricted to small-amplitude motions, as the force generating elements generally display nonlinear behaviors for large displacements.

However, the model's application can readily be extended to large-amplitude motions if proper stiffness and damping characteristics are introduced. Another reservation is that this model has excluded the arms and therefore cannot thoroughly account for the case of a driver with hands on the steering wheel, where the dynamic response is somewhat different according to [70]. A final remark is that this study has considered motions in the sagittal plane to be decoupled from other anatomical planes. While in general there is some degree of coupling amongst motions within said planes, Russell et al. have argued that sagittal motions are dominated by sagittal actions [88]. Hence, considering sagittal actions should suffice for adequately predicting sagittal motions.

2.10. Conclusion

An analytical, nonlinear biomechanical model of the upper body was developed for the purpose of studying the propagation of disturbance inputs from a generic vehicle to a seated passenger. The dynamic predications of the model are validated against experimental results within literature and it can replicate experimental data with sufficient accuracy and fidelity. The proposed model accounts for curved motion and allows for prediction of the all small-amplitude sagittal motions. This model employs much fewer degrees of freedom than similar finite element models and is therefore computationally lighter and provides additional geometric and analytical intuition into the upper body's internal dynamics. Upon simulation of frequency response, it was shown that within the vehicular frequency range of 1-10 Hz, the lower lumbar region, namely the L5S1 and L4L5 discs, experience the highest translational vibration transmissibility and the neck experiences the highest rotational vibration transmissibility. The model suggests that the maximum vibration transmissibility occurs at about 4 Hz, which could be the designated frequency for vibration mitigation and controller design. The model can be employed in ride-comfort studies and help define a quantitative ride comfort index, such that the most comfortable ride would be one that has

induced the least internal displacements. Also, the model has applications in any other study which might require an assessment of the internal dynamics of the upper body.

Level	Mass - m (kg)	Sagittal Mass Moment of Inertia - I_{yy} (×10^-4 kg.m^2)
Pelvis	8.1541	300
L5	2.1243	54.6
L4	2.0367	52.0
L3	1.9710	54.1
L2	1.8907	59.1
L1	1.8250	64.0
Thorax	16.0746	1250
Head	5.0662	293.4

Table 1. Inertial Parameters for the Passenger Model from [68] and [82]

Section	Initial k_a (kN/m)	Modified k_a (kN/m)	Initial k_s (kN/m)	Modified k_s (kN/m)
Pelvis-Seat	300	108	200	98
L5S1	510	184	45	22.1
L4L5	450	162	30	14.7
L3L4	525	189	30	14.7
L2L3	600	216	35	17.6
L1L2	620	223.2	40	19.6
T-L1	640	230.4	50	24.5
Neck	1250	450	30	14.7

Table 2. Translational Intervertebral Stiffness Values, initial guess from [81], modified to match [70]

Section	Initial b_a (Ns/m)	Modified b_a (Ns/m)	Initial b_s (Ns/m)	Modified b_s (Ns/m)
Pelvis-Seat	1200	938	1200	894
L5S1	1200	971	1200	337
L4L5	1200	581	1200	175
L3L4	1200	615	1200	172
L2L3	1200	646	1200	182
L1L2	1200	644	1200	191
T-L1	1200	1436	1200	468
Neck	1200	2181	1200	394

Table 3. Translational Intervertebral Damping Values, initial guess from [82], modified to match [70]

Section	k_r (Nm/rad)	b_r (Nms/rad)
Pelvis-Seat	700	1.2
L5S1	75	1.2
L4L5	80	1.2
L3L4	100	1.2
L2L3	120	1.2
L1L2	140	1.2
T-L1	160	1.2
Neck	400	1.2

Table 4. Rotational Intervertebral Stiffness and Damping Values, from [81] and [82]

Mass - m_{seat} (kg)	Cushion Stiffness - k_{seat} (kN/m)	Cushion Damping - b_{seat} (Ns/m)
13.6	80	1350

Table 5. Seat parameters, from [80]

Muscle	Young's Modulus - E_m (kPa)	Damping Ratio - ζ_m
Multifidus	91.34	0.58
Longissimus	62.85	0.58

Table 6. Muscle Material Properties, from [83] and [84]

	Thorax	L1	L2	L3	L4	L5
Initial Length – L0 (cm)	26.57	14.03	11.59	9.14	7.11	4.81
Cross Sectional Area - A_m (cm^2)	18.5	1.95	3.18	4.74	6.50	7.14

Table 7. Associated Muscles' Geometric Parameters, from [78] and [85]

		Thorax	L1	L2	L3	L4	L5
On Vertebra	α_v (deg)	171.2	89.8	89.6	101.9	108.1	105.2
	λ_v (mm)	178.3	68.8	66.8	72.6	68.6	63.3
On Pelvis	α_p (deg)	178.1	150.5	158.0	165.9	164.9	164.8
	λ_p (mm)	44.2	46.9	51.1	61.2	65.2	67.3

Table 8. Geometric Parameters for Muscle Attachment Points on both Vertebra and Pelvis[76]

	Distance to base - d (mm)	x-Distance to CG - D_x (mm)	z-Distance to CG - D_z (mm)
Lumbar Contact Point	212.5	69.9	19.3
Thorax Contact Point	438.9	64.8	66.8

Table 9. Geometric Parameters for Seat Backrest Contact Points[76]

Level	Head-Thorax	L1	L2	L3	L4	L5	Pelvis-L5
Half-Thickness (mm)	121.4	13.8	14.5	14.6	15.1	13.9	37.5

Table 10. Tangential Half-Thickness Dimensions for Velocity Transfer[76]

	Pelvis-Seat (tangential)	Pelvis-Seat (normal)	Thorax-L1 (tangential)	Thorax-L1 (normal)	Thorax-Head (tangential)	Thorax-Head (normal)
Distance (mm)	-89.8	65.3	-164.9	67.4	265.1	-19.6

Table 11. Distance from CG to compliance interface[76]

	Head	Thorax	L1	L2	L3	L4	L5	Pelvis
Initial Angle θ_0 (deg)	75.6	104.0	65.9	71.3	83.9	98.8	107.6	135.0
Initial Position x (mm)	-55.9	-10.7	-45.4	-58.4	-63.8	-61.4	-50.5	-17.3
Initial Position z (mm)	767.7	505.7	308.4	271.0	231.8	192.0	155.8	109.6

Table 12. Geometric Initial Conditions with Seat Base at the Coordinate Origin[76]

3. The Vehicle Model

The vehicle model employed in this study is a full-car model which consists of a vehicle body (sprung mass) that has all 6 rigid-body spatial degrees of freedom and is suspended on top of 4 wheels (unsprung mass) that have an individual vertical degree of freedom with respect to the vehicle body and can rotate around their individual axes. The front wheels can be steered. A schematic of the vehicle model is shown in Fig. 18.

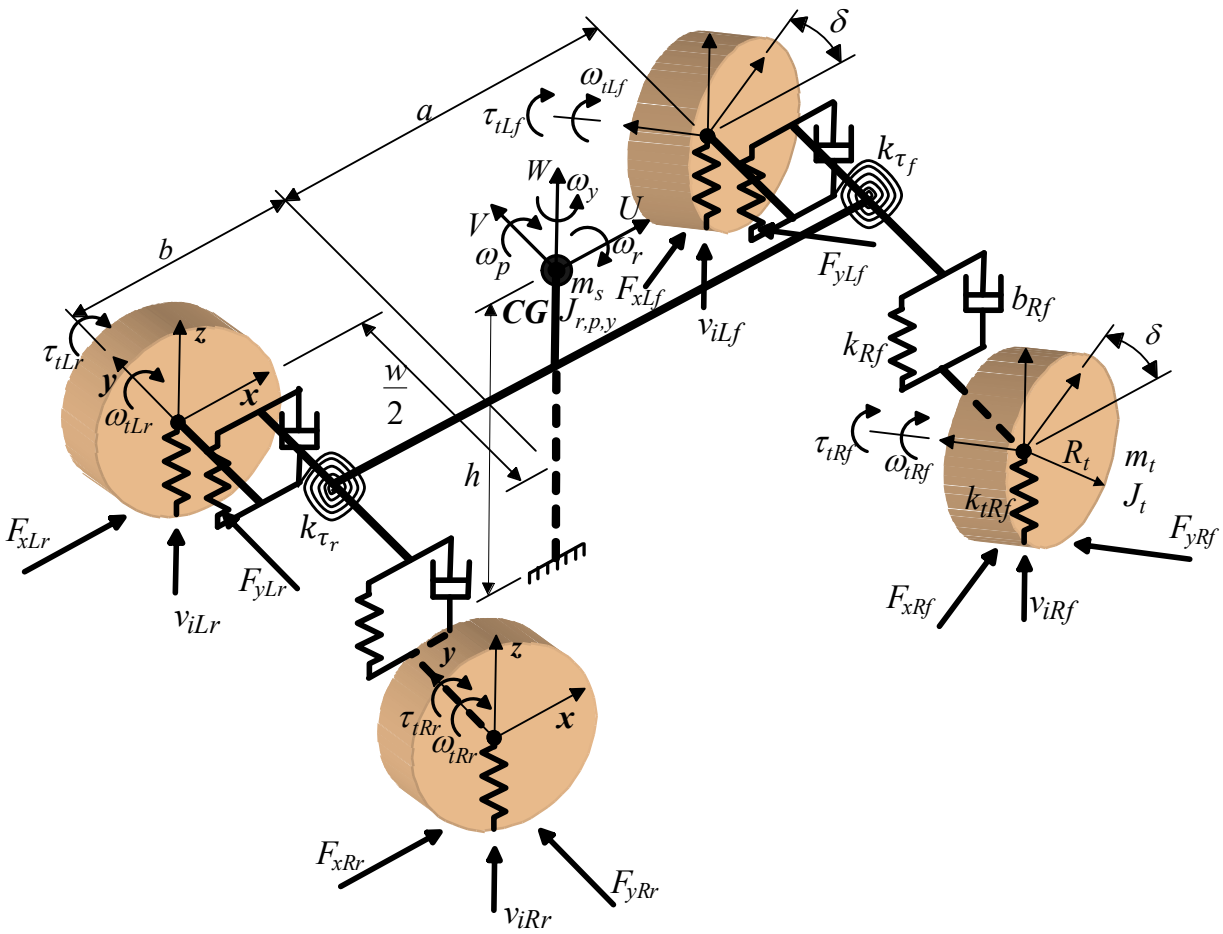

Figure 18 Schematic of the vehicle model

The coordinate origin is at the vehicle body's center of gravity designated with **CG**. Body-fixed coordinates are used where $\boldsymbol{x}$, $\boldsymbol{y}$, $\boldsymbol{z}$ axes are aligned with the vehicle's longitudinal, lateral, and

vertical directions, respectively, with positive $\boldsymbol{x}$ towards the front, positive $\boldsymbol{y}$ to the left, and positive $\boldsymbol{z}$ upwards. Like any rigid body in three-dimensional space, the vehicle body has 6 degrees of freedom including three translations and three rotations. The translational degrees of freedom are designated with U, V, and W that respectively denote longitudinal, lateral, and vertical velocities along body-fixed $\boldsymbol{x}$, $\boldsymbol{y}$, $\boldsymbol{z}$ axes that pass through the center of gravity. The vehicle body can also rotate around each axis. The rotational degrees of freedom are designated with ω_r, ω_p, ω_y that respectively denote roll, pitch, and yaw angular velocities around the $\boldsymbol{x}$, $\boldsymbol{y}$, $\boldsymbol{z}$ axes.

The center of gravity for the vehicle body is designated with **CG**. The vehicle body has mass m_s and moments of inertia J_r, J_p, J_y which indicate rotational moments of inertia for roll, pitch, and yaw motions, respectively. The center of gravity has height h from the inertial ground and is at distance a and b from the front and rear axles, respectively. The vehicle track width is the distance between the centerline of two wheels on the same axle and is denoted by w with the **CG** at the middle.

There are anti-roll bars represented with torsional springs k_{τ_f} and k_{τ_r} at the front and at the rear, respectively. The wheels each have mass m_t and moment of inertia J_t around their axes. The wheel angular velocities are denoted by ω_t. Lateral forces F_y and longitudinal forces F_x are applied to the vehicle at each corner through the force-generation mechanism of the tires. Vehicle suspension parameters are denoted by k and b which represent the suspension stiffness and damping, respectively. Tires are modeled as springs with stiffness k_t. The inputs to the model include the front steering angle δ, the road input velocity v_i at each corner, and the torque τ_t on each wheel.

For the parameters and variables associated with each corner, the subscripts L and R indicate left and right, and subscripts f and r denote front and rear, for example b_{Rf} indicates the suspension

damping coefficient at the front right corner, and $\omega_{t_{Lr}}$ denotes the angular velocity of the left rear wheel.

To develop the equations of motion, the forces applied to the sprung and unsprung masses should be identified and calculated. These forces are either vertical (along the $\boldsymbol{z}$ axis) or horizontal (within the $\boldsymbol{xy}$ plane). Vertical forces are applied to the sprung mass through the suspension units, and horizontal forces are generated by the tires. Therefore, to obtain the required forces it is necessary to have suspension and tire models.

3.1. Tire Forces

Tire forces include longitudinal F_x and lateral F_y forces that are applied to the vehicle from the inertial ground due to distortion of the tires. Empirical models have been developed that explain how tires generate forces [89]. In particular, two geometric slip quantities being the fore-aft slip and the side slip angle are the primary contributors to force generation. Fig. 19 shows a schematic of a tire and its velocity components.

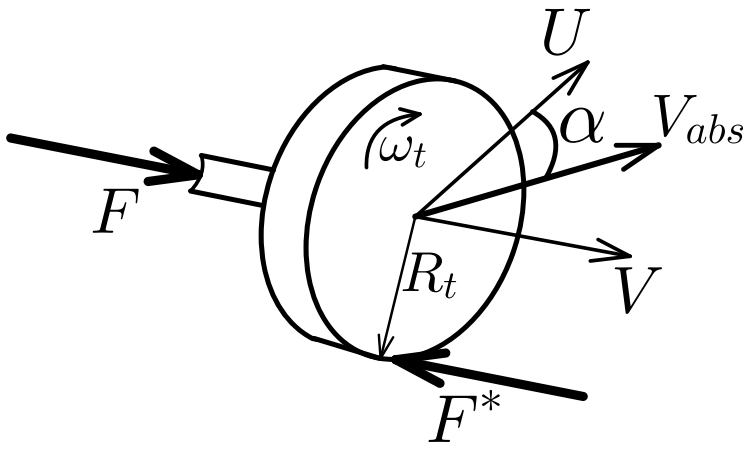

Figure 19 Schematic of a tire and its velocity components

The fore-aft slip, also known as the longitudinal slip, is a measure of the tire's deviation from pure rolling motion and is defined as follows:

$$s = \frac{R_t\omega_t - U}{max\{|R_t\omega_t|, U\}}$$

Eq. 41

Where R_t is the wheel's radius, ω_t is its angular velocity, and U is the longitudinal velocity component of the wheel center. For the case of pure rolling, the fore-aft slip would be zero, but since the tire is not a rigid body there is always some slip. The denominator of Eq. 41 would be $R_t\omega_t$ for acceleration and U for braking.

The second slip quantity is the side slip angle which enables the generation of lateral force and is calculated as:

$$\alpha = (-)\tan^{-1}\frac{V}{U}$$

Eq. 42

As noticed in Fig. 19, a force F is applied to the tire and gives it a lateral velocity component V, this causes the tire's longitudinal velocity component U to make an angle α with the tire's absolute velocity vector V_{abs}, and this creates a lateral contact force F^*. This F^* is the force required in horizontal dynamics analysis and it is generated due to the existence of the side slip angle α[89]. The negative sign is employed as a convention such that a positive α causes a positive F^*.

There are quite a few theories that associate said slip quantities to the horizontal forces generated by the tires, including the linear tire model[86], the Dugoff tire model[90], and Pacejka's Magic Formula tire model[91] which become more and more complicated in the same order. The linear

tire model can adequately predict the force generation for small slip angles. However, the linear tire model does not saturate, i.e. it suggests that tires can generate unlimited forces as long as sufficient slip or side slip is provided. However, we know that tire forces generation saturate at a certain threshold beyond which the tire slides[89]. The Dugoff tire model has addressed this limitation and allows for nonlinear force generation and saturation. The Dugoff tire model can reasonably predict relatively harsh driving maneuvers and is employed as the required tire model to associate the generated forces with the slip quantities in this research.

3.1.1. The Dugoff Tire Model

The Dugoff tire model enables nonlinear force generation and associates the horizontal forces generated by the tire to the fore-aft slip, side slip angle, and normal force. Fig. 20 is a schematic of the forces at the contact patch of a typical vehicle tire.

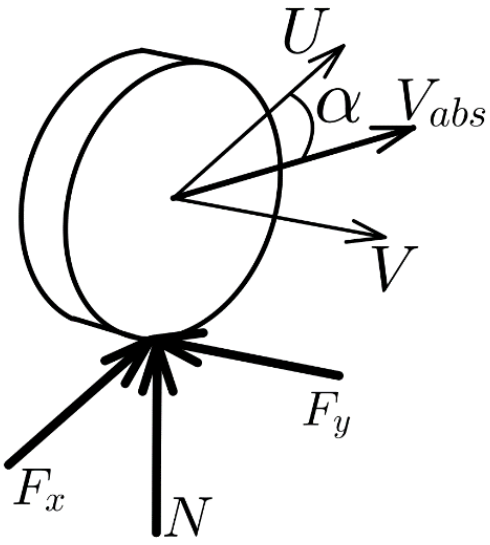

Figure 20 Schematic of tire forces and velocity components

The Dugoff tire model calculates the horizontal forces, longitudinal F_x and lateral F_y, as follows:

$$F_{x_{temp}} = \frac{C_x s}{1 - |s|} \quad ; \quad F_{y_{temp}} = \frac{C_y \tan \alpha}{1 - |s|}$$

Eq. 43

Where s is the fore-aft slip, α is the side slip angle, and C_x and C_y are tire coefficients obtained from experiment. Eq. 43 calculates the tire forces assuming that the tire's force-generation capability has not been saturated. In order to determine whether or not the tire is indeed saturated we would subsequently calculate:

$$\lambda = \frac{\mu N}{2\sqrt{{F_{x_{temp}}}^2 + {F_{y_{temp}}}^2}}$$

Eq. 44

Where μ is the coefficient of friction between the tire and the inertial ground at the contact patch, N is the normal force applied to the tire from the inertial ground, and λ is an index of tire saturation. Now the actual tire forces, for both directions, become:

$$F_{x,y} = F_{x,y_{temp}} \qquad if\ \lambda \geq 1$$

$$F_{x,y} = 2\lambda\left(1 - \frac{\lambda}{2}\right) F_{x,y_{temp}} \qquad if\ \lambda < 1$$

Eq. 45

3.2. Wheel Torque and Traction

The longitudinal F_x forces depend on the fore-aft slip, and that in turn depends on the angular velocity of the wheel which is a function of the torque applied to the wheel. Fig. 21 shows a schematic of a wheel with applied torque and the longitudinal force.

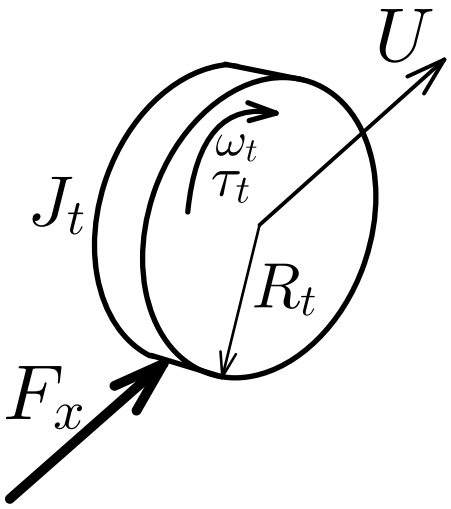

Figure 21 Schematic of a wheel with tractive torque

The present vehicle model does not include the powertrain and it is assumed that each wheel has an independent torque τ_t applied to it which rotates the wheel.

3.3.Road Input

The input signals v_i come from random number generation algorithms to simulate a vehicle going over a standard random road. The road profile is different for the left and right wheels to enable roll excitation. Furthermore, the road input to the rear tires is a delayed version of the one at the front tires, as the longitudinal velocity of the car U is usually much larger than its lateral velocity V, which causes the rear tires to basically traverse a delayed version of the road input at the front, even if the vehicle is being steered. Fig. 22 shows a schematic of a vehicle over a random road.

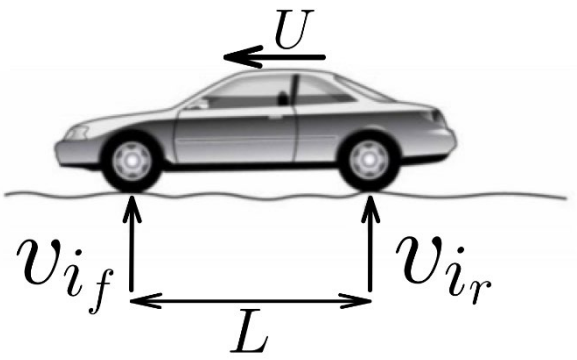

Figure 22 Schematic of a vehicle over a random road

As can be seen in Fig. 22, the rear axle will traverse the same road that the front axle has, but only at a time equal to L/U later, where L is the vehicle's wheelbase and is the sum of parameters a and b introduced in Fig. 18.

$$v_{i_r}(t) = v_{i_f}(t - \frac{L}{U})$$

Eq. 46

3.4.Kinematics and Geometry

The equations of motion are derived using bond graphs [92]. Bond Graphs are a modeling technique developed by Dr. Henry Paynter (1958)[93] which enable modeling dynamic systems within different energy domains (mechanical, electrical, hydraulic, etc) that track energy from the inputs to the outputs of a dynamic system. They are quite useful in modeling multibody mechanical dynamics, such as a vehicle that consists of various sub-systems (sprung mass, suspension, wheel traction, etc). Perhaps the most useful feature of bond graph modeling is that causality is straight forward to evaluate such that it is known apriori if subsystem models will fit together such that a computational overall model will result. Their advantage in modeling multibody systems is that the bond graph segment for each module attaches to the others and one can proceed to derive the

equations of motion in one continuous step. In order to develop the bond graph for the vehicle model at hand, the different bond graph segments for each module need to be attached together through the kinematic relationships between said modules and their layout.

3.5.Unsprung Mass and Suspension

The vertical forces are the response of the vehicle's suspension system to the road input and in order to find the vertical forces we need a model for the vehicle suspension. The suspension energy elements (springs and dampers) are assumed to have linear constitutive behaviors. Fig. 23 brings a schematic of a corner suspension unit detached from the sprung mass.

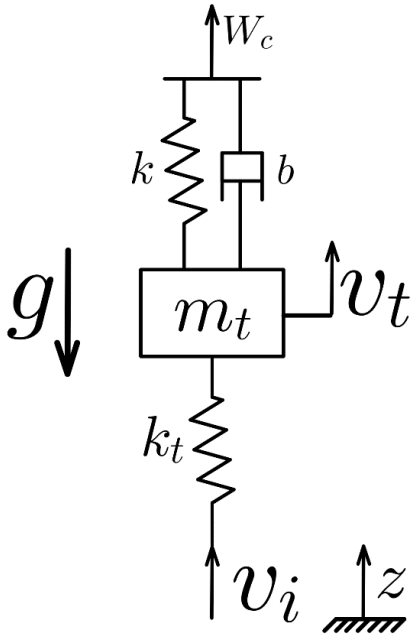

Figure 23 Schematic of a corner suspension unit, detached from the sprung mass

Here v_t is the heave velocity of the unsprung mass at each corner and W_c is the heave velocity of the sprung mass at the location of the individual corner. This point belongs to the sprung mass and

its velocity W_c will be calculated using a velocity transfer from the center of gravity. The c subscript indicates the quantity of interest is being expressed at one of the four corners.

3.6.Anti-Roll Bar

An anti-roll bar is a device that allows modification of a vehicle's roll stiffness while not effecting its vertical stiffness. Anti-roll bars are at the front and rear of virtually all vehicles and are used to effect the oversteer/understeer behavior of the vehicle. Fig. 24 shows a schematic of the anti-roll bar at the front. The torsional spring creates a torque which exerts equal and opposite forces on the sprung and corner unsprung masses through a moment arm of $\frac{w}{2}$. The difference between the unsprung mass heave velocity v_t and the sprung mass heave velocity W_c at each corner twists a half-shaft with length l_a (not shown in Fig. 18). The difference between these twists on either side is resisted by the anti-roll bar which is modeled as a torsional spring.

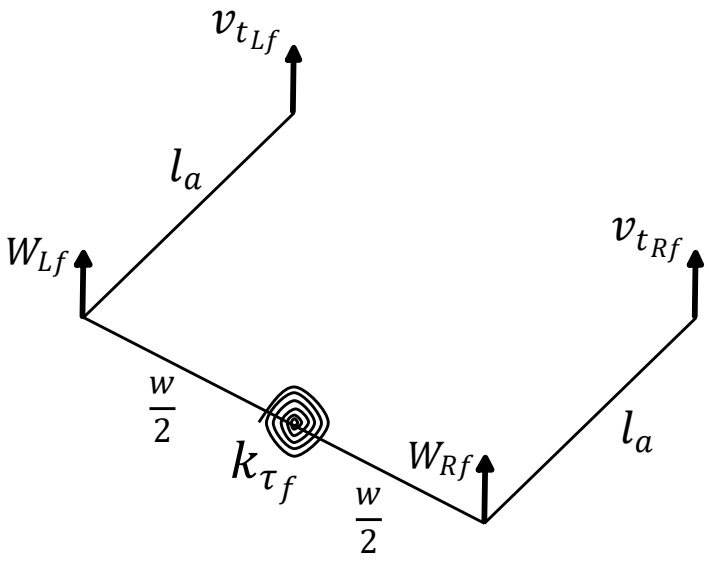

Figure 24 Schematic of the front anti-roll bar

3.7.Sprung Mass

To develop the kinematics of the sprung mass, it can be decoupled from the unsprung masses as though they were detached. Fig. 25 shows a schematic of the sprung mass' geometry and the important velocities and dimensions that play a part in deriving the equations of motion.

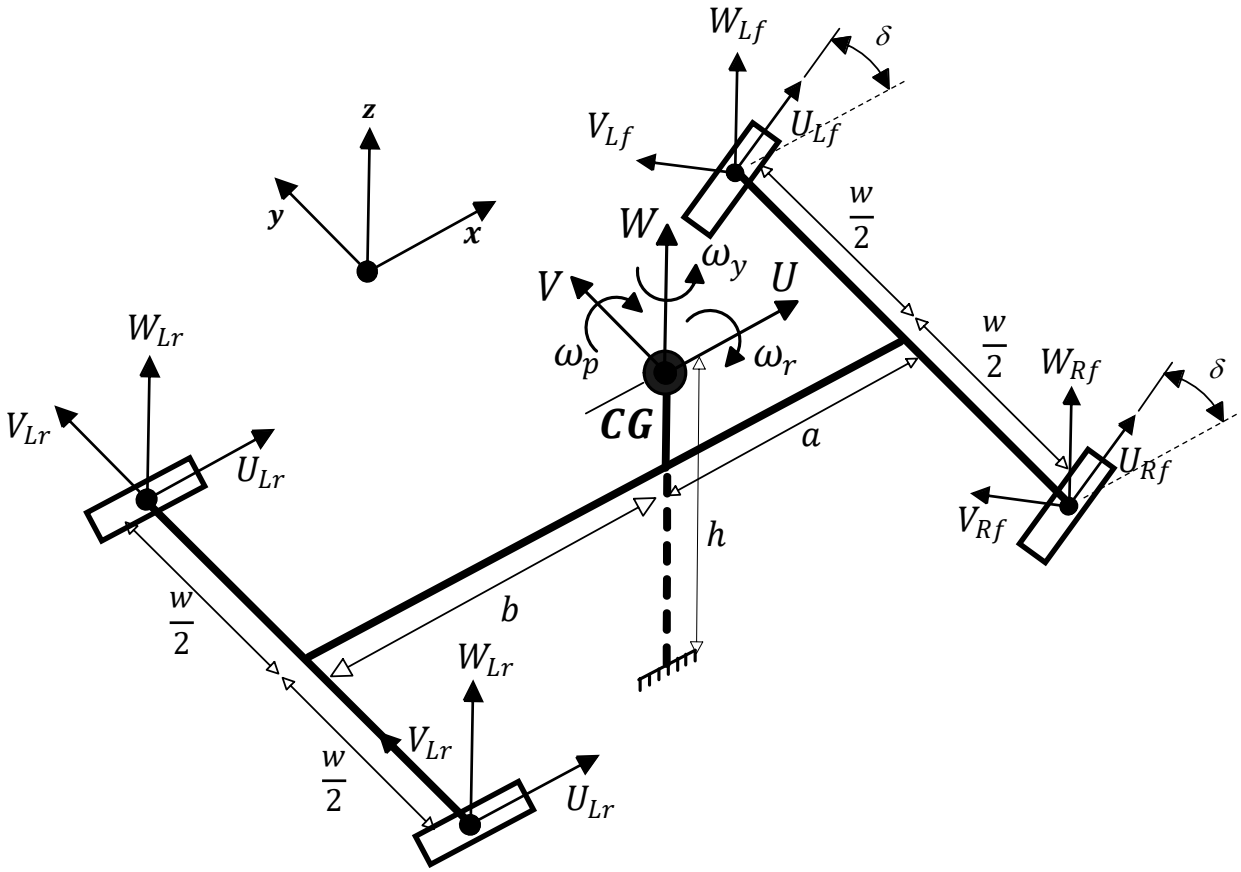

Figure 25 Schematic of the sprung mass and body-fixed velocities

It must be noted that body-fixed coordinates are used and the reference axes rotate with the vehicle body. In a similar diagram, Fig. 26 brings a free-body diagram of the sprung mass as if decoupled from the unsprung masses and shows the forces acting on it.

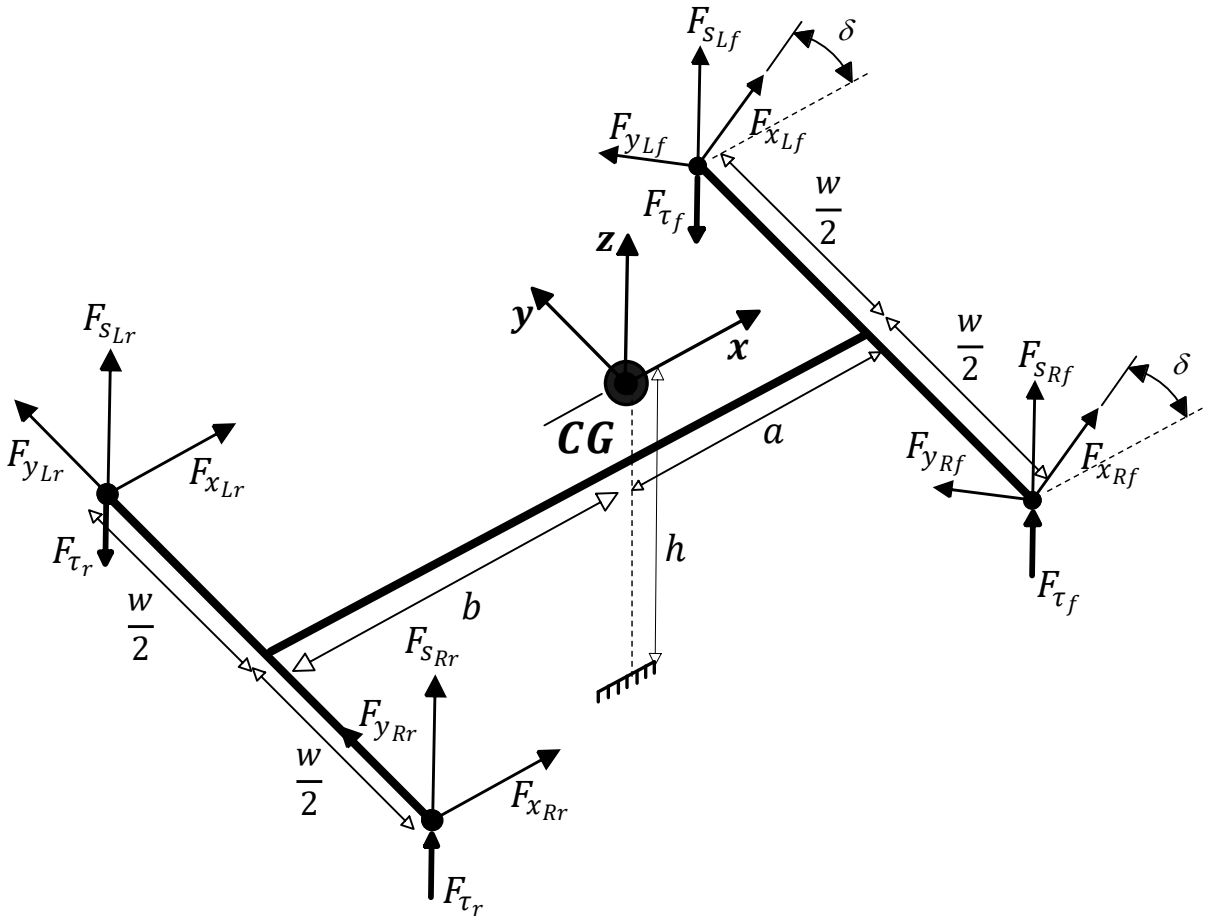

Figure 26 Free body diagram of the sprung mass

The horizontal forces F_x and F_y are applied to the vehicle body at each corner's wheel center, as it is assumed that the same horizontal force would be experienced at the wheel center as it is at the contact patch. The vertical F_s forces are applied to the sprung mass via the suspensions and their reaction is applied to the unsprung masses. The vertical anti-roll bar forces F_τ are applied equally and in opposite directions on either side of the sprung mass and therefore have a pure-rolling effect and do not contribute to the sprung mass' heave and pitch motions. However, their reaction is applied to the unsprung masses and affects the vertical motion of the unsprung mass.

To further derive the dynamics of the sprung mass, one must note that the wheel centers are located at a height R_t from the inertial ground as shown in Fig. 19 and the center of gravity of the sprung mass is located at height h.

To find the horizontal forces using the Dugoff tire model, the wheel center velocities need to be calculated. The rear wheels' velocities are oriented along the main body's coordinate axes but the front wheel velocities are oriented along axes of their own due to the front steering angle that rotates the front tires with respect to the vehicle body in the yaw direction. Therefore, the longitudinal and lateral components of wheel center velocities have to be calculated along each wheel's instantaneous axes.

The wheel centers are treated as points on the vehicle body and a rigid-body velocity transfer between the center of gravity and the wheel center yields the wheel centers' horizontal velocity components. For the rear axle, these velocities would readily generate the required horizontal forces, for the front axle, however, the obtained velocities need to be transferred one more time to be along the steered wheel's directions. The velocity transfer from the vehicle body's center of gravity to the wheel center would be performed as such:

$$\vec{V}_{w.c.} = \vec{V}_{CG} + \vec{\omega} \times \vec{r}_{w.c.}$$

Eq. 47

Here the w.c. subscript indicates wheel center, and the $\vec{r}_{w.c.}$ vector is the displacement vector connecting the center of gravity to the individual wheel center. V_{CG} and ω represent the translational and rotational velocity vectors of the body at the center of gravity.

$$\vec{V}_{CG} = \begin{Bmatrix} U \\ V \\ W \end{Bmatrix} \quad ; \quad \vec{\omega} = \begin{Bmatrix} \omega_r \\ \omega_p \\ \omega_y \end{Bmatrix}$$

Eq. 48

Also, the individual $r_{w.c.}$ displacement vectors are given as:

$$\vec{r}_{Rf} = \begin{Bmatrix} a \\ -\frac{w}{2} \\ -(h - R_t) \end{Bmatrix} ; \ \vec{r}_{Lf} = \begin{Bmatrix} a \\ \frac{w}{2} \\ -(h - R_t) \end{Bmatrix} ; \ \vec{r}_{Lr} = \begin{Bmatrix} -b \\ \frac{w}{2} \\ -(h - R_t) \end{Bmatrix} ; \ \vec{r}_{Rr} = \begin{Bmatrix} -b \\ -\frac{w}{2} \\ -(h - R_t) \end{Bmatrix}$$

Eq. 49

Plugging the information from Eq. 48 and Eq. 49 into Eq. 47, the velocity components of the wheel centers would be calculated accordingly. The horizontal velocity components U_c, V_c lend themselves to horizontal force generation through the Dugoff tire model and the vertical components W_c determine the vertical F_s forces applied to the sprung mass from the corner suspension units.

$$\begin{Bmatrix} \bar{U}_{Rf} \\ \bar{V}_{Rf} \\ W_{Rf} \end{Bmatrix} = \begin{Bmatrix} U - (h - R_t)\omega_p + \frac{w}{2}\omega_y \\ V + a\omega_y + (h - R_t)\omega_r \\ W - \frac{w}{2}\omega_r - a\omega_p \end{Bmatrix}$$

$$\begin{Bmatrix} \bar{U}_{Lf} \\ \bar{V}_{Lf} \\ W_{Lf} \end{Bmatrix} = \begin{Bmatrix} U - (h - R_t)\omega_p - \frac{w}{2}\omega_y \\ V + a\omega_y + (h - R_t)\omega_r \\ W + \frac{w}{2}\omega_r - a\omega_p \end{Bmatrix}$$

$$\begin{Bmatrix} U_{Lr} \\ V_{Lr} \\ W_{Lr} \end{Bmatrix} = \begin{Bmatrix} U - (h - R_t)\omega_p - \frac{w}{2}\omega_y \\ V - b\omega_y + (h - R_t)\omega_r \\ W + \frac{w}{2}\omega_r + b\omega_p \end{Bmatrix}$$

$$\begin{Bmatrix} U_{Rr} \\ V_{Rr} \\ W_{Rr} \end{Bmatrix} = \begin{Bmatrix} U - (h - R_t)\omega_p + \frac{w}{2}\omega_y \\ V - b\omega_y + (h - R_t)\omega_r \\ W - \frac{w}{2}\omega_r + b\omega_p \end{Bmatrix}$$

Eq. 50

It is noteworthy that with the given velocity transfer, the horizontal velocity components would be calculated at each corner along the directions of the central axes and therefore the calculated front wheels' horizontal velocities are denoted with a bar symbol $\overline{U}, \overline{V}$. To find the horizontal forces at the front axle, the wheel center velocity components need to be expressed along the wheels' steered axes. The steered velocity components at the front are calculated according to Fig. 25:

$$U_{Rf} = \overline{U}_{Rf}\cos\delta + \overline{V}_{Rf}\sin\delta \;\; ; \;\; U_{Lf} = \overline{U}_{Lf}\cos\delta + \overline{V}_{Lf}\sin\delta$$

$$V_{Rf} = -\overline{U}_{Rf}\sin\delta + \overline{V}_{Rf}\cos\delta \;\; ; \;\; V_{Lf} = -\overline{U}_{Lf}\sin\delta + \overline{V}_{Lf}\cos\delta$$

Eq. 51

With the kinematic relationships for the sprung mass and the unsprung masses developed, we can proceed to draw the system's bond graph.

The bond graph for the vehicle model is given in Fig. 27, excluding the anti-roll bar to allow for better clarity. As is evident in Fig. 27, the bond graph is causal, i.e. every inertia and compliance element is in integral causality and therefore the equations of motion can readily be derived from the bond graph.

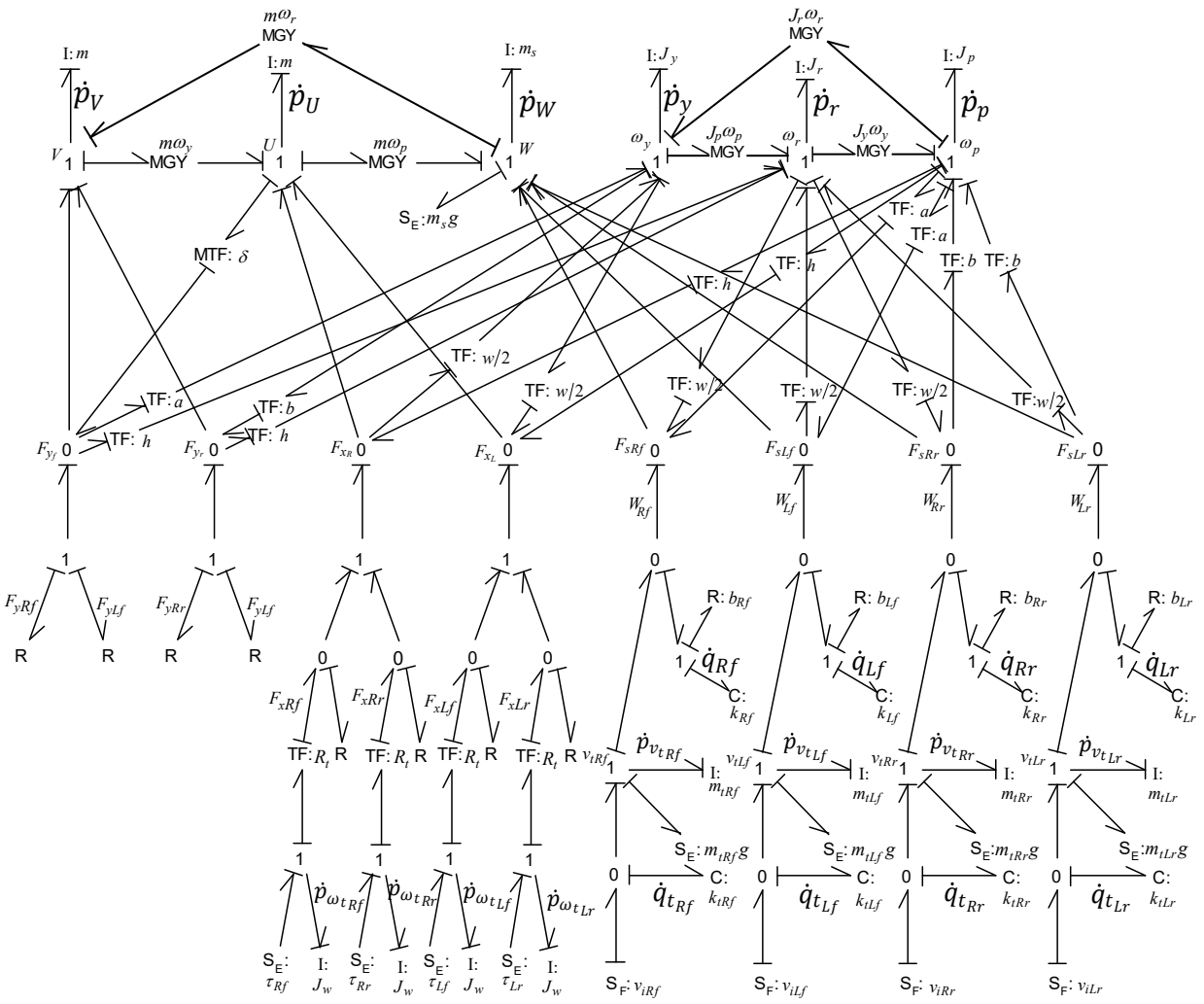

Figure 27 Bond graph of the vehicle model, excluding the anti-roll bar

The bond graph segment for the anti-roll bar is given in Fig. 28 with the unsprung mass velocity v_t and sprung mass corner velocity W_c brought from Fig. 27 with the same causality, which indicates that the bond graph segments can indeed be integrated properly.

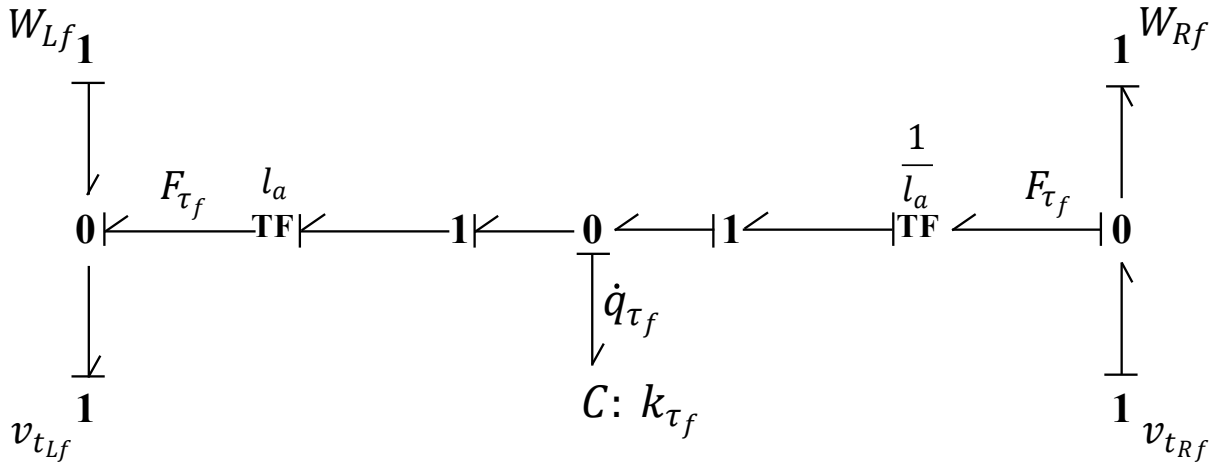

Figure 28 Bond graph segment for the front anti-roll bar

Now with all the velocities across force generating elements and velocities associated with all the inertias having been established, the equations of motion for the vehicle model can be derived from the given bond graphs in Fig. 27 and Fig. 28. Bond graphs yield the equations of motion as a set of first-order differential equations in a state-space where the state variables are the momenta of the inertial elements and the displacements across the springs which are denoted with p and q variables, respectively. The momentum variables are proportional to their corresponding velocity and could be expressed in velocity terms as well. The structure of the equations of motion is such that the time derivative of each state is a function of other states and the inputs only. The sign convention for the relative velocities across the springs is that displacement is considered positive in compression. In the following derived equations, the subscript c indicates that the equation is being developed for one of the four corners.

The anti-roll bar equations for the front and rear are as follows:

$$\dot{q}_{\tau_f} = \frac{v_{t_{Rf}} - W_{Rf}}{l_a} - \frac{v_{t_{Lf}} - W_{Lf}}{l_a} \quad ; \quad \dot{q}_{\tau_r} = \frac{v_{t_{Rr}} - W_{Rr}}{l_a} - \frac{v_{t_{Lr}} - W_{Lr}}{l_a}$$

Eq. 52

$$F_{\tau_f} = \frac{k_{\tau_f} q_{\tau_f}}{l_a} \quad ; \quad F_{\tau_r} = \frac{k_{\tau_r} q_{\tau_r}}{l_a}$$

Eq. 53

The unsprung mass and suspension equations are as follows:

$$\dot{q}_{t_c} = v_{i_c} - v_{t_c}$$

Eq. 54

$$\dot{q}_{s_c} = v_{t_c} - W_c$$

Eq. 55

$$\dot{p}_{v_{t_c}} = m_t \dot{v}_{t_c} = -m_t g + N_c - F_{s_c} \pm F_{\tau_c} \; ; \; N_c = k_t q_{t_c} \; if \; q_{t_c} \geq 0 \; ; \; F_{s_c} = k_c q_{s_c} + b_c (v_{t_c} - W_c)$$

Eq. 56

Where q_{t_c} is the displacement across the tire spring, q_{s_c} is the displacement across the suspension spring, and $p_{v_{t_c}}$ is the vertical momentum of the unsprung mass, all for the individual corner c. Also F_{s_c} is that corner's suspension force which will be applied to both the sprung mass and the unsprung mass in action and reaction. Furthermore, F_{τ_c} is the anti-roll bar force at the corner of interest which in the employed sign convention is negative for the right wheels and positive for the left wheels, as they're the reactions of the F_τ forces specified in Fig. 26. It is also noteworthy that the normal force N_c required to calculate the horizontal forces from the Dugoff tire model comes from suspension analysis. Tires can only be in compression, as the inertial ground can only push on the vehicle. Therefore, a normal force will be generated in the tires only if they are compressed, which is indicated in Eq. 56.

The equation for wheel traction in each corner is as follows:

$$\dot{p}_{\omega_{t_c}} = J_t \dot{\omega}_{t_c} = \tau_{t_c} - R_t F_{x_c}$$

Eq. 57

Where $p_{\omega_{t_c}}$ is the angular momentum of the rotating wheel at each corner.

Before one can derive the equations of motion for the sprung mass, it is necessary to point out that due to the use of body-fixed coordinates, the reference frame rotates with the body and therefore cross product terms show up in all momentum equations, both angular and translational. These non-linear terms are represented by modulated gyrators in the bond graph.

It is noteworthy to mention that for the translational equations, the sprung mass and the unsprung masses have been decoupled for the heave (vertical) degree of freedom and the heave equation is decoupled for the sprung mass and the unsprung masses. However, since the attachments of the wheels to the vehicle body are assumed to be infinitely stiff in the longitudinal and lateral directions, the sprung mass and the unsprung masses have no relative motion with respect to one another in the longitudinal and lateral directions and therefore the equations of motion for these translational degrees of freedom are written for the entire vehicle mass.

$$M = m_{total} = m_s + 4m_t$$

Eq. 58

The forces that affect the sprung mass dynamics are designated in the bond graph in Fig. 27. Each force is a function of the state variables and the inputs.

The translational equations of motion for the sprung mass are given as follows:

$$\dot{p}_U = M\dot{U} = -MW\omega_p + MV\omega_y + \left(F_{x_{Rf}} + F_{x_{Lf}}\right)\cos\delta - \left(F_{y_{Rf}} + F_{y_{Lf}}\right)\sin\delta + F_{x_{Rr}} + F_{x_{Lr}}$$

Eq. 59

$$\dot{p}_V = \dot{MV} = -MU\omega_y + MW\omega_r + \left(F_{y_{Rf}} + F_{y_{Lf}}\right)\cos\delta + \left(F_{x_{Rf}} + F_{x_{Lf}}\right)\sin\delta + F_{y_{Rr}} + F_{y_{Lr}}$$

Eq. 60

$$\dot{p}_W = m_s\dot{W} = -m_sV\omega_r + m_sU\omega_p - m_sg + F_{s_{Rf}} + F_{s_{Lf}} + F_{s_{Rr}} + F_{s_{Lr}}$$

Eq. 61

Where p_U, p_V, p_W are the longitudinal, lateral, and vertical translational momenta of the sprung mass, respectively.

The Rotational momentum equations of motion for the sprung mass are:

$$\dot{p}_r = J_r\dot{\omega}_r = J_p\omega_p\omega_y - J_y\omega_y\omega_p + h\left(\left(F_{y_{Rf}} + F_{y_{Lf}}\right)\cos\delta + \left(F_{x_{Rf}} + F_{x_{Lf}}\right)\sin\delta + F_{y_{Rr}} + F_{y_{Lr}}\right)$$
$$+ \frac{w}{2}\left(-F_{s_{Rf}} + F_{s_{Lf}} - F_{s_{Rr}} + F_{s_{Lr}}\right) - 2w\left(F_{\tau_f} + F_{\tau_r}\right) + \left(\tau_{t_{Rf}} + \tau_{t_{Lf}}\right)\sin\delta$$

Eq. 62

$$\dot{p}_p = J_p\dot{\omega}_p = J_y\omega_y\omega_r - J_r\omega_r\omega_y + b\left(F_{s_{Rr}} + F_{s_{Lr}}\right) - a\left(F_{s_{Rf}} + F_{s_{Lf}}\right)$$
$$- \left(\tau_{t_{Rf}} + \tau_{t_{Lf}}\right)\cos\delta - \left(\tau_{t_{Rr}} + \tau_{t_{Lr}}\right)$$
$$+ h\left(\left(F_{y_{Rf}} + F_{y_{Lf}}\right)\sin\delta - \left(F_{x_{Rf}} + F_{x_{Lf}}\right)\cos\delta - \left(F_{x_{Rr}} + F_{x_{Lr}}\right)\right)$$

Eq. 63

$$\dot{p}_y = J_y\dot{\omega}_y = J_r\omega_r\omega_p - J_p\omega_p\omega_r + a\left(\left(F_{y_{Rf}} + F_{y_{Lf}}\right)cos\,\delta + \left(F_{x_{Rf}} + F_{x_{Lf}}\right)sin\,\delta\right)$$
$$- b\left(F_{y_{Rr}} + F_{y_{Lr}}\right)$$
$$+ \frac{w}{2}\left(\left(F_{x_{Rf}} - F_{x_{Lf}}\right)cos\,\delta + \left(F_{y_{Lf}} - F_{y_{Rf}}\right)sin\,\delta + \left(F_{x_{Rr}} - F_{x_{Lr}}\right)\right)$$

Eq. 64

Where p_r, p_p, p_y are the roll, pitch, and yaw angular momenta of the sprung mass.

It is noteworthy that the reaction of the wheel torques are applied to the sprung mass and contribute to the pitch and roll equations, as they act in the $\boldsymbol{xy}$ plane.

The given equations together govern the dynamics of the vehicle, and with appropriate parameters and initial conditions could replicate the dynamic behavior of a real vehicle.

3.8.Parameters

There are many parameters employed in this model which are necessary for analyzing the dynamics of the vehicle. The parameters are extracted for a full-sized sedan. Some parameters are directly extracted from the literature, whereas others are estimated according to other specifications. Table 1 gives a list of all vehicle parameters extracted from the literature.

Symbol	Meaning	Value	Units
g	Gravitational acceleration constant	9.81	$\frac{m}{s^2}$
M	Total vehicle mass	1372.97	kg
m_{ratio}	Sprung to unsprung mass ratio $m_{ratio} = \frac{m_s}{4m_t}$	6	-

L	Wheelbase Length	2.805	m
l_a	Anti-roll bar length on either side	0.4572	m
$\frac{a}{b}$	Ratio of distance from front axle to CG to the rear's	0.676	-
w	Track length	1.615	m
h	CG height	0.54	m
J_p	Pitch moment of inertia	3235	kgm^2
J_y	Yaw moment of inertia	3832	kgm^2
J_r	Roll moment of inertia	663	kgm^2
R	Wheel's radius	0.313	m
J_t	Wheel's moment of inertia	1.965	kgm^2
ν_{ride_f}	Front ride frequency	1.120485	Hz
ν_{ride_r}	Rear ride frequency	1.167136	Hz
$\nu_{W.H.}$	Wheel-hop frequency	10.5	Hz
$k_{\tau_{f_{total}}}$	Total roll stiffness at the front	1468.785	$N.m/deg$
$k_{\tau_{r_{total}}}$	Total roll stiffness at the rear	1089.494	$N.m/deg$
ζ_f	Front suspension damping ratio	0.42	-
ζ_r	Rear suspension damping ratio	0.47	-
μ	Coefficient of friction (dry asphalt)	0.75	-
C_{x_f}	Longitudinal front tire coefficient	166050	N
C_{y_f}	Lateral front tire coefficient	68000	N
C_{x_r}	Longitudinal rear tire coefficient	119350	N

C_{y_r}	Lateral rear tire coefficient	48000	N

Table 13 Vehicle parameters extracted from the literature

Some other parameters are not directly extracted from the literature, but are calculated according to those that have been. These include the sprung mass, the individual unsprung masses, and the stiffness and damping parameters for the suspension units and tires.

$$m_s = M\left(\frac{m_{ratio}}{1+m_{ratio}}\right) \quad ; \quad m_t = \frac{M-m_s}{4}$$

Eq. 65

To calculate the suspension stiffness parameters according to the inscribed ride frequency, the effective corner masses of the vehicle body need to be determined. They are obtained from a static pitch equilibrium equation where the effective mass would be proportional to the static normal force at each corner. Fig. 29 shows a schematic of a stationary vehicle in a gravity field.

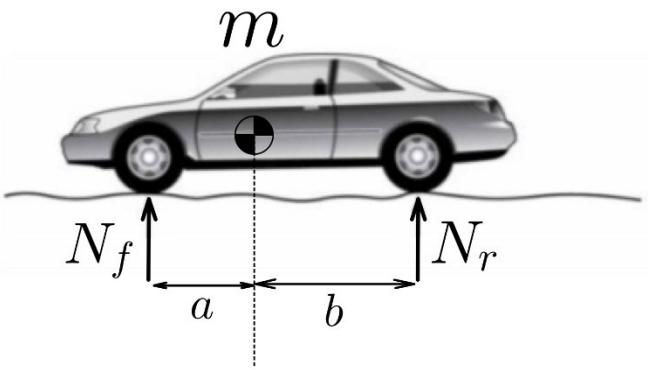

Figure 29 Vehicle schematic for mass distribution analysis

According to Fig. 29, the effective mass distribution for the front and rear axles would be:

$$\sum M_{static} = 0 \rightarrow N_f = \frac{b}{a+b}mg \quad ; \quad N_r = \frac{a}{a+b}mg$$

$$m_{s_f} = \frac{1}{2}\frac{b}{a+b}m_s \quad ; \quad m_{s_r} = \frac{1}{2}\frac{a}{a+b}m_s$$

Eq. 66

Where m_{s_f} and m_{s_r} are the effective sprung mass value for each corner at the front and rear axles.

Now the individual tire stiffness parameters can be calculated as such:

$$\omega_{W.H.} = 2\pi\nu_{W.H.} \quad ; \quad k_t = m_t{\omega_{W.H.}}^2$$

Eq. 67

Similarly, the corner suspension stiffness parameters would be:

$$\omega_{ride_f} = 2\pi\nu_{ride_f} \quad ; \quad k_f = m_{s_f}{\omega_{ride_f}}^2$$

$$\omega_{ride_r} = 2\pi\nu_{ride_r} \quad ; \quad k_r = m_{s_r}{\omega_{ride_r}}^2$$

Eq. 68

Where ω_t is the natural frequency associated with wheel hop motion, and ω_{ride} is the natural frequency associated with heave motion and *f* and *r* subscripts indicate front and rear, respectively. Here k_t is the tire stiffness which is considered identical for all wheels, and k_f and k_r are the suspension stiffness coefficients at each corner suspension unit, for the front and rear axles.

Similarly, the damping coefficients for the suspension units would be calculated as:

$$b_f = 2\zeta_f m_{s_f}\omega_{ride_f} \quad ; \quad b_r = 2\zeta_r m_{s_r}\omega_{ride_r}$$

Eq. 69

To calculate the stiffness of the anti-roll bar, one must note that the corner suspensions themselves provide some roll stiffness, and the anti-roll bar stiffness is the difference between the total roll stiffness and the portion provided by the corner suspensions.

$$k_{\tau_f} = k_{\tau_{f_{total}}} - 2k_f\left(\frac{w}{2}\right)^2 \quad ; \quad k_{\tau_r} = k_{\tau_{r_{total}}} - 2k_r\left(\frac{w}{2}\right)^2$$

Eq. 70

Now all the parameters that participate in the equations of motion have been investigated.

3.9.Initial Conditions

The state variables involved in the equations of motion include the velocities associated with different inertias and displacements associated with springs. The initial longitudinal velocity of the vehicle is a non-zero cruising speed U_0 that is selected arbitrarily. This indicates that the simulation begins when the vehicle is going over a random road with a constant speed. The initial angular velocity of the wheels is also adjusted such that the fore-aft slip is initially zero for all wheels. The rest of the initial velocities are all zero.

$$U(t=0) = U_0 \ ; \ s(t=0) = 0 \ \rightarrow \omega_t(t=0) = \frac{U_0}{R}$$

Eq. 71

As the vehicle is being modeled as if in a gravity field, the springs employed in the model would have an initial displacement due to gravity. To obtain this initial displacement, the steady-state equations are solved where every state derivative is assumed to be zero. The initial displacement for the springs in the front and in the rear are different as the vehicle's mass distribution is longitudinally asymmetric and the center of gravity is closer to the front axle.

Once the effective corner masses are obtained, the initial spring displacements are calculated according to the effective static weight that they support.

$$q_c(t=0) = \frac{m_c g}{k_c} \quad ; \quad q_{t_c}(t=0) = \frac{(m_t + m_c)g}{k_t}$$

Eq. 72

Where the c subscript indicates the individual corner of interest.

3.10. Validation

To ensure that the vehicle model can reasonably predict the dynamics of a real vehicle, the present model needs to be validated against established literature. The validation effort at hand needs to verify that a proper input to the vehicle model would result in an appropriate output. This would include ensuring that the correct random road signal is generated and fed into the model in terms of the input signals. Furthermore, to validate the suspension modeling, appropriate levels of heave acceleration must be observed that correspond to published literature, and finally to validate the horizontal dynamics' predictions, the kinematic signals of the vehicle in response to a step-steer maneuver would be compared to the predictions of CarSim, a commercially available and recognized vehicle dynamics software.

3.11. Random Road Generation

Various road profiles with different levels of roughness are recognized and differentiated in the ISO 8608[94]. To generate a random road, a random temporal signal is generated and its mean is subtracted from the original signal to ensure zero mean. An appropriate amplitude gain is applied to the signal. To ensure the generated road falls within acceptable road profiles, the road roughness displacement levels of the generated road is compared to those in ISO8608.

Fig. 30 depicts a typical generated random road for the right and left tracks of the vehicle.

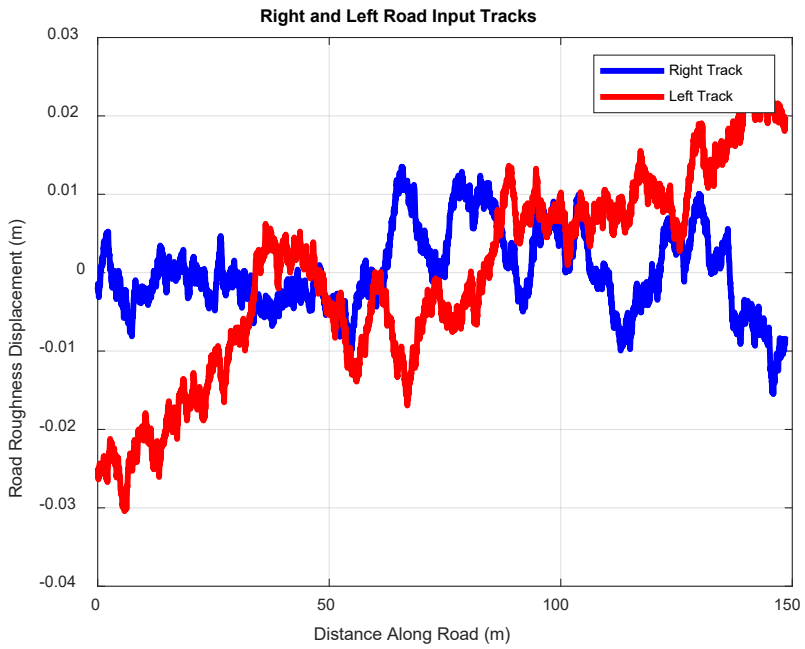

Figure 30 The generated random road for the right and left tracks

Fig. 30 shows that the generated random road corresponds well to a relatively smooth road as recognized by ISO8608 according to the amplitude and frequency content of the road profile.

This verifies that the road input is generated properly.

3.12. Vertical Dynamics Validation

To validate the vertical dynamics, the vehicle was subjected to the random road input and simulated for a constant speed of $U_0 = 25$ m/s. Fig. 31 shows the time-history of the heave acceleration of the center of gravity of the vehicle body.

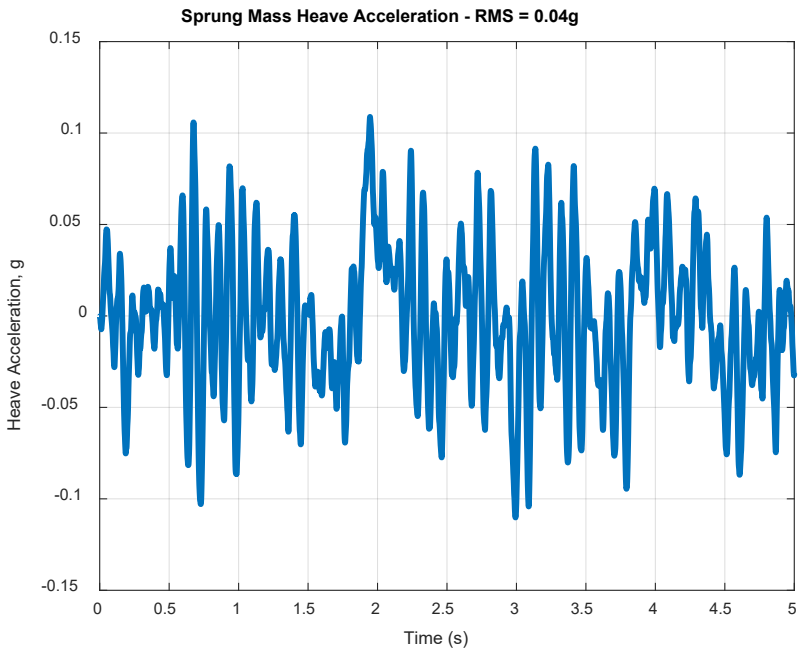

Figure 31 Heave acceleration response of the vehicle body's center of gravity

The vehicle body has experienced an RMS value of 0.04g's that corresponds well to the levels of heave acceleration of a vehicle traversing a smooth road[95]. To validate the vertical dynamics, one also needs to investigate the displacement across the suspension (rattlespace). Fig. 32 shows this displacement for the four corners.

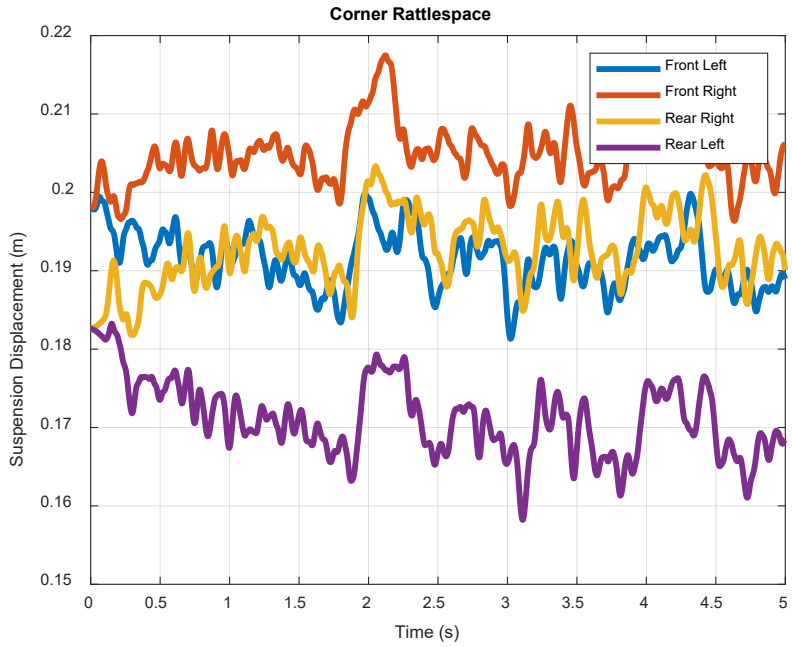

Figure 32 Suspension displacement for the four corners

As is evident in Fig. 32, the suspension displacements are different for all corners due to different right-left road tracks and different front-rear weight distribution, yet they are all within the same appropriate range [citation here]. Therefore, the predictions of the suspension units are reasonable and therefore the random road input is adequately "felt" across the vehicle body.

3.13. Horizontal Dynamics Validation

To validate the model for horizontal dynamics, the present vehicle model was compared to CarSim's predictions. CarSim is a commercially available vehicle dynamics software that incorporates minute details in its modeling procedure and has been validated against experiment for a wide range of vehicles. For the validation task at hand, the vehicle was simulated for initially going straight and after one second, a step-steer input of 1 degree of front steering angle $\delta=1°$ was applied. Horizontal kinematic signals including yaw rate, lateral

acceleration, and vehicle trajectory were investigated compared to CarSim's predictions. Fig. 33 shows the comparison plots.

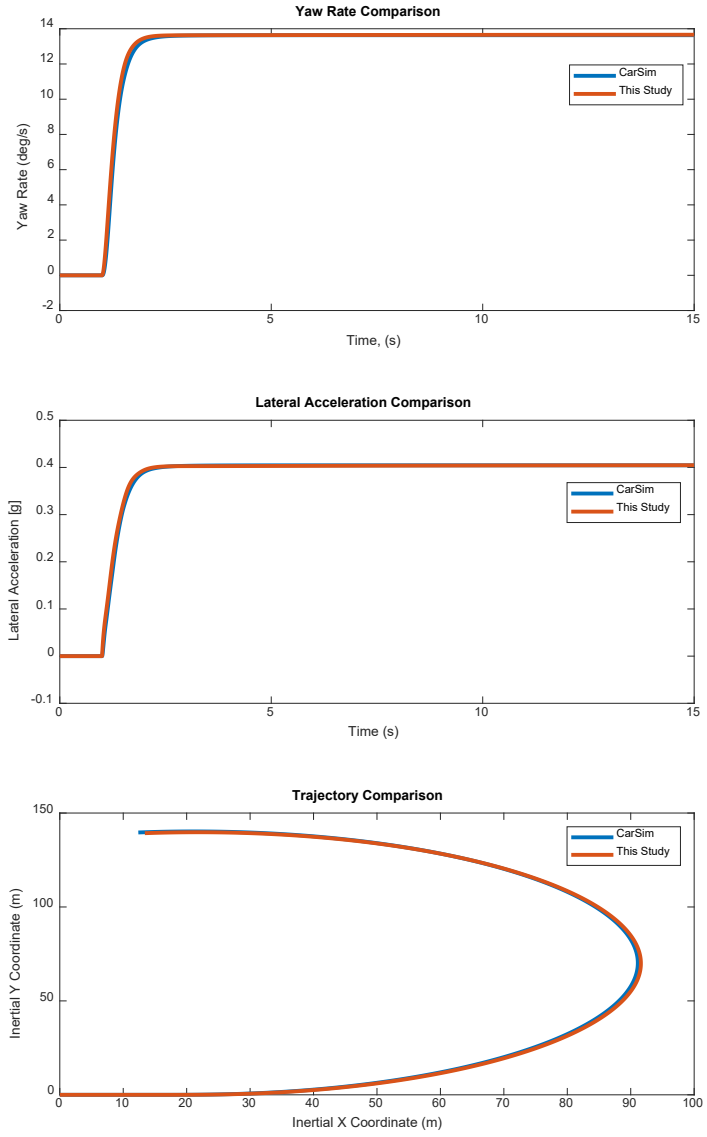

Figure 33 Horizontal dynamics validation against CarSim

As can be seen in Fig. 33, the low-order model developed here has replicated CarSim's outputs and the model's response is virtually identical to that of CarSim's. This demonstrates the power of low-order models and provides some confidence that the model predictions for the vehicle horizontal dynamics are reasonably accurate.

3.14. Seat Track Velocity and Acceleration

Given that the disturbance inputs from the vehicle to the passenger model in chapter 2 were velocity signals at the seat track, the seat track velocities need to be investigated for each seat that a passenger might sit in. This requires a velocity transfer from the center of gravity of the sprung mass to the seat track location. Fig. 34 shows the relative position of the seat tracks with respect to the vehicle body's center of gravity that are required for the velocity transfer.

Figure 34 Relative position for the seat tracks with respect to the CG

Also to compare the information coming from the passenger model with the currently established ride comfort metrics, the acceleration of the seat track should also be investigated. The acceleration transfer from the center of gravity would look like:

$$\vec{a}_{s.t.} = \vec{a}_{CG} + \vec{\dot{\omega}} \times \vec{r}_{s.t.} + \vec{\omega} \times \vec{\omega} \times \vec{r}_{s.t.}$$

Eq. 73

Where the s.t. subscript indicates the seat track of interest and $\vec{r}_{s.t.}$ is the position vector from the center of gravity to the mentioned seat track.

3.15. Conclusion

A full car model was developed including all spatial degrees of freedom and its predictions were validated against established literature. Even though the model is minimal and incorporates only the necessary complexities, it can sufficiently approximate a real vehicle, as demonstrated in validation plots.

Now that both the vehicle model and the passenger model have been developed, the passenger model can be subjected to the disturbance inputs from the vehicle model and its propagation within the passenger model can be investigated. However, before the vibration responses from the passenger model can become a source of inference for ride comfort estimation, a ride comfort metric needs to be established.

4. Devising the Ride Metric

Now that both the passenger model and the vehicle model have been developed, a novel ride comfort metric can be investigated. The hypothesis from Chapter 1 is that the ride comfort metric would eventually be an index that represents the total internal displacements within the passenger model due to the disturbance vibration coming from the vehicle.

In this Chapter, the ride-comfort metric is developed as a function of the important local displacements from the passenger model. In order to determine the range of the numerical value of the prospective metric, currently established industrial metrics for ride comfort will be compared to the present study, such that the model would be exposed to disturbance signals that drive the established metric to the threshold of discomfort, and the passenger model's response would be recorded and later employed in choosing the range of the newly developed metric.

4.1. Established industrial ride comfort metrics

To justify the need for developing a new ride comfort metric, the calculation mechanism behind the established standards needs to be investigated such that they can be compared with one another. The industrial standards of interest include the ISO2613[16], the BS6841[43], and the VDI2057[42]. Els [44] argued that while these established metrics agree in their trend for ride comfort, i.e. the higher the net acceleration, the lower the comfort, they do not agree on the comfort zone and that their suggested ranges for a comfortable ride do not overlap.

In what follows, the three mentioned standards will be investigated and adapted into the model. All three standards associate ride comfort with acceleration, with ISO2631 and BS6841 considering all translational accelerations and VDI2057 only considering heave acceleration.

4.1.1. ISO2613

Perhaps the most commonly used industrial metric for ride comfort is the ISO2631, initially released by the International Standards Organization in 1989, then revised in 2003 and 2018. This standard considers all of the translational accelerations to which the human body is subjected and arrives at a "net" acceleration upon filtering the input acceleration signals with a few designated frequency filters and ultimately specifies values for comfortable and uncomfortable ranges of motion. However, ISO2631 is known to have particular emphasis on the vertical direction while ignoring the longitudinal and lateral directions[3, 18, 19].

The frequency filters are selected according to the responses of human subjects and the comfort-evaluation surveys. Fig. 35 shows a block diagram of how the net acceleration is calculated in ISO2631.

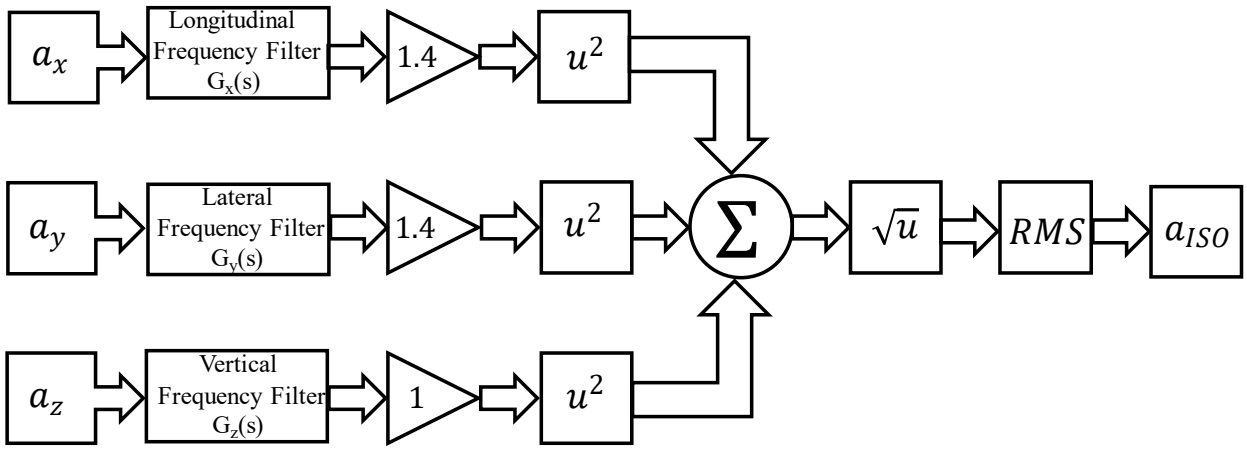

Figure 35 Block diagram for ISO2631 calculations of an effective, net acceleration

The frequency filters for ISO2631's calculation of the effective, net acceleration come from experiments with human subjects. ISO2631 gives the frequency filters for all translational degrees of freedom in a frequency response plot similar to that given in Fig. 36.

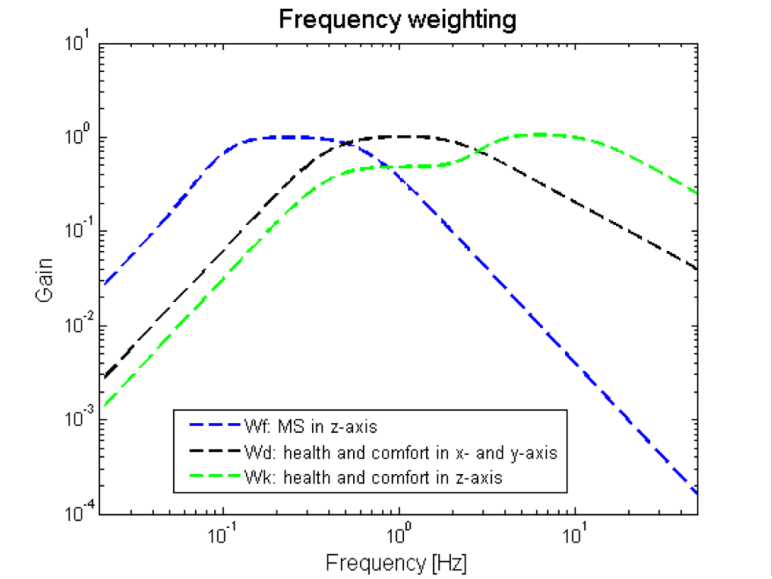

Figure 36 Frequency weightings given by ISO2631[16]

Where W_k is the frequency weighting for the vertical direction, W_d is the frequency weighting for both longitudinal and lateral directions, and W_f is a suggested frequency weighting for the study of motion sickness, which is not investigated in this study.

However, to implement the suggested frequency weightings given in Fig. 36, Rimell et al. have devised frequency filters that correspond to ISO2631's frequency weightings with high fidelity[96]. These frequency filters comprise a cascade of transfer functions including a high-pass filter, a low-pass filter, a velocity-acceleration transitional filter, and an upward step filter. The frequency filters suggested by Rimell et al. to replicate ISO2631's frequency weightings are as follows:

$$G_{x_{ISO}}(s) = G_{y_{ISO}}(s) = \left(\frac{s^2}{s^2 + (2\pi 0.4)\sqrt{2}s + (2\pi 0.4)^2}\right)\left(\frac{(2\pi 100)^2}{s^2 + (2\pi 100)\sqrt{2}s + (2\pi 100)^2}\right)\left(\frac{(2\pi 2)s + (2\pi 2)^2}{s^2 + (2\pi 2)1.59s + (2\pi 2)^2}\right)$$

$$G_{z_{ISO}}(s) = \left(\frac{s^2}{s^2 + (2\pi 0.4)\sqrt{2}s + (2\pi 0.4)^2}\right)\left(\frac{(2\pi 100)^2}{s^2 + (2\pi 100)\sqrt{2}s + (2\pi 100)^2}\right)\left(\frac{(2\pi 12.5)s + (2\pi 12.5)^2}{s^2 + (2\pi 12.5)1.59s + (2\pi 12.5)^2}\right)\left(\frac{s^2 + (2\pi 2.37)1.1s + (2\pi 2.37)^2}{s^2 + (2\pi 3.3)1.1s + (2\pi 3.3)^2}\right)$$

Eq. 74

The raw acceleration signals a_x, a_y, a_z are filtered with the suggested frequency weightings to yield A_x, A_y, A_z and then the net acceleration according to ISO2613 would be calculated as follows.

$$\bar{a}_{ISO} = \sqrt{(1.4A_x)^2 + \left(1.4A_y\right)^2 + (A_z)^2}$$

$$a_{ISO} = RMS(\bar{a}_{ISO}) = \sqrt{\frac{1}{T}\int_0^T {\bar{a}_{ISO}}^2 dt}$$

Eq. 75

Where T is the duration of simulation that is selected much larger than the largest natural period of oscillations (larger than the reciprocal of the smallest natural frequency).

4.1.2. BS 6841

The British standard BS6841 was initially introduced in 1987 by the British Standards Institution and has been most recently revised in 2020[43]. BS6841 is yet another major acceleration-based standard that suggests ranges of comfortable exposure to acceleration disturbance. All translational accelerations are considered in BS6841, with an emphasis on the vertical direction.

While the procedure used in calculating the net, effective acceleration in BS6841 is very similar to that for ISO2631, they are different in the implemented frequency filters, the gains applied to each directional acceleration, and finally BS6841 uses a quartic-order calculation instead of an RMS (Root Mean Square). Fig. 37 shows a schematic of the BS6841 net acceleration calculation.

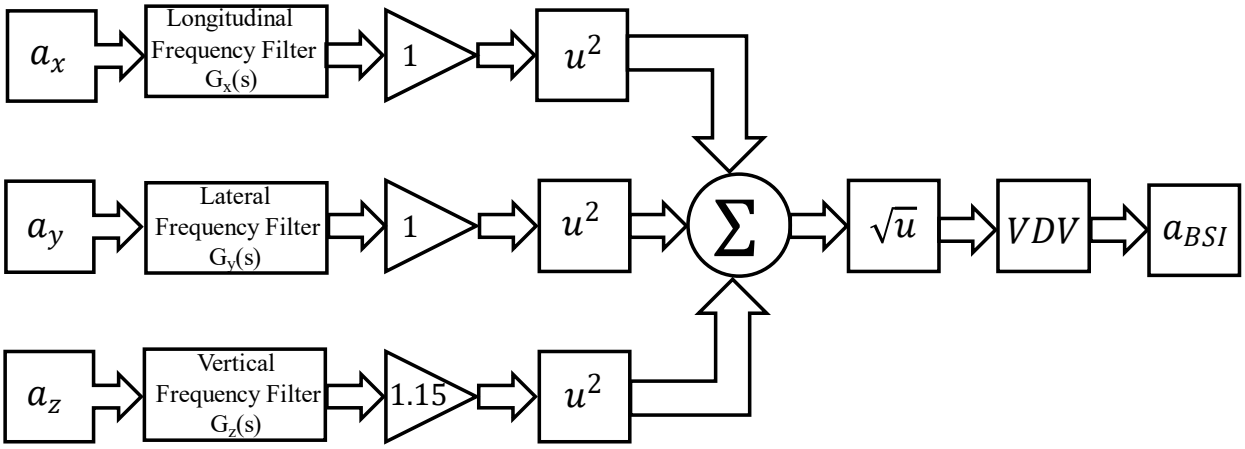

Figure 37. Block diagram for BS6841's calculation of an effective, net acceleration

Similar to ISO2631, there are suggested frequency filters that fit the weightings suggested by BS6841 given by Rimmel et al. [96] as follows:

$$G_{x_{BSI}}(s) = G_{y_{BSI}}(s) = \left(\frac{s^2}{s^2 + (2\pi 0.4)\sqrt{2}s + (2\pi 0.4)^2}\right)\left(\frac{(2\pi 100)^2}{s^2 + (2\pi 100)\sqrt{2}s + (2\pi 100)^2}\right)\left(\frac{(2\pi 2)s + (2\pi 2)^2}{s^2 + (2\pi 2)1.59s + (2\pi 2)^2}\right)$$

$$G_{z_{BSI}}(s) = \left(\frac{s^2}{s^2 + (2\pi 0.4)\sqrt{2}s + (2\pi 0.4)^2}\right)\left(\frac{(2\pi 100)^2}{s^2 + (2\pi 100)\sqrt{2}s + (2\pi 100)^2}\right)\left(\frac{(2\pi 16)s + (2\pi 16)^2}{s^2 + (2\pi 16)1.82s + (2\pi 16)^2}\right)\left(\frac{s^2 + (2\pi 2.5)1.11s + (2\pi 2.5)^2}{s^2 + (2\pi 4)1.05s + (2\pi 4)^2}\right)$$

Eq. 76

The differences in the frequency filters for ISO2631 and BS6841 is particularly noticeable for the vertical direction. Fig. 38 shows a comparison of the frequency filters suggested for the vertical direction between the two standards.

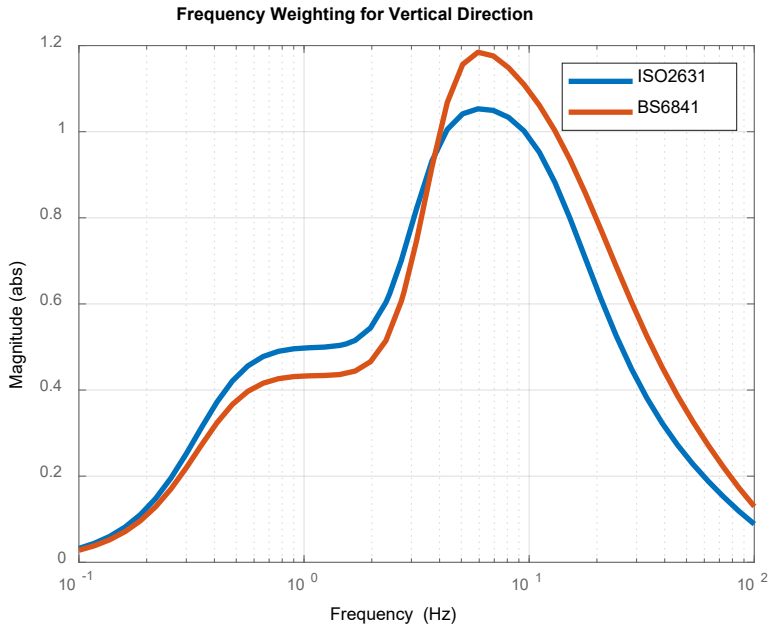

Figure 38. Comparison of the frequency weightings between ISO2631 and BS6841

Fig. 38 suggests that the two standards emphasize different frequency ranges within the vehicular motion's frequency range [1-10 Hz], such that motions below 4Hz get higher weights from ISO2631 whereas BS6841 amplifies motions above 4Hz and below 10Hz.

Once the raw acceleration signal is frequency-weighted, the filtered A_x, A_y, A_z signals would combine to make up the BS6841's effective, net acceleration. The BS6841 uses a quartic averaging and its result is called the VDV (Vibration Dose Value).

$$\bar{a}_{BSI} = \sqrt{(A_x)^2 + \left(A_y\right)^2 + (1.15A_z)^2}$$

$$a_{BSI} = VDV(\bar{a}_{BSI}) = \sqrt[4]{\frac{1}{T}\int_0^T {\bar{a}_{BSI}}^4 dt}$$

Eq. 77

The outputs of the ISO2631 and BS6841 are an effective net acceleration which can be interpreted in terms of ride comfort according to Table 1.

a_{net}	Comfort Interpretation
$a_{net} < 0.315\ ms^{-2}$	Not Uncomfortable
$0.315ms^{-2} \leq a_{net} \leq 0.63ms^{-2}$	A Little Uncomfortable
$0.5ms^{-2} \leq a_{net} \leq 1ms^{-2}$	Fairly Uncomfortable
$0.8ms^{-2} \leq a_{net} \leq 1.6ms^{-2}$	Uncomfortable
$1.25ms^{-2} \leq a_{net} \leq 2.5ms^{-2}$	Very Uncomfortable
$a_{net} > 2\ ms^{-2}$	Extremely Uncomfortable

Table 14. Interpretation guide for the calculated effective, net acceleration used in ISO2631 and BS6841

4.1.3. VDI2057

The last industrial ride comfort metric investigated in this study is the VDI2057[42]. This standard was initially developed by the Association of German Engineers[3] in 1963 and its latest revision has occurred in 2017. The VDI2057 solely considers the vertical acceleration and uses the same frequency weighting as ISO2631. However, VDI2057 has its own procedure for calculating a ride metric. Once the a_z vertical acceleration signal is weighted according to the ISO2631's frequency filters, the filtered acceleration signal A_z would be subjected to an FFT (Fast Fourier Transform) frequency decomposition. Next, the frequency distribution of the filtered acceleration signal is manipulated according to the frequency range of interest and finally the K-factor ride comfort index is obtained. The K-factor will be compared to a subjective table which determines the level of ride comfort.

[3] Verein Deutscher Ingenieure

$$a_z(t) \xrightarrow{G_{z_{ISO}(s)}} A_z(t) \overset{\mathcal{F}}{\Rightarrow} A_z(\omega), \omega = 2\pi f$$

$$K_z(f) = 10\sqrt{f}A_z(f) \quad 1 \leq f \leq 4\ Hz$$

$$K_z(f) = 20A_z(f) \qquad 4 \leq f \leq 8\ Hz$$

$$K_z(f) = 160\frac{A_z(f)}{f} \qquad 8 \leq f \leq 80\ Hz$$

Eq. 78

Once the frequency-dependent $K_z(f)$ is calculated for all frequencies, its value would be integrated over the entire frequency range and the K-factor will be obtained.

$$K_{VDI} = \int_{1Hz}^{80Hz} K_z(f)df$$

Eq. 79

Once K_{VDI} is calculated, Table 2 would determine the ride's comfort level[97].

K_{VDI} Threshold	Subjective Perception of Discomfort
0.1	There is no oscillation
0.25	The first sensations appear
0.63	Minimum level of sensations
1.6	It feels good
4	Oscillations feel "strong"
10	Very strong level of perception
25	Very strong level of perception
63	Very strong level of perception

Table 15. The subjective guide to interpreting the K_{VDI}

To verify the discrepancy between the comfort zone predicted by the aforementioned industrial standards, the model is driven with certain levels of random road excitation to arrive at the discomfort threshold as predicted by each individual standard. In each case, the predictions of the other two standards are also be recorded. Finally, a comparison among the three shows whether they agree. Therefore, for ISO2631 and BS6841, the model was run over a rough random road that would generate a value of $a_{net} \approx 1.2\ m/s^2$ and for VDI2057 the model was run over a random road that would cause a value of $K_{VDI} \approx 4$, which indicate the given threshold of discomfort in all standards. After recording the comfort index from all three standards for 20 separate runs of the simulation, the comfort indices are compared in Table 3.

	ISO2631 (m/s^2)	**BS6841 (m/s^2)**	**VDI2057**
ISO2631 $a_{net} \approx 1.2\ m/s^2$	-	1.68 Very Uncomfortable	3.31 Comfortable
BS6841 $a_{net} \approx 1.2\ m/s^2$	0.86 Fairly Uncomfortable	-	2.48 Comfortable
VDI2057 $K_{VDI} \approx 4$	1.67 Very Uncomfortable	2.18 Extremely Uncomfortable	-

Table 16. Comparison of the established ride metrics at their individual threshold of discomfort

Table 3 indicates that while the introduced metrics agree on the trend that higher acceleration exacerbates the perception of ride comfort, they do not agree on the zones of comfort. Hence, developing a new ride comfort metric could be beneficial. At this point all industrial, quantitative ride-comfort metrics have been investigated and we shall proceed to defining our new metric.

4.2. The Novel Ride Comfort Index

In Chapter 1 it was mentioned that the currently established ride-comfort indices do not all match and their predicted zones of comfort do not overlap. It is hypothesized that a most comfortable ride would be that which induces the least internal motion within a passenger's body. Chapter 2 introduced a biomechanical model of a vehicle passenger that would enable the calculation of the internal displacements within the body when subjected to disturbance vibrations from a vehicle. Chapter 3 gave the vehicle model that would generate said disturbance and now we wish to define a new ride comfort metric according to the outputs of the passenger model that has been subjected to vehicular vibration disturbance.

Chapter 2 showed how the lower lumbar region within a passenger's body, namely the L5S1 and the L4L5 discs, display the greatest translational vibration transmissibility in the vehicular frequency range. The neck also showed the greatest rotational vibration transmissibility. Given how chronic lower-back pain is associated with the lower lumbar region[58, 98, 99] and how the motion of the head has been associated with whiplash[100] and a passenger's perception of ride comfort[101], the local displacements of the said three joints being the L5S1, the L4L5, and the neck are considered for developing the biomechanical ride comfort index. This adds up to 9 total displacements including axial, shear, and rotary displacements for the above-mentioned joints.

These local displacements vary in magnitude as well as dimension, and therefore their absolute value cannot directly contribute to developing a displacement index. Consequently, the local displacements first need to be normalized and non-dimensionalized in order to lend themselves to a ride comfort index.

4.2.1. Non-Dimensionalization

Given that the passenger model is subject to gravity and how the model has a curved geometry, every local displacement has a non-zero, static equilibrium, initial condition. When subjected to disturbance excitation, the displacement signals oscillate around that static equilibrium point.

To come up with a non-dimensional, normalized variable that can be combined with other similar variables to form a ride comfort index, the target local displacements are subtracted from their static equilibrium value to find their deviation from said position. This displacement deviation signal is divided by the static equilibrium value to yield a non-dimensional, normalized version of the displacement of interest.

$$q^* = \frac{q - q_0}{q_0} \quad ; \quad q = \{q_{a_{L5S1}}, q_{s_{L5S1}}, q_{r_{L5S1}}, q_{a_{L4L5}}, q_{s_{L4L5}}, q_{r_{L4L5}}, q_{a_{Neck}}, q_{s_{Neck}}, q_{r_{Neck}}\}$$

Eq. 80

Here the name of the joint of interest is added as a subscript next to all considered displacements and the a, s, r subscripts indicate axial, shear, and rotary displacements, respectively.

Now the new non-dimensional, normalized q^* variables can be arithmetically manipulated, and their respective numerical value is comparable as they signify the deviation from the individual static equilibrium position for each displacement.

The proposed ride comfort metric is an index that combines the deviation of the 9 important displacements from their static equilibrium position. Since the contribution of these individual displacements to discomfort might not be equal to one another, individual weights are considered for each non-dimensional displacement. And to avoid cancellation of the positive and negative deviations with one another, the square of the non-dimensional displacements is considered in making up the ride comfort index, which is given as follows.

$$A.R.C = \int_0^{\infty} \sum_{i=1}^{9} w_i {q_i}^{*2}\, dt$$

Eq. 81

Where ARC stands for (Author's initials) Ride Comfort, and the proposed ride comfort index will be henceforth known as the ARC. Building on the original hypothesis, a ride which corresponds to the smallest possible ARC would be most comfortable. Also, the w_i are the weighting factors that indicate the contribution of each individual displacement deviation to the perception of discomfort. The ARC is technically a measure of discomfort and therefore the lower the ARC, the more comfortable the ride.

4.2.2. Weightings

To come up with the values for the weighting gains, a non-dimensional energy signal is introduced as the temporal integral of the square of the magnitude of the non-dimensional displacement deviation signal for each of the 9 displacements, which in turn is related to the frequency integral of the square of the magnitude of the same signal in the frequency domain according to Parseval's Identity for Fourier Transforms as follows:

$${E_i}^* = \int_{-\infty}^{\infty} |{q_i}^*(t)|^2 dt = \frac{1}{2\pi} \int_{-\infty}^{\infty} |{Q_i}^*(\omega)|^2 d\omega$$

Eq. 82

Making use of Parseval's identity here, the second integral is calculated for each of the non-dimensional displacements. These non-dimensional energy signals represent the energy associated with that particular displacement. Since the displacement signals have been normalized, the amount of associated energy can be employed to come up with the weightings for the ARC. The

thought process here is that the displacement deviation which has the smallest associated energy, would have the smallest weight. Or the deviation displacement which has the greatest associated energy would earn the greatest weight and its displacement would be penalized more than the others. Therefore, all non-dimensional energy signals would be normalized with respect to their minimal value and the resulting quotient would become the weighting factor for that particular energy.

$$E^* = \bigcup_{i=1}^{9} {E_i}^* \quad ; \quad w_i = \frac{{E_i}^*}{\min\,(E^*)}$$

Eq. 83

To obtain the resulting weights from Eq. 83, the model was run 100 times with each run having a new random road as its disturbance input. It was determined that the smallest non-dimensional energy was always found to be associated with the axial displacement of the L5S1 joint. The mean value and the standard deviation of the weight factors corresponding to each displacement were recorded and are given in Table 4.

	$w_{a_{L5S1}}$	$w_{s_{L5S1}}$	$w_{r_{L5S1}}$	$w_{a_{L4L5}}$	$w_{s_{L4L5}}$	$w_{r_{L4L5}}$	$w_{a_{Neck}}$	$w_{s_{Neck}}$	$w_{r_{Neck}}$
$\bar{x}$	1	2.0642	2.3256	1.2714	8.2959	5.0049	1.6123	1.7752	2.5388
σ	0	0.0406	0.1632	0.0087	0.4351	0.3189	0.0343	0.5316	0.7406
$\frac{\sigma}{\bar{x}}$ (%)	0	1.96	7.01	0.68	5.24	6.37	2.13	29.94	29.17

Table 17. the mean and the standard deviation of the individual weighting factors across 100 runs of the simulation

It was found that for all lumbar displacements, the standard deviation turns out to be a very small fraction of the mean, meaning that the weights associated with the L5S1 and L4L5 joints turn out to be more or less the same every time the simulation is run over a new random road. However,

the standard deviation of the weighting factor for the neck joint's shear and rotary displacements turned out to be a substantial fraction of their respective mean (around 30%), which indicates that the weighting factors change substantially for the neck joint for each simulation. Therefore, the neck joint's behavior does not lend itself to the definition of the ride comfort index given here and is therefore excluded in the calculation of the proposed ride metric. The finalized ARC is given as:

$$A.R.C = \int_0^{\infty} \left\{ \left(q^*{}_{a_{L5S1}} \right)^2 + 2.06 \left(q^*{}_{s_{L5S1}} \right)^2 + 2.33 \left(q^*{}_{r_{L5S1}} \right)^2 + 1.27 \left(q^*{}_{a_{L4L5}} \right)^2 + 8.30 \left(q^*{}_{s_{L4L5}} \right)^2 + 5 \left(q^*{}_{r_{L4L5}} \right)^2 \right\} dt$$

Eq. 84

Now that the ride comfort metric has been established, controllers can be designed to minimize ARC as a cost function to enhance ride comfort.

4.3.Conclusion

It was shown that the currently established industrial ride comfort metrics do not agree with one another. It was hypothesized that a biomechanical model of a passenger aboard a vehicle that can predict the internal dynamics within the body can help determine whether a ride is comfortable. A novel ride comfort metric, known as ARC, was devised as a measure of the combined, weighted displacement deviations within the lowermost lumbar joints in the Passenger Model. ARC becomes the cost function that needs to be minimized for the most comfortable ride.

5. Controller Design and Actuation

In the previous Chapters, research was conducted to devise a novel ride comfort metric from a biomechanical perspective. In this chapter, we will develop a control strategy to optimize the given ride comfort cost function introduced in Chapter 4.

5.1. Actuator Location

Most studies that develop ride comfort strategies for a vehicle's passengers achieve improvements by control of the vehicle's suspension system[45, 48, 52]. Use of active control for the suspension system requires significant power and adds other concerns such as road holding and constraints due to vehicle handling requirements. Hence this research focuses control strategy by proposing active control of the vehicle seats to improve ride comfort.

Upon creating the passenger's biomechanical model in Chapter 2, it was assumed that the seat makes contact with the passenger's body in 3 locations: the hip cushion at the bottom, and the lumbar and the thoracic backrest supports. In reality, these places of contact are spread over a finite area, however, they have been considered as singular points for the simplicity of the model. It is assumed that force actuators are positioned at the same locations as the springs and dampers that represent the seat passive connection. For the purpose of controller design, it is assumed that the actuators can instantly provide the required forces. Fig. 39 shows a schematic of the seat system equipped with active force actuators marked with circles.

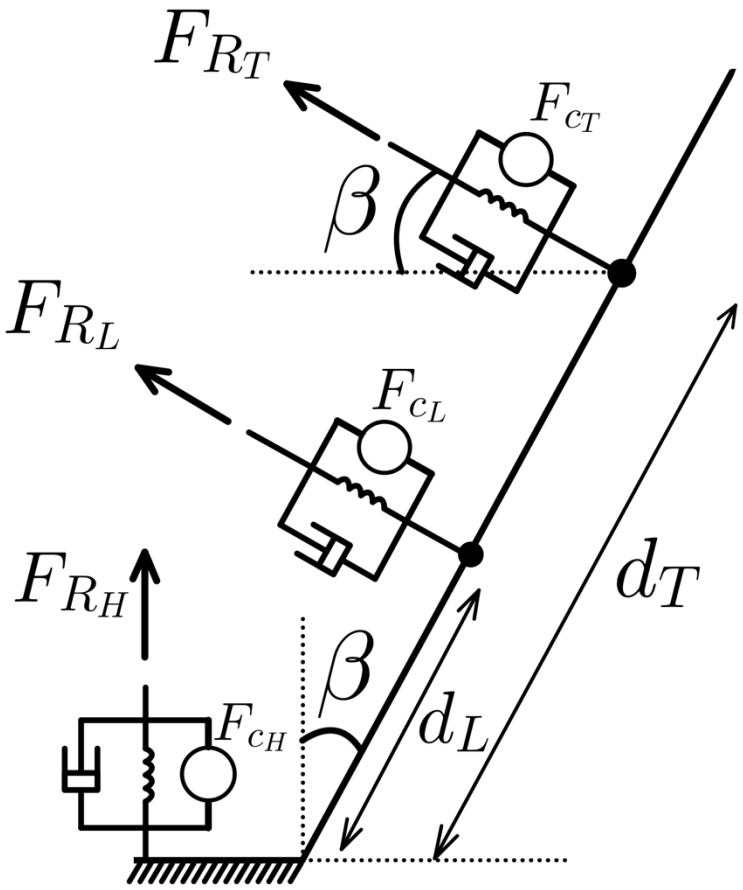

Figure 39. Schematic of proposed seat actuators

Here F_{c_H}, F_{c_L}, F_{c_T} represent the controlled actuator force in the hip cushion, lumbar backrest, and thorax backrest, respectively.

5.2.Control philosophy

Given that the equations of motion for the model have been developed in a state-space and that the cost function (A. R. C.) is quadratic (Eq. 81), linear state-variable feedback control is considered as a control strategy. This of course requires that linearization of the model results in an acceptable representation of the original system.

5.3.Linearization

The non-linear passenger model developed in Chapter 2 has been linearized around its equilibrium position with non-linear terms having been evaluated at said equilibrium position and treated as constant for the remainder of the analysis. The state-space representation is given as follows:

$$\dot{\vec{x}}_{84\times1} = A_{84\times84}\,\vec{x}_{84\times1} + B_{84\times5}\,\vec{u}_{5\times1} \quad ; \quad \vec{x}(0) = \vec{x}_0$$

$$\vec{u} = [W_s, \omega_p, F_{c_H}, F_{c_L}, F_{c_T}]^T$$

Eq. 85

It must be noted that given that the variations in the cruise input U_s is negligible compared to the heave W_s and pitch ω_p inputs, thus the cruise input is treated as constant whose effect has been considered in the initial conditions of the linearized model. Therefore, the linearized model would comprise 84 states (8 angular positions, 25 velocities, 33 displacements, and 18 translational positions). The input vector $\vec{u}$ consists of two disturbance inputs W_s and ω_p, and three controlled inputs F_{c_H}, F_{c_L}, F_{c_T}.

To test the accuracy of the linearization, the passive system is subjected to a heave and pitch disturbance and the predictions of the linearized model are compared to the non-linear model. Fig.40 compares the linear model to the non-linear model for two important displacements: the shear displacement of the L4L5 joint (Fig.40 (a)), and the rotational displacement of the L5S1 joint (Fig.40 (b)).

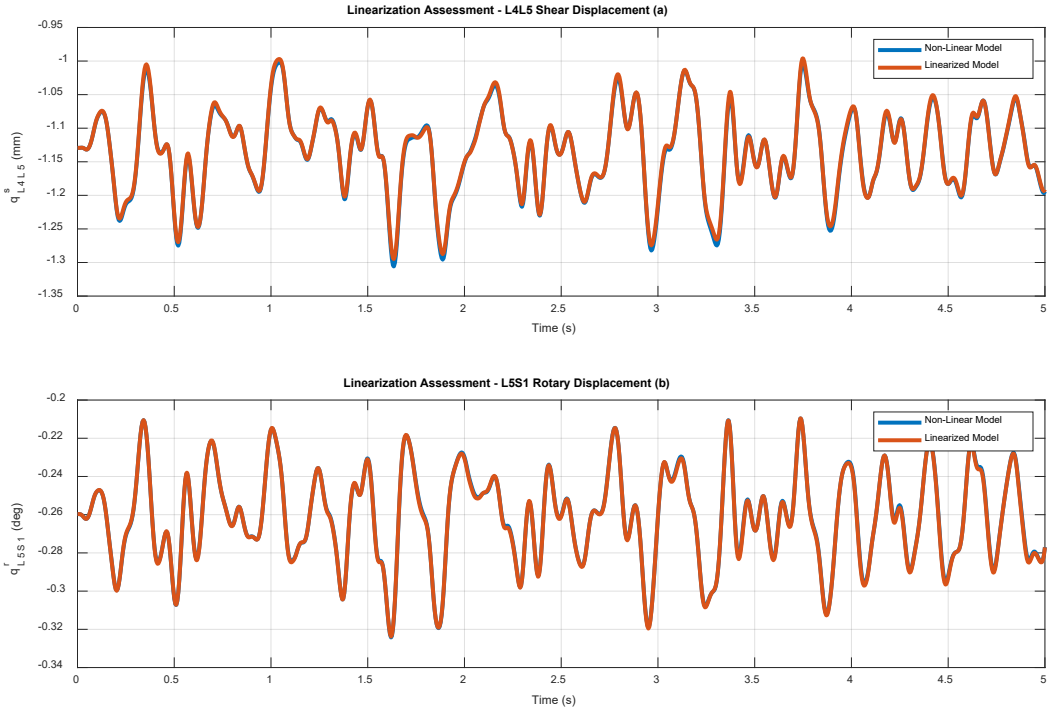

Figure 40. Comparing the predictions of the linearized model to the nonlinear model for two typical states

Figs. 40 verifies that the linearized model can accurately track the non-linear model predictions in response to disturbance inputs and therefore the linearization has been successful. We can now proceed to design the linear state-variable feedback control.

5.4.Controller Design – LQR

A Linear Quadratic cost function has been proposed and a Linear Quadratic Regulator (LQR) is used for the control of the 3 actuators. The LQR algorithm gives the state-gain matrix K such that when multiplied by the state vector yields commands to the actuators that will minimize the quadratic cost function [102].

$$J = \int_0^\infty (x^T Q x + u^T R u + 2x^T N u) dt$$

$$\vec{u} = -K\vec{x} \rightarrow J_{min}$$

Eq. 86

Here J is the total cost function, Q and R are weighting matrices for the states and inputs, respectively, and N is a weighting matrix for any non-linear cross term in the cost function that might include the product of a state and an input. Once the gain matrix K is found, assuming one has access to the states, then $-K\vec{x}$ input will ensure the cost function would arrive at a global minimum.

The cost function is re-written in terms of ARC and the specified inputs.

$$J = \int_0^\infty \left\{ \sum_{i=1}^{6} Q_i {q_i}^{*2} + R_1 {F_{c_H}}^2 + R_2 {F_{c_L}}^2 + R_3 {F_{c_T}}^2 \right\} dt = ARC + \int_0^\infty \left(R_1 {F_{c_H}}^2 + R_2 {F_{c_L}}^2 + R_3 {F_{c_T}}^2 \right) dt$$

Eq. 87

The Q_i weights are selected to match the found weightings in Chapter 4 for ARC and the R_i weights are selected such that ARC is minimized while not consuming excessive energy. Table 18 gives the employed values for Q_i and R_i weights.

Q_1	Q_2	Q_3	Q_4	Q_5	Q_6	$R_1 = R_2 = R_3$
$\frac{1}{\left({q_0}^a{}_{L5S1}\right)^2}$	$\frac{2.06}{\left({q_0}^s{}_{L5S1}\right)^2}$	$\frac{2.33}{\left({q_0}^r{}_{L5S1}\right)^2}$	$\frac{1.27}{\left({q_0}^a{}_{L4L5}\right)^2}$	$\frac{8.3}{\left({q_0}^s{}_{L4L5}\right)^2}$	$\frac{5}{\left({q_0}^r{}_{L4L5}\right)^2}$	0.0001

Table 18. Given Q_i and R_i weights for the LQR function

The LQR algorithm was run using MATLAB and the gain matrix K was produced. The LQR function only depends on the A and B matrices of the state space representation, and it can find the global, cost-function-minimizing inputs as long as the linearized state space is stabilizable, i.e., the uncontrollable part of the A matrix has no positive eigenvalues and is stable.

With the gain matrix at hand, the vehicle model was simulated to traverse a random road and it was assumed that the passenger is sitting in the rear right seat and the associated seat track velocities were calculated using a velocity transfer from the center of gravity. The seat track velocities become input to the passenger model. Upon simulation of the nonlinear model with a controlled input vector equal to $-K\vec{x}$, it was found that the proposed controller reduces ARC by 60% in a span of 5 seconds of going over a random road. However, the controller design process is not yet done. Although LQR finds the optimal solution, it uses state-variable feedback and therefore assumes that we have real-time access to the system states. This is generally not a valid assumption. We do not have access to the state variables unless we measure all 84 of them, which is neither practical nor feasible. However, we could place sensors in strategic locations that could give us access to some states or linear combinations of them. Thus, to find the other states, it is necessary to design an observer that could estimate the states of the linearized state space, such that they could subsequently be used in state-variable feedback control.

5.5.Observer design – Kalman filter

In order to be able to estimate the system's states, an observer is designed which uses a few practical outputs of from the system and estimates the states accordingly. For practicality and to facilitate the implementation of the research at hand, it is assumed that we have placed sensors collocated with the actuators. Therefore, there would be sensors at each contact location that will measure the displacements in the hip cushion, lumbar backrest, and thorax backrest. Now we proceed to design an observer that takes in said measurements and yields estimates of the states. The estimator equations are shown in Eqs. (88).

$$\dot{\hat{x}} = A\hat{x} + Bu + L(y - \hat{y}) \quad ; \quad \hat{y} = C\hat{x}$$

$$\dot{\hat{x}} = A\hat{x} + Bu + Ly - LC\hat{x} = (A - LC)\hat{x} + [B\ L]\begin{bmatrix} u \\ y \end{bmatrix}$$

Eq. 88

Here A and B are the same system matrices from the linearization, C is the matrix that associates the sensor outputs with the system states, and L is the observer gain matrix which determines the performance of the estimator to be designed, i.e., how fast can the observed $\hat{x}$ states track the actual x states. Given the large number of the system states, in order to avoid arbitrary pole-placement for the observer matrix L, a Kalman filter is designed instead using MATLAB. The Kalman function takes in the A and C matrices and two covariant matrices that determine the noise level in the sensor inputs and the disturbance inputs, and gives the observer gain matrix L. The Kalman function will find an observer as long as the A, C system is detectable, i.e., the unobservable part of the A matrix has no positive eigenvalues and is therefore stable.

To test the designed observer, the linearized state space is perturbed with a non-equilibrium initial condition and the performance of the observer is assessed to see how well it tracks the states. Fig. 41 shows the observer's performance for four arbitrary states.

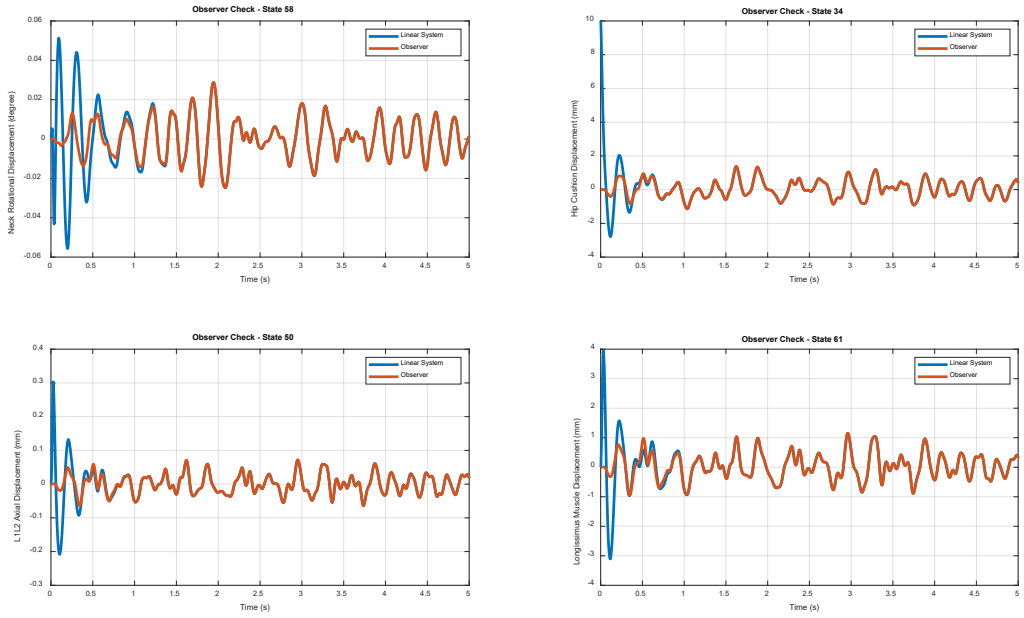

Figure 41. Observer performance check

Fig. 41 shows that the observer converges on all the respective states in about 500 milliseconds at which point the observer's estimation becomes virtually identical to the linear model's predictions. This verifies that the observer can provide a sufficiently accurate estimation of the state space and therefore state-variable feedback is possible for the given control strategy for the passenger model using the seat sensors.

With the estimated states at hand, the state space equations for the linearized system become:

$$\dot{x} = Ax + Bu \quad , \quad y = Cx \quad , \quad u = -K\hat{x}$$

$$\dot{\hat{x}} = A\hat{x} + Bu + L(y - \hat{y}) \quad , \quad \hat{y} = C\hat{x} \quad , \quad u = -K\hat{x}$$

Eq. 89

5.6.Controller performance: random road input

The simulation was run for the case of the vehicle traversing a random road for both control on/off scenarios and the observer-designed controller shows that the ARC is reduced by almost 60% in 5 seconds. Fig.42 compares the ARC for the passive and controlled systems.

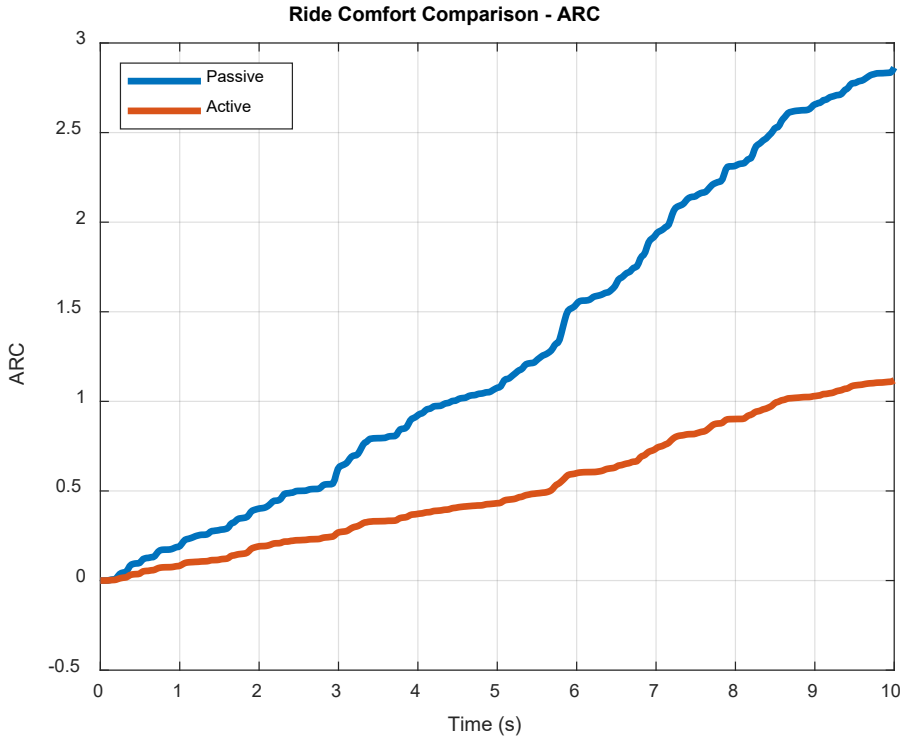

Figure 42. Active vs. Passive performance index, ARC

ARC is the time integral of the sum of weighted, non-dimensional, normalized, displacement energies and therefore increases monotonically. Fig. 42 shows that the proposed controller can reduce the growth of ARC by a factor of almost 3 in 10 seconds. It is also noticed in Fig.42 that the rate of ARC's growth has been reduced for the controlled system.

The weighted, non-dimensional energies are given for the Active vs. Passive systems in Fig.43.

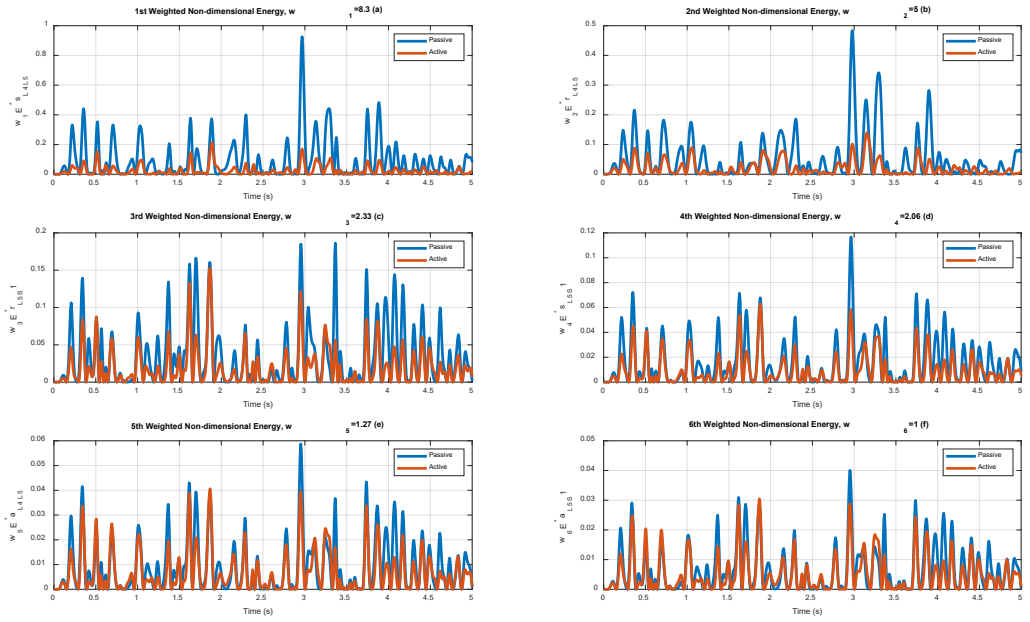

Figure 43. Performance of the controller with respect to the individual six terms that make up ARC

As can be seen in Fig. 43, the active controller has mitigated all six of the displacement energies associated with ARC, particularly the first two energies that had the greatest weightings in Fig.43(a) and Fig.43(b).

Fig.44 gives the sum of the weighted non-dimensional energies for each individual direction.

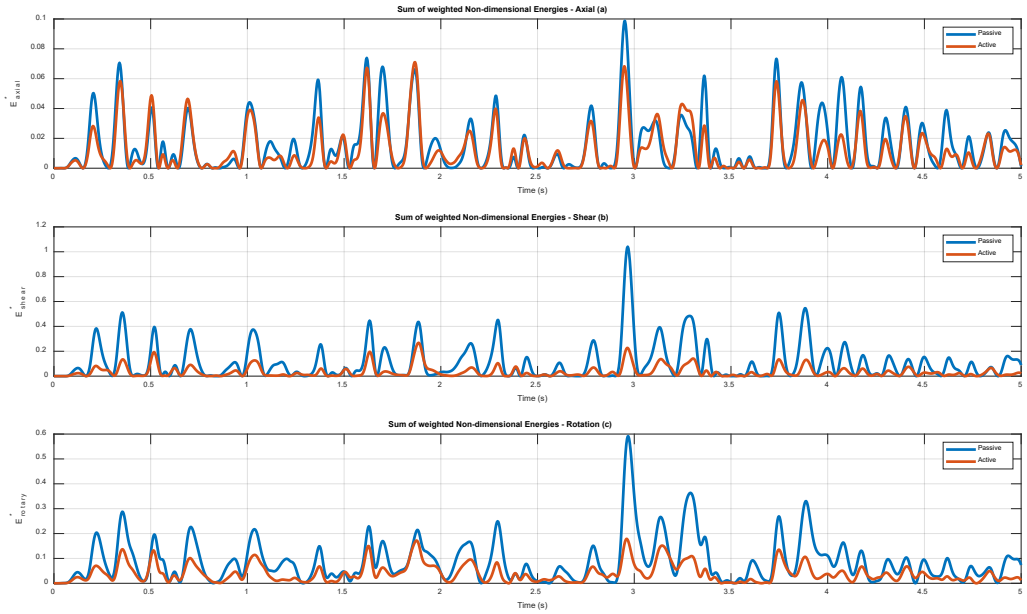

Figure 44. Sum of weighted, non-dimensional energies for the three axial, shear, and rotary directions.

Fig.44(a) shows that while the energy associated with the axial direction has not been significantly reduced, there is a substantial reduction for the shear and rotary directions that have greater weightings in Fig.44(b) and Fig.44(c).

Fig.45 depicts the ARC-associate actual displacement states for both active and passive control.

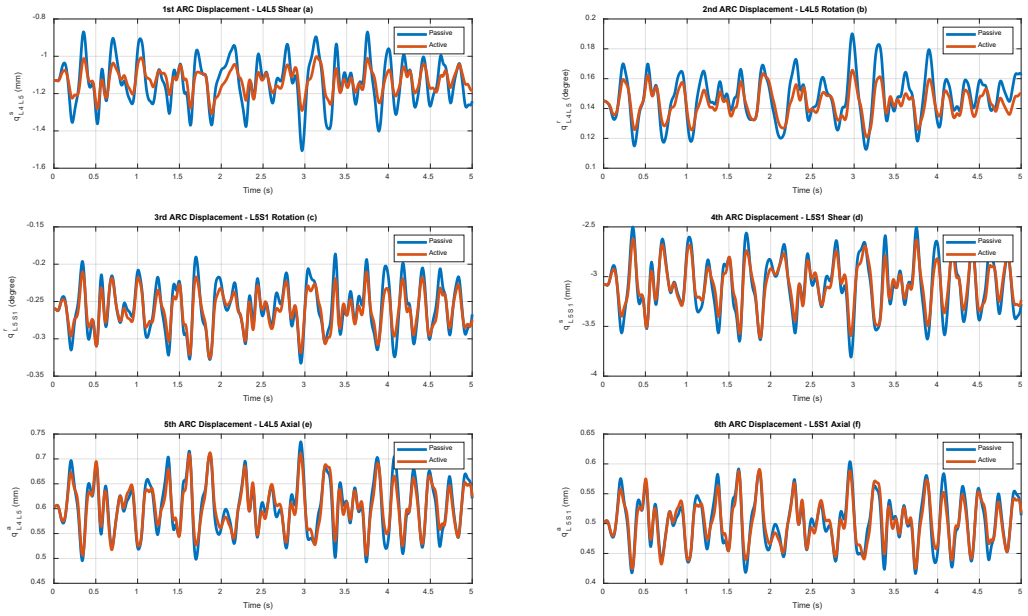

Figure 45. ARC-associated displacement states

As is observed in Fig.45, all ARC-associated displacements have been more or less reduced using active control, particularly the most-weighted displacements in Fig.45(a) and Fig.45(b).

It is further noted that the controller has also reduced the displacements associated with the ARC cost function. However, the other states would also be investigated to ensure the controller is not exacerbating the performance of other states.

The neck joint and the L1L2 joint have been arbitrarily selected as non-ARC displacement candidates. Fig.46 assesses the performance of the controller for non-ARC displacements.

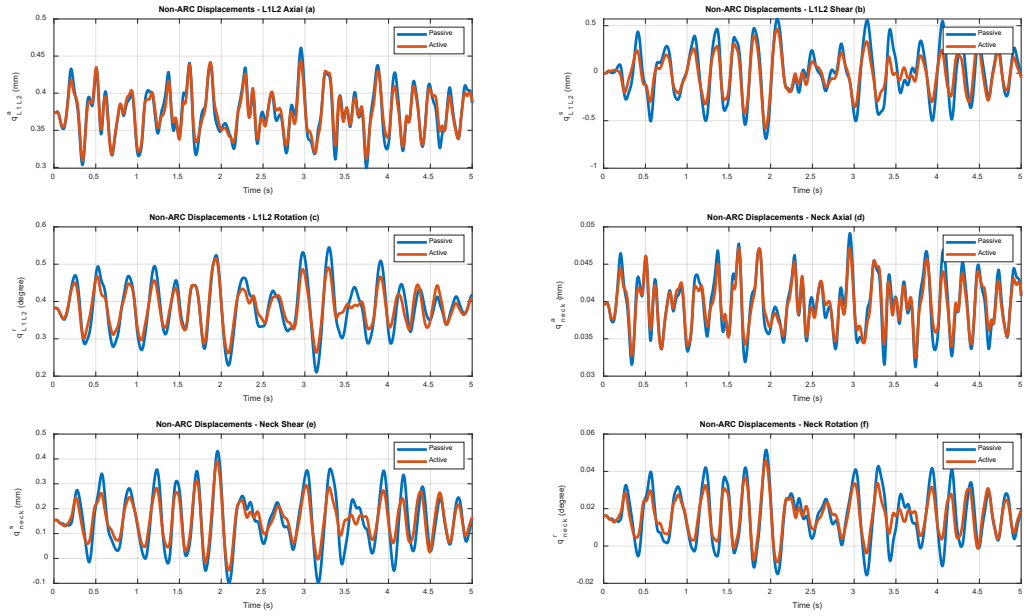

Figure 46. Performance of the controller against non-ARC displacements

It can be seen in Fig.46 that the performance of the controller for those states not included in the ARC cost function is as good or better than the passive response.

5.6.1. Required Power and Force

It was demonstrated that the designed controller can significantly reduce the ARC cost function. The power and force requirements are investigated in Fig.47

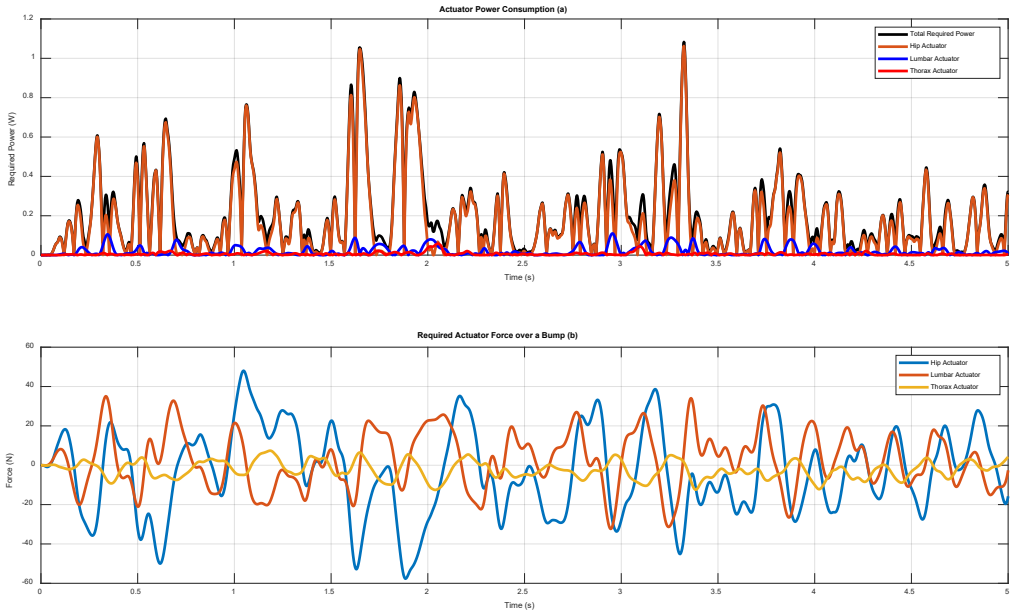

Figure 47. Required power (a) and force (b) for a reduction of ARC by 60%

Fig.47(a) shows that the maximum required total power is almost 1 Watt. The reason the required power is relatively small is that while the required forces are substantial, the relative velocity across which they are applied is quite small. It can also be observed in Fig.48 that the majority of power is required for the hip actuator.

Fig.47(b) shows that forces as large as 60N are required for the controller to perform as demonstrated. The largest force is required at the hip actuator, and the smallest force is required at the thorax actuator.

5.7.Controller performance for a large transient input

In this section the car model is subjected to a large bump input instead of a random road to investigate the performance of the controller for a transient disturbance. A r bump input is

considered such that the vehicle would momentarily lose contact with the ground as it goes over the bump and would be subjected to impulsive accelerations. Fig.48 shows the bump profile.

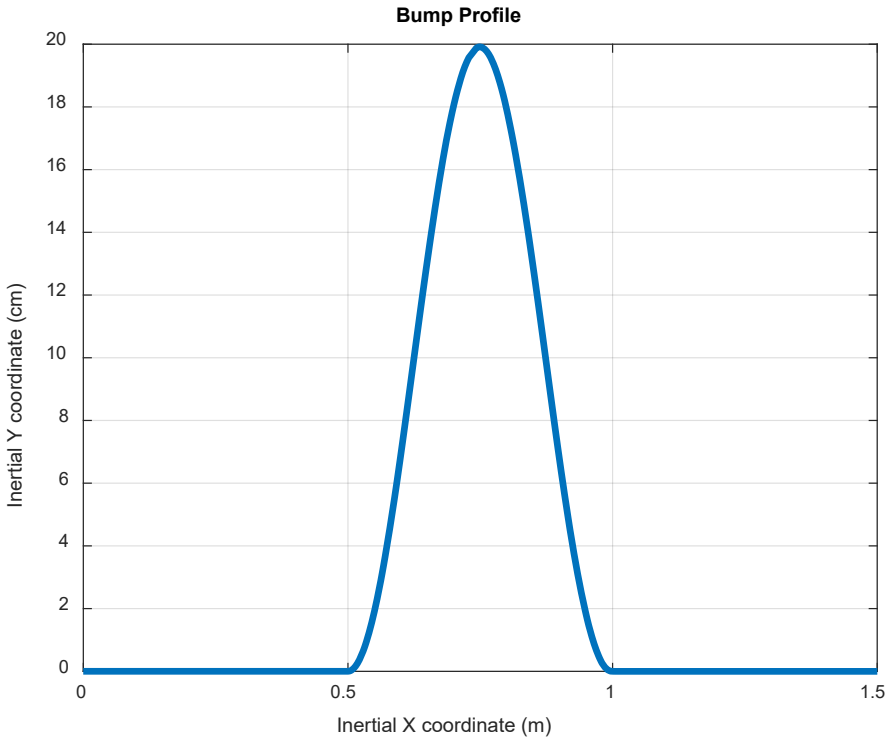

Figure 48. Bump profile

Fig. 49 shows the heave acceleration of the center of gravity and the normal forces on on the tires as the vehicle traverses the bump.

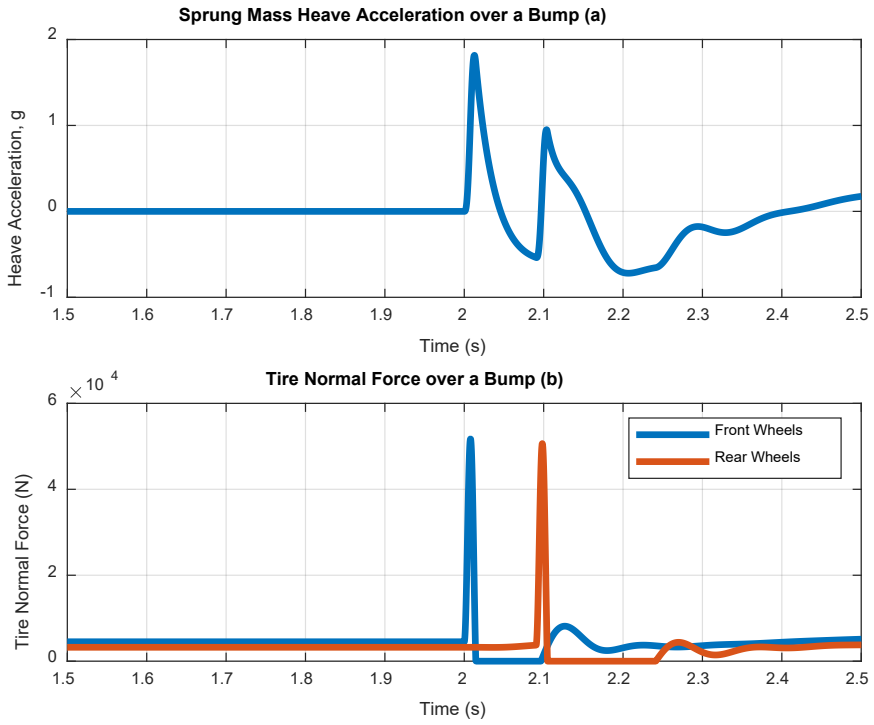

Figure 49. CG acceleration (a) and tire normal force (b) over a bump

It can be seen in Fig.49(a) that as the vehicle goes over the bump, it instantaneously experiences accelerations as large as almost 2 g's and it is also observed in Fig.49(b) that the tires momentarily lose contact with the ground as the normal force has temporarily become equal to zero. This indicates that the given bump can indeed be considered an extreme input.

Fig.50 gives the controller's performance in reducing the ARC cost function over a bump.

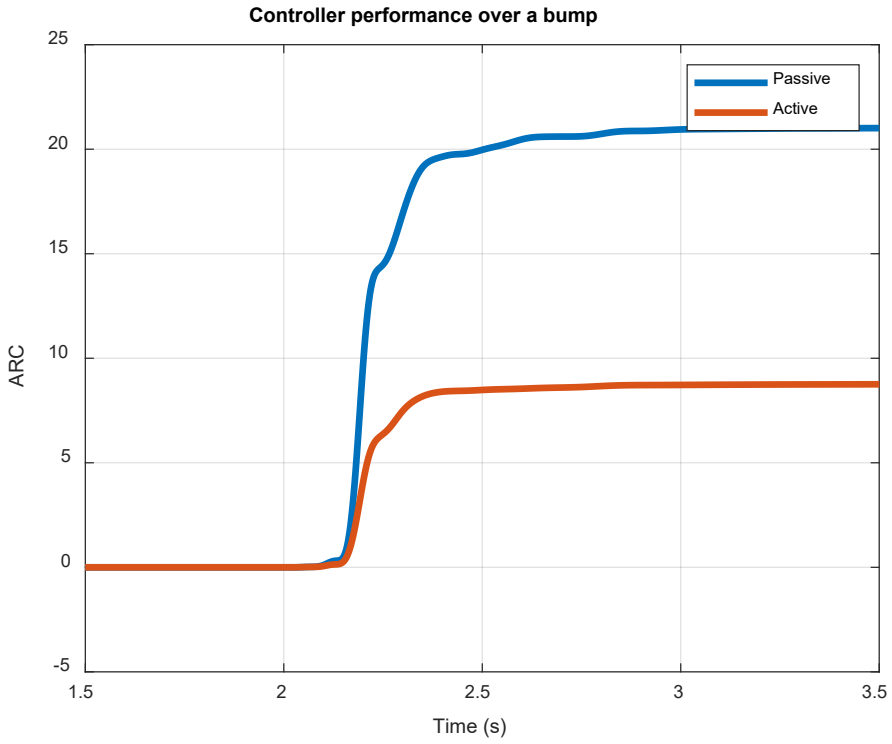

Figure 50. Controller performance over a rough bump: over 50% ARC reduction

Fig.50 shows that the controller has managed to slow down the growth of ARC by more than 50% as the vehicle hits the rough bump.

Fig.51 shows the controller's performance for those ARC-associated displacements as the vehicle traverses the bump.

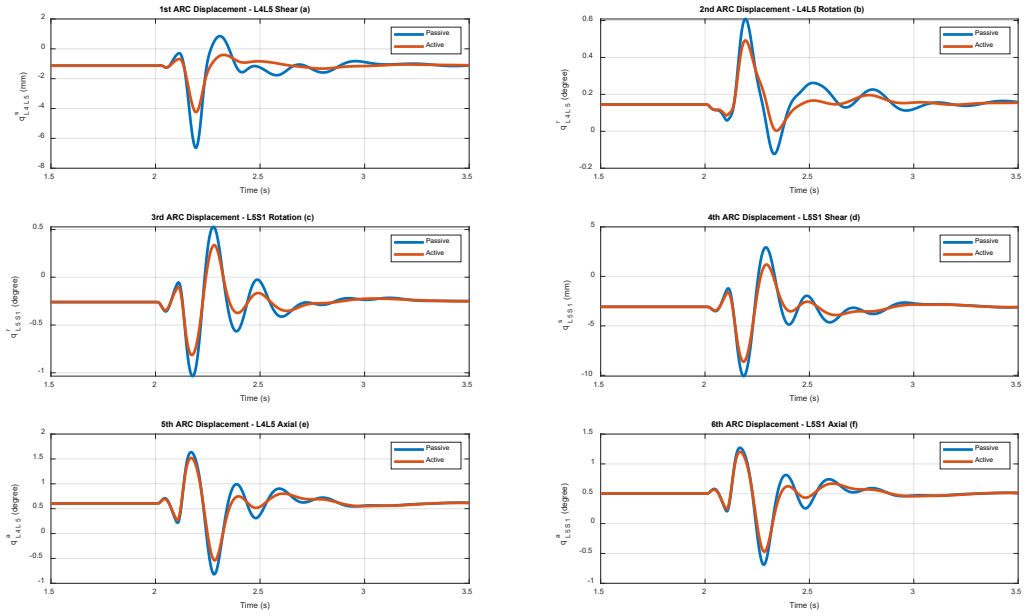

Figure 51. Controller performance against a rough bump input: ARC displacements

Fig.51 shows that the controller somewhat reduces the ARC-displacements compared to the passive system, the reduction is less than when the vehicle traversed a random road.

To check the performance of other states in response to the bump input, again the L1L2 and the neck joints are selected to assess the controller's performance in non-ARC displacements. Fig.52 gives the controller's performance for the non-ARC displacements.

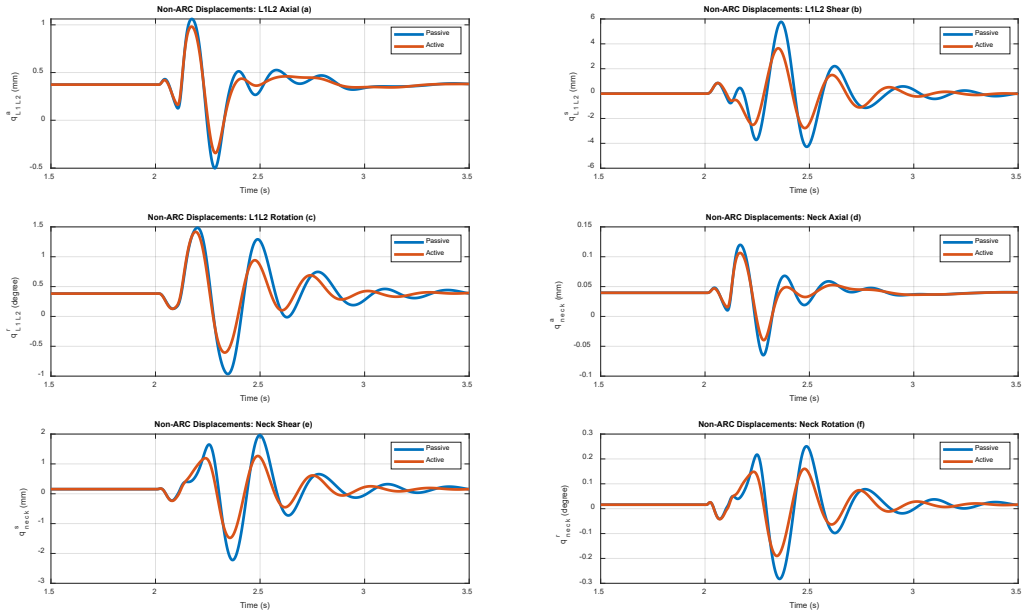

Figure 52. Controller performance against a rough bump input: non-ARC displacements

Fig.52 shows that while the controller has not significantly mitigated the non-ARC displacements, its performance is still better than the passive system in reducing said displacements.

5.7.1. Required power and force

It was gathered that while the controller mitigates the displacement states in response to a bump input, its performance is not as good as when traversing a random road. Fig.53 gives the consumed power and required forces for the controller as the vehicle goes over the bump.

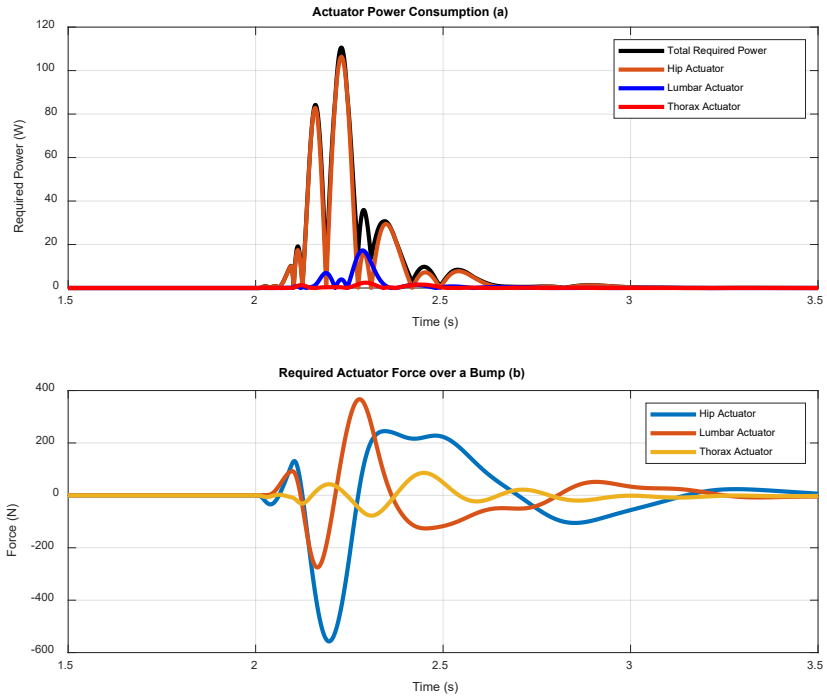

Figure 53. Required actuator power and force: over a bump

Fig.53(a) shows that as much as 100 Watts of power is required for the controller when going over a bump. Again, the majority of the power is consumed at the level of the hip actuator. Fig.53(b) shows that the controller requires as much as 600 N of force. It is noticeable that both the required power and force are significantly larger for a bump input than when traversing a random road.

It is gathered that when the vehicle goes over the rough bump, the controller still manages to reduce the cost function and associated displacements, however, this would require abundant amounts of power and force and the performance would still not be as good as when traversing a random road.

5.8.Required actuator agility

In the previous sections it was assumed that the actuators are all infinitely fast and that they can provide the required force instantly. In this section, a delay will be considered for all actuators and the performance of the delayed system in reducing the cost function is investigated. Fig.54 assesses the actuator performance for various time-delays as the vehicle traverses a random road.

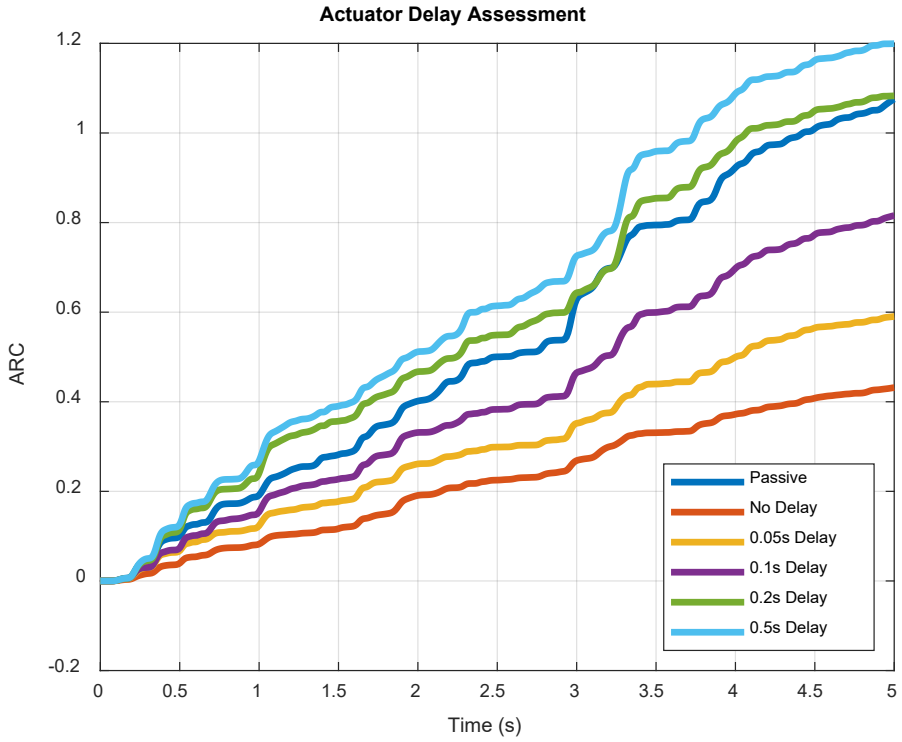

Figure 54. Effect of actuator delay on the ARC cost function

Fig.54 shows that as the actuator delay increases, the controller performance is reduced if the actuators' delay exceeds 0.2 seconds, then the controlled system's performance is worse than the passive system. Therefore, in order for the controller to perform better than the passive system, the actuator's break frequency must be at least 5 Hz. A break frequency of 10Hz allows for 20% reduction of ARC, where a break frequency of 20Hz enables a 40% ARC-reduction.

5.9.Effect of backrest angle

In all previous sections of this study, the backrest inclination angle was considered to be zero, i.e., the seat back is upright. Changing the inclination angle will in fact change the equilibrium position and therefore will change the equilibrium initial conditions of the model and thus change the linearization. A different linearization would result in a different equivalent state space, which will change the controller and observer settings. Hence, the effect of the inclination angle must be considered, and each assessment would need to clarify its assumed backrest inclination angle.

5.10. Implementation

To test and implement the given design, bladder actuators could be employed that can apply compressive pushing forces on demand. For instances that a tensile pulling force is required, it could be achieved through tightening the seat belt which pushes on the body in the other direction and can replicate a pulling effect as if from the seat side.

5.11. Conclusion

The non-linear passenger model was linearized, and an observer-based state variable feedback controller was designed to reduce the ARC cost function which corroborates with better ride comfort. It was gathered that the controller can reduce the ARC by 60% when going over a random road without consuming excessive power or force. If exposed to extreme road inputs such as a rough bump, it was observed that the controller can still reduce the ARC by 50%, despite requiring tremendous power and force. The controller maintains the level of non-target displacement states and reduces the target displacement states. It must be noted that for the controller to have a desirable performance, the actuators need to be sufficiently fast, with a break frequency of at least 5 Hz.

This research helped define a quantitative ride comfort index called ARC that is a measure of the internal displacements of a passenger's body at the lower lumbar level, the region that is susceptible to the highest chronic pains and back-ache injuries.

The present study can have applications in enhancing ride comfort for ground vehicles and improving vehicle seats. It can also have applications whenever an assessment of the internal dynamics of the upper body is required.

6. REFERENCES

[1] C. Wang, X. Zhao, R. Fu, Z. Li, Research on the comfort of vehicle passengers considering the vehicle motion state and passenger physiological characteristics: improving the passenger comfort of autonomous vehicles, International journal of environmental research and public health, 17 (2020) 6821, https://doi.org/10.3390/ijerph17186821

[2] M.G. Da Silva, Measurements of comfort in vehicles, Meas. Sci. Technol., 13 (2002) R41, https://doi.org/10.1088/0957-0233/13/6/201

[3] L.L. Hoberock, A survey of longitudinal acceleration comfort studies in ground transportation vehicles, in, Council for Advanced Transportation Studies, 1976.

[4] D. Oborne, A critical assessment of studies relating whole-body vibration to passenger comfort, Ergonomics, 19 (1976) 751-774, https://doi.org/10.1080/00140137608931589

[5] D. Oborne, Vibration and passenger comfort, Applied Ergonomics, 8 (1977) 97-101,

[6] H. Jacklin, Human reactions to vibration, SAE Transactions, (1936) 401-408,

[7] D. Dieckmann, A study of the influence of vibration on man, Ergonomics, 1 (1958) 347-355, https://doi.org/10.1080/00140135808964610

[8] E. Sperling, C. Betzhold, Contribution to evaluation of comfortable running of railway vehicles, Bulletin of the International Railway Congress Association, 34 (Year) 672-678,

[9] Y. Yang, W. Ren, L. Chen, M. Jiang, Y. Yang, Study on ride comfort of tractor with tandem suspension based on multi-body system dynamics, Appl. Math. Model., 33 (2009) 11-33, https://doi.org/10.1016/j.apm.2007.10.011

[10] H. Reiher, F. Meister, Die Empfindlichkeit des Menschen gegen Stöße, Forschung auf dem Gebiet des Ingenieurwesens A, 3 (1932) 177-180,

[11] L. Fothergill, M. Griffin, The evaluation of discomfort produced by multiple frequency whole-body vibration, Ergonomics, 20 (1977) 263-276, https://doi.org/10.1080/00140137708931626

[12] D. Oborne, M. Clarke, The determination of equal comfort zones for whole-body vibration, Ergonomics, 17 (1974) 769-782, https://doi.org/10.1080/00140137408931423

[13] A. Jones, S. DJ, A scale of human reaction to whole body, vertical, sinusoidal vibration, (1974),

[14] R.C. Sharma, Evaluation of Passenger Ride Comfort of Indian Rail and Road Vehicles with ISO 2631-1 Standards: Part 1-Mathematical Modeling, International Journal of Vehicle Structures & Systems (IJVSS), 8 (2016),

[15] E. Enders, G. Burkhard, F. Fent, M. Lienkamp, D. Schramm, Objectification methods for ride comfort, Forschung im Ingenieurwesen, 83 (2019) 885-898, https://doi.org/10.1007/s10010-019-00361-6

[16] ISO, Shock evaluation of human exposure to whole-body vibration, in: ISO 2631, International Organization for Standardization, 1997.

[17] M. Cieslak, S. Kanarachos, M. Blundell, C. Diels, M. Burnett, A. Baxendale, Accurate ride comfort estimation combining accelerometer measurements, anthropometric data and neural networks, Neural Computing and Applications, 32 (2020) 8747-8762,

[18] M. Fard, L. Lo, A. Subic, R. Jazar, Effects of seat structural dynamics on current ride comfort criteria, Ergonomics, 57 (2014) 1549-1561, https://doi.org/10.1080/00140139.2014.934300

[19] M. Turner, M.J. Griffin, Motion sickness in public road transport: the effect of driver, route and vehicle, Ergonomics, 42 (1999) 1646-1664, 10.1080/001401399184730

[20] S. Chen, D. Wang, A. Zuo, Z. Chen, W. Li, J. Zan, Vehicle ride comfort analysis and optimization using design of experiment, 2010 Second International Conference on Intelligent Human-Machine Systems and Cybernetics, 1 (Year) 14-18, https://doi.org/10.1109/IHMSC.2010.11

[21] A. Soliman, Effect of road roughness on the vehicle ride comfort and rolling resistance, in, SAE Technical Paper, 2006.

[22] A. Soliman, S. Moustafa, A. Shogae, Parameters affecting vehicle ride comfort using half vehicle model, in, SAE Technical Paper, 2008.

[23] C.N. Abernethy III, G. Plank, E.D. Sussman, Effects of deceleration and rate of deceleration on live seated human subjects, in, United States. Urban Mass Transportation Administration, 1977.

[24] C. Abernethy, H. Jacobs, G. Plank, J. Stoklosa, E. Sussman, Maximum deceleration and jerk levels that allow retention of unrestrained, seated transit passengers, Evaluation, 1 (1980),

[25] D. Martin, D. Litwhiler, An investigation of acceleration and jerk profiles of public transportation vehicles, 2008 Annual Conference & Exposition, (Year), https://doi.org/10.18260/1-2--3800

[26] M. Elbanhawi, M. Simic, R. Jazar, In the passenger seat: investigating ride comfort measures in autonomous cars, IEEE Intelligent transportation systems magazine, 7 (2015) 4-17,

[27] K. Kato, S. Kitazaki, T. Sonoda, Effects of driver's head motion and visual information on perception of ride comfort, in, SAE Technical Paper, 2009.

[28] S. Koumura, T. Ohkita, Ride Comfort Evaluation through Analysis of Roll and Lateral Vehicle Behaviors Due to Road Input, SAE International Journal of Passenger Cars-Mechanical Systems, 1 (2008) 472-479,

[29] B.E. Donohew, M.J. Griffin, Motion sickness: effect of the frequency of lateral oscillation, Aviat. Space Environ. Med., 75 (2004) 649-656,

[30] K.C. Parsons, E.M. Whitham, M.J. Griffin, Six axis vehicle vibration and its effects on comfort, Ergonomics, 22 (1979) 211-225, https://doi.org/10.1080/00140137908924605

[31] H. Hayati, D. Eager, A.-M. Pendrill, H. Alberg, Jerk within the context of science and engineering—A systematic review, Vibration, 3 (2020) 371-409, https://doi.org/10.3390/vibration3040025

[32] S.-i. Nakazawa, T. Ishihara, H. Inooka, Real-time algorithms for estimating jerk signals from noisy acceleration data, International Journal of Applied Electromagnetics and Mechanics, 18 (2003) 149-163,

[33] S. Hiroaki, Ability to withstand sudden braking, Railw Res Rev, 52 (1995) 18-21,

[34] J.P. Powell, R. Palacín, Passenger stability within moving railway vehicles: limits on maximum longitudinal acceleration, Urban Rail Transit, 1 (2015) 95-103, https://doi.org/10.1007/s40864-015-0012-y

[35] Q. Huang, H. Wang, Fundamental study of jerk: evaluation of shift quality and ride comfort, in, SAE Technical Paper, 2004.

[36] K. Hayafune, H. Yoshida, Control method of autonomous vehicle considering compatibility of riding comfort and vehicle controllability, SAE Technical Paper, (1990), https://doi.org/10.4271/901486

[37] Y. Liu, L. Zuo, Mixed skyhook and power-driven-damper: A new low-jerk semi-active suspension control based on power flow analysis, Journal of Dynamic Systems, Measurement, and Control, 138 (2016), https://doi.org/10.1115/1.4033073

[38] M. Batra, J. McPhee, N.L. Azad, Anti-jerk dynamic modeling and parameter identification of an electric vehicle based on road tests, Journal of Computational and Nonlinear Dynamics, 13 (2018),

[39] B. Khorram, A. Wåhlberg, A. Tavakoli Kashani, Longitudinal jerk and celeration as measures of safety in bus rapid transit drivers in Tehran, Theor. Issues Ergonomics Sci., 21 (2020) 577-594, https://doi.org/10.1080/1463922X.2020.1719228

[40] A. Scamarcio, M. Metzler, P. Gruber, S. De Pinto, A. Sorniotti, Comparison of anti-jerk controllers for electric vehicles with on-board motors, IEEE Transactions on Vehicular Technology, 69 (2020) 10681-10699,

[41] F. Pradko, R.A. Lee, Vibration comfort criteria, in, SAE Technical Paper, 1966.

[42] VDI, Human exposure to mechanical whole-body vibration, in: VDI2057, Association of German Engineers, 2002.

[43] BSI, Guide to measurement and evaluation of human exposure to whole-body mechanical vibration and repeated shock, in: BS6841, British Standards Institution, 1987.

[44] P. Els, The applicability of ride comfort standards to off-road vehicles, J. Terramech., 42 (2005) 47-64, https://doi.org/10.1016/j.jterra.2004.08.001

[45] J. Marzbanrad, M. Mohammadi, S. Mostaani, Optimization of a passive vehicle suspension system for ride comfort enhancement with different speeds based on design of experiment method (DOE) method, Journal of Mechanical Engineering Research, 5 (2013) 50-59,

[46] V.-q. Le, Ride comfort analysis of vibratory roller via numerical simulation and experiment, DEStech Transactions on Engineering and Technology Research, (2017),

[47] S. Hiemstra-van Mastrigt, L. Groenesteijn, P. Vink, L.F. Kuijt-Evers, Predicting passenger seat comfort and discomfort on the basis of human, context and seat characteristics: a literature review, Ergonomics, 60 (2017) 889-911,

[48] M.V. Shurpali, L. Mullinix, An approach for validation of suspension seat for ride comfort using multi-body dynamics, in, SAE Technical Paper, 2011.

[49] A. Kasaiezadeh, M.R. Jahromi, A. Alasty, Fatigue life assessment approach to ride comfort optimization of a passenger car under random road execution conditions, in, SAE Technical Paper, 2005.

[50] R.-c. Dong, L. He, W. Du, Z.-k. Cao, Z.-l. Huang, Effect of sitting posture and seat on biodynamic responses of internal human body simulated by finite element modeling of body-seat system, J. Sound Vibrat., 438 (2019) 543-554, https://doi.org/10.1016/j.jsv.2018.09.012

[51] M. Gohari, M. Tahmasebi, Active off-road seat suspension system using intelligent active force control, Journal of Low Frequency Noise, Vibration and Active Control, 34 (2015) 475-489, https://doi.org/10.1260%2F0263-0923.34.4.475

[52] A. Kuznetsov, M. Mammadov, I. Sultan, E. Hajilarov, Optimization of a quarter-car suspension model coupled with the driver biomechanical effects, J. Sound Vibrat., 330 (2011) 2937-2946, https://doi.org/10.1016/j.jsv.2010.12.027

[53] Y. Cho, Y.-S. Yoon, Biomechanical model of human on seat with backrest for evaluating ride quality, International Journal of Industrial Ergonomics, 27 (2001) 331-345, https://doi.org/10.1016/S0169-8141(00)00061-5

[54] V. Guruguntla, M. Lal, An improved biomechanical model to optimize biodynamic responses under vibrating medium, Journal of Vibration Engineering & Technologies, 9 (2021) 675-685, https://doi.org/10.1007/s42417-020-00254-x

[55] N. Mohajer, H. Abdi, S. Nahavandi, K. Nelson, Directional and sectional ride comfort estimation using an integrated human biomechanical-seat foam model, J. Sound Vibrat., 403 (2017) 38-58, https://doi.org/10.1016/j.jsv.2017.05.019

[56] T.-H. Kim, Y.-T. Kim, Y.-S. Yoon, Development of a biomechanical model of the human body in a sitting posture with vibration transmissibility in the vertical direction, International Journal of Industrial Ergonomics, 35 (2005) 817-829, https://doi.org/10.1016/j.ergon.2005.01.013

[57] Y. Kozawa, G. Sugimoto, Y. Suzuki, A new ride comfort meter, SAE Transactions, (1986) 1038-1045,

[58] J.A. Ashton-Miller, A.B. Schultz, Biomechanics of the human spine, Basic orthopaedic biomechanics, 2 (1997) 353-385,

[59] RadiologyKey.com, Figure 9.1: Sagittal view of the spine showing vertebral levels, https://radiologykey.com/spine-5/, (2016)

[60] S.M. McGill, Evolving ergonomics?, Ergonomics, 52 (2009) 80-86, https://doi.org/10.1080/00140130802480851

[61] G. McGinty, J.J. Irrgang, D. Pezzullo, Biomechanical considerations for rehabilitation of the knee, Clin. Biomech., 15 (2000) 160-166,

[62] D.A. Neumann, Kinesiology of the musculoskeletal system-e-book: foundations for rehabilitation, Elsevier Health Sciences, 2016.

[63] N.P. Reeves, J. Cholewicki, Modeling the human lumbar spine for assessing spinal loads, stability, and risk of injury, Critical Reviews™ in Biomedical Engineering, 31 (2003),

[64] K.-U. Schmitt, P.F. Niederer, D.S. Cronin, B. Morrison III, M.H. Muser, F. Walz, Trauma biomechanics: an introduction to injury biomechanics, Springer, 2019.

[65] J.N. Katz, Lumbar disc disorders and low-back pain: socioeconomic factors and consequences, JBJS, 88 (2006) 21-24, https://doi.org/10.2106/JBJS.E.01273

[66] T. Keller, Z. Mao, D. Spengler, Young's modulus, bending strength, and tissue physical properties of human compact bone, Journal of orthopaedic research, 8 (1990) 592-603, https://doi.org/10.1002/jor.1100080416

[67] D. Morita, Y. Yukawa, H. Nakashima, K. Ito, G. Yoshida, M. Machino, S. Kanbara, T. Iwase, F. Kato, Range of motion of thoracic spine in sagittal plane, Eur. Spine J., 23 (2014) 673-678, https://doi.org/10.1007/s00586-013-3088-7

[68] D.J. Pearsall, J.G. Reid, L.A. Livingston, Segmental inertial parameters of the human trunk as determined from computed tomography, Ann. Biomed. Eng., 24 (1996) 198-210, https://doi.org/10.1007/BF02667349

[69] S.M. McGill, S. Grenier, N. Kavcic, J. Cholewicki, Coordination of muscle activity to assure stability of the lumbar spine, Journal of electromyography and kinesiology, 13 (2003) 353-359, https://doi.org/10.1016/S1050-6411(03)00043-9

[70] A. M-PRANESH, S. Rakheja, R. Demont, Influence of support conditions on vertical whole-body vibration of the seated human body, Ind. Health, 48 (2010) 682-697, https://doi.org/10.2486/indhealth.MSWBVI-25

[71] G. Marini, G. Huber, K. Püschel, S.J. Ferguson, A 1-D model of the nonlinear dynamics of the human lumbar intervertebral disc, J. Sound Vibrat., 387 (2017) 194-206, https://doi.org/10.1016/j.jsv.2016.09.021

[72] J.C. Iatridis, M. Weidenbaum, L.A. Setton, V.C. Mow, Is the nucleus pulposus a solid or a fluid? Mechanical behaviors of the nucleus pulposus of the human intervertebral disc, Spine, 21 (1996) 1174-1184,

[73] T.H. Smit, M.S. van Tunen, A.J. van der Veen, I. Kingma, J.H. van Dieën, Quantifying intervertebral disc mechanics: a new definition of the neutral zone, BMC musculoskeletal disorders, 12 (2011) 1-10, https://doi.org/10.1186/1471-2474-12-38

[74] A. Shirazi-Adl, Analysis of large compression loads on lumbar spine in flexion and in torsion using a novel wrapping element, J. Biomech., 39 (2006) 267-275, https://doi.org/10.1016/j.jbiomech.2004.11.022

[75] N. Arjmand, Computational biomechanics of the human spine in static lifting tasks, École Polytechnique de Montréal, 2006.

[76] N. An, Human Spine, grabCAD.com, https://grabcad.com/library/human-spine-1, (2014)

[77] D.C. Karnopp, D.L. Margolis, R.C. Rosenberg, System dynamics, Modeling and simulation of mechatronic systems, 4 (1990),

[78] N. Arjmand, A. Shirazi-Adl, B. Bazrgari, Wrapping of trunk thoracic extensor muscles influences muscle forces and spinal loads in lifting tasks, Clin. Biomech., 21 (2006) 668-675, https://doi.org/10.1016/j.clinbiomech.2006.03.006

[79] L. Hansen, M. De Zee, J. Rasmussen, T.B. Andersen, C. Wong, E.B. Simonsen, Anatomy and biomechanics of the back muscles in the lumbar spine with reference to biomechanical modeling, Spine, 31 (2006) 1888-1899, https://doi.org/10.1097/01.brs.0000229232.66090.58

[80] G. Papaioannou, A. Voutsinas, D. Koulocheris, I. Antoniadis, Dynamic performance analysis of vehicle seats with embedded negative stiffness elements, Veh. Syst. Dyn., (2019), https://doi.org/10.1080/00423114.2019.1617424

[81] T.S. Keller, C.J. Colloca, J.-G. Béliveau, Force-deformation response of the lumbar spine: a sagittal plane model of posteroanterior manipulation and mobilization, Clin. Biomech., 17 (2002) 185-196, https://doi.org/10.1016/S0268-0033(02)00003-7

[82] B. Bazrgari, A. Shirazi-Adl, M. Kasra, Computation of trunk muscle forces, spinal loads and stability in whole-body vibration, J. Sound Vibrat., 318 (2008) 1334-1347, https://doi.org/10.1016/j.jsv.2008.04.047

[83] S.R. Ward, A. Tomiya, G.J. Regev, B.E. Thacker, R.C. Benzl, C.W. Kim, R.L. Lieber, Passive mechanical properties of the lumbar multifidus muscle support its role as a stabilizer, J. Biomech., 42 (2009) 1384-1389, https://doi.org/10.1016/j.jbiomech.2008.09.042

[84] K.M. Moorhouse, K.P. Granata, Role of reflex dynamics in spinal stability: intrinsic muscle stiffness alone is insufficient for stability, J. Biomech., 40 (2007) 1058-1065, https://doi.org/10.1016/j.jbiomech.2006.04.018

[85] R. Bayoglu, L. Geeraedts, K.H. Groenen, N. Verdonschot, B. Koopman, J. Homminga, Twente spine model: a complete and coherent dataset for musculo-skeletal modeling of the thoracic and cervical regions of the human spine, J. Biomech., 58 (2017) 52-63, https://doi.org/10.1016/j.jbiomech.2017.04.003

[86] D. Karnopp, Vehicle dynamics, stability, and control, CRC Press, 2013.

[87] M.Y. Svensson, O. Boström, J. Davidsson, H.-A. Hansson, Y. Håland, P. Lövsund, A. Suneson, A. Säljö, Neck injuries in car collisions—a review covering a possible injury mechanism and the development of a new rear-impact dummy, Accid. Anal. Prev., 32 (2000) 167-175, https://doi.org/10.1016/S0001-4575(99)00080-9

[88] P. Russell, M. Pearcy, A. Unsworth, Measurement of the range and coupled movements observed in the lumbar spine, Rheumatology, 32 (1993) 490-497, https://doi.org/10.1093/rheumatology/32.6.490

[89] H. Pacejka, Tire and vehicle dynamics, Elsevier, 2005.

[90] H. Dugoff, P.S. Fancher, L. Segel, An analysis of tire traction properties and their influence on vehicle dynamic performance, SAE transactions, (1970) 1219-1243,

[91] H.B. Pacejka, Modeling of the pneumatic tyre and its impact on vehicle dynamic behaviour, (1995),

[92] D. Karnopp, D.L. Margolis, R.C. Rosenberg, System dynamics, Wiley New York, 1990.

[93] H. Paynter, Generalizing the concepts of power transport and energy ports for system engineering, ASME Presented at the 1958 Annual Meeting New York. NY, (Year),

[94] ISO, Mechanical vibration— Road surface profiles — Reporting of measured data, in: ISO 8608, International Organization for Standardization, 2016.

[95] D.L. Margolis, C.M. Nobles, Semi-active heave and roll control for large off-road vehicles, SAE transactions, (1991) 467-476,

[96] A.N. Rimell, N.J. Mansfield, Design of digital filters for frequency weightings required for risk assessments of workers exposed to vibration, Ind. Health, 45 (2007) 512-519,

[97] M. Mitroi, A. Chiru, Determinations regarding the influence on movement and comfort of different elastic suspension structures in N2 type vehicles, IOP Conference Series: Materials Science and Engineering, 997 (Year) 012049,

[98] B.S. Webster, S.H. Snook, The cost of 1989 workers' compensation low back pain claims, Spine, 19 (1994) 1111-1115; discussion 1116, https://doi.org/10.1097/00007632-199405001-00001

[99] A. Praemer, S. Furner, D.P. Rice, J.L. Kelsey, Musculoskeletal conditions in the United States, (1999),

[100] T. Garcia, B. Ravani, A biomechanical evaluation of whiplash using a multi-body dynamic model, J. Biomech. Eng., 125 (2003) 254-265,

[101] K. Kazuhito, K. Satoshi, S. Takayuki, Effects of Driver's Head Motion and Visual Information on Perception of RideComfort, SAE Technical Paper 2009-01-1223, (2009),

[102] P. Lancaster, L. Rodman, Algebraic riccati equations, Clarendon press, 1995.